Integration of Solid Oxide Electrolyzer and Fischer-Tropsch: A sustainable pathway for synthetic fuel

CrossMark

Giovanni Cinti [a], Arianna Baldinelli [a], Alessandro Di Michele [b], Umberto Desideri [c,*]

[a] Dipartimento di Ingegneria, Università degli Studi di Perugia, Perugia, Italy
[b] Dipartimento di Fisica e Geologia, Università degli Studi di Perugia, Perugia, Italy
[c] Dipartimento di Ingegneria dell'Energia, dei Sistemi, del Territorio e delle Costruzioni, Università degli Studi di Pisa, Pisa, Italy

HIGHLIGHTS

- Electric energy can be efficiently stored into high density Fischer–Tropsch fuels.
- SOFC co-electrolysis is integrated with Fischer-Tropsch synthesis.
- Three different systems are proposed and their performance evaluated.
- Electricity-to-liquid efficiency is as high as 57.2% in the best case.

ARTICLE INFO

ABSTRACT

Because of their easy and widespread distribution and safe handling, liquid fuels are used in everyday life, to power vehicles, aircrafts, ships, etc. The use of fuels from conventional fossil sources is now called for a more sustainable alternative. Hence, chemical energy storage of electricity generated by renewable sources into synthetic fuels represents an interesting solution, solving also other typical problems with renewables, such as grid stabilization.

Within this framework, the present study deals with the production of synthetic green fuels by means of the Fischer-Tropsch process, downstream a previous electricity-to-gas conversion achieved operating a Solid Oxide Electrolyzer (SOE) stack in co-electrolysis. With reference to the state of the art, this study developed the concept of integrating an SOE and a Fischer-Tropsch process in a small plant size, which is compatible with renewables power density. To this aim, fuel upgrading is supposed to be performed separately.

Based on experimental results on a Solid Oxide Cells stack operated in co-electrolysis, three system-level models were developed, evaluating the most performing option. Thus, considering a plant capacity of 1 bbl/day of liquid fuel, in the best scheme, the electricity-to-liquid efficiency was estimated to be 57.2%. Materials introduced into the system are simply water (33,701 ton/MJ) and carbon dioxide (79,795 ton/MJ). While hydrogen is necessary to feed the SOE, net consumption is zero because it is recovered from Fischer-Tropsch product lighter fraction.

© 2015 Published by Elsevier Ltd.

1. Introduction

High efficiency and use of renewable energy sources are among the major keys for a sustainable development. Improving process efficiency requires a great technological effort, either to improve existing solutions or to look for brand-new concepts. The use of renewable energy sources, despite the significant deployment in the last years, still faces typical drawbacks such as the difficulty to predict the generated power exactly and to keep a stable power supply. Thus, in order to obtain the most out of unprogrammable energy sources (such as sun and wind), they have to be coupled with energy storage systems which separate the moments of supply and demand and mitigate electric grid stability issues. In addition to these points, environmental protocols call for a strict emissions control of greenhouse gases and other atmospheric pollutants.

In this paper, a system which stores electricity by means of a high efficiency process, producing a stable, high-density, safe and easy to handle energy vector, is studied. Among all the possible pathways to obtain a useful energy vector, the current work deals with chemical energy storage into a liquid fuel, which is preferable

* Corresponding author. Tel.: +39 0502217375.
E-mail address: umberto.desideri@unipi.it (U. Desideri).

Nomenclature

Abbreviations

RES	renewable energy sources
SOE	solid oxide electrolyzer
FT	Fischer–Tropsch
WGS	water gas shift reaction
RWGS	reverse water gas shift reaction

Symbol

i	current
E_{tn}	thermoneutral voltage, $E_{tn} = \Delta H/zF$
E_{rev}	reversible voltage, $E_{rev} = \Delta G/zF$
j	current density
A	stack active area, $A = i/j$
z	number of electrons needed to electrolyze one mole of reactants
F	Faraday constant, 96485 C/mol_e
Q_{react}	reactants mole flowrate

n	number of carbon atoms
α	chain growth selectivity
W_n	mass fraction of the total of n-carbon atoms compounds
$(\wp)_n$	olefins to paraffins ratio
x_{COout}	CO molar fraction in the Fischer–Tropsch syncrude
x_{COin}	CO molar fraction in the Fischer–Tropsch feeding stream
LHV	lower heating value
η	theoretical electrolysis efficiency
η_{ex}	system exergetic efficiency
η_{FT}	Fischer–Tropsch unit efficiency
η_{GTL}	gas-to-liquid Fischer–Tropsch unit efficiency
η_{SOE}	SOE stack efficiency
η_{tot}	overall power-to-liquid efficiency
$(VI)_{soec}$	SOE stack electrical power requirements
W_{aux}	auxiliary components power requirements
Q_{net}	net thermal energy
S/C	steam to carbon ratio

in many applications that cannot be operated with gaseous fuels. To this end, an efficient electricity storage is achieved by means of high temperature Solid Oxide Electrolyzers [1], which produce syngas out of water and carbon dioxide, operating in co-electrolysis. Carbon dioxide could be recovered from external processes, such as biogas or carbon capture from power plants flue gases. Then, the electricity-to-gas process is followed by a gas-to-liquid conversion, by means of the Fischer–Tropsch process. In this way the final utilization of synthetic carbonaceous fuels results in zero net carbon emissions. The use of solid oxide cells to electrolyze water was recently studied in several works dealing with high temperature steam electrolysis [2–11]; instead, few literature results were found about CO_2 electrolysis [12–16]. The simultaneous electrolysis of CO_2 and H_2O (co-electrolysis), has been studied in the last years in a number of papers presenting experimental measurements [17–22] and system modeling.

Co-electrolysis offers several advantages: in spite of achieving separate steam electrolysis and the subsequent mixing with carbon dioxide in a dedicated reactor [23], a blend of hydrogen and carbon monoxide (referred as syngas) is obtained by simply operating an electrolyzer, without needing any additional component [1].

The produced syngas can be either directly used or further chemically processed (e.g. methanation, DME synthesis, Fischer–Tropsch). The current technical, social and economic scenario is still requiring liquid fuels, favoring the synthesis of middle distillates (paraffinic hydrocarbons, mainly diesel and kerosene) [24]. For this reason, Fischer–Tropsch synthesis represents a key-strategy to produce liquid fuels. From a historical point of view, this process is not new at all, since it was developed in Germany during the Second World War. At that time, the need for aircraft fuels pushed scientists to develop a method to gasify coal (which was locally available) into a valuable blend of liquid hydrocarbons. In such a manner, while oil-derived fuels were not accessible, liquid fuels could still be available. After the war, in some of the world coal richest areas, the Fischer–Tropsch technology allowed to produce liquid fuels: an example that is worth to mention is the Shell large refinery plant in South Africa. Similarly, where methane availability exceeds consumption, the Fischer–Tropsch process was implemented downstream methane reforming.

Although large installations are normally used when employing methane or coal as raw materials, many other technologies exist,

which are suitable to produce a syngas to feed a Fischer–Tropsch process [25]. As an example, biomass gasification is a possible primary step for a further gas-to-liquid process [26,27]. Nevertheless, biomass-derived syngas could contain dangerous impurities and its composition is sensitive to environmental variables and feedstock heterogeneity. This is a clear disadvantage for a durable and correct operation of the catalysts used for the Fischer–Tropsch synthesis. Conversely, the composition of syngas from SOEs is controlled acting on the electrolyzer operational parameters; thus, the quality of the obtained syngas is improved and impurities affecting catalysts lifetime are absent. Moreover, with the aim of increasing the share of solar and wind power, SOEs allow to use the soil more efficiently than producing biomass for energy utilization [28,29].

In several researches, evaluations of SOE-based systems were performed. In [30,31] a model considering the integration of SOEs with a nuclear plant was studied and a 52.6% cycle efficiency was achieved. In [32], a thermodynamic study about the coupling of a SOE and a catalytic reactor for methane and DME synthesis was presented. Similarly, in [33,34] SOE operation in an integrated system for the production of ethanol was simulated. The economic analysis of the system estimated a cost of 1.1 $ per kg of synthesized ethanol. Finally, in [35] a model of an SOE–FT integrated system is presented where the main results are an overall efficiency of 51% and liquid fuels final cost prediction of 4.4–15 $/GGE.

However, there are still several open issues to investigate: one of them is definitely the optimal plant size. While SOE technology can hardly be expected to be scaled-up from the kW range up to the MW in a short time, FT synthesis is often associated with large installations in the order of 10,000 bbl/day, such as Sasol, Shell and PetroSA plants [36–38]. Alongside large-scale applications, many studies concerning smaller-size systems were published in recent years. Sunfire [23] is working on a Fischer–Tropsch system to achieve a minimum liquid fuel production of 600 l/day (4 bbl/day). Rentech [39] has been involved in a demo-installation with the productivity of 10 bbl/day. Finally, Velocys [40] patented a commercial 125 bbl/day modular reactor.

This study was based on the assumptions that the size of Fischer–Tropsch process can be reduced to have cost-effective applications also with smaller plant capacities, getting closer to what foreseen SOE plant sizes are. On one hand, Solid Oxide Electrolyzers can be made of several stack modules, achieving the required system capability. On the other hand, scaling down
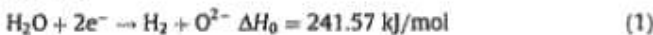
the Fischer-Tropsch process, in order to integrate liquid fuels production into a RES-driven distributed energy generation system, is still a challenge. However, when considering a Fischer-Tropsch process, two sections can be isolated: synthesis and refining. The first consists of transforming the incoming syngas into a syncrude blend made of liquid paraffins, alcohols and waxes, while the second is made of a series of expensive and size-sensitive processes, devoted to syncrude upgrading (e.g.: hydrogenation and isomerization to achieve the proper Octane number). Considering the scenario of several distributed Fischer-Tropsch facilities fed with gas coming from SOEs running on RES power, refining is not taken into account in this study and could still be conceived in a centralized plant receiving the syncrude blends from a number of smaller plants. Therefore, RES energy storage into a liquid medium does not include the upgrading of the primary syncrude to the refined products, which could be performed in a centralized plant, downstream many distributed facilities.

Coherently with such general approach, SOE and Fisher-Tropsch units models were developed; the former is based on experimental data from an SOE stack, while the latter is based on assumptions derived from the literature. Three novel integration designs were developed and studied, considering the overall system efficiency and other advantages, such as complexity reduction and integration with the surrounding environment.

2. Renewables-to-gas: solid oxide electrolysers

In SOEs, electricity is fed to the system to drive electrochemical reactions whose products are valuable gases. Compared to a SOFC, the reactants are fed to the SOE cathode, which is the electrode where reduction takes place, while the anode is the electrode where oxygen is obtained.

In the electrolysis process (Eq. (1)) water is split into hydrogen and oxygen, using heat and work as driving force. When carbon dioxide is also supplied with the reactants, co-electrolysis takes place. As it happens for water, carbon dioxide is reduced and it produces carbon monoxide at the cathode and oxygen at the anode (Eq. (2)).

$$H_2O + 2e^- \rightarrow H_2 + O^{2-} \quad \Delta H_0 = 241.57 \text{ kJ/mol} \tag{1}$$

$$CO_2 + 2e^- \rightarrow CO + O^{2-} \quad \Delta H_0 = 282.79 \text{ kJ/mol} \tag{2}$$

ΔH is the energy necessary for the reactions and it is expressed as the well known sum of two contributions: Gibbs free energy and reaction entropy variation multiplied by the temperature (Eq. (3)). In fuel cells, the Gibbs free energy is the electrical work depending on the reversible potential between the cell electrodes (E_{rev}, Eq. (4)), Faraday constant (F) and electron mole flow associated to each mole of reactant (z; for example: one mole of water requires two moles of electrons as shown in Eq. (1). Thus $z = 2$). Entropy has to be supplied in the form of heat, which makes SOE thermal losses internally valuable because they supply the electrolysis heat demand. When such irreversible thermal losses are equivalent to the heat demand, the energy balance is obtained and, for the aforesaid reasons, the reached energy equilibrium takes the name of thermoneutral. Thus, setting this as design operational point, all electrical input is transformed into hydrogen (or hydrogen plus carbon monoxide), i.e. into chemical potential energy, as defined in (Eq. (4))

$$\Delta H = \Delta G + T\Delta S \tag{3}$$

$$\Delta G = zFE_{rev} \tag{4}$$

$$E_{tn} = \frac{\Delta H}{zF} = E_{rev} + \frac{T\Delta S}{zF} \tag{5}$$

SOE efficiency (Eq. (6)) is calculated as the ratio between the chemical energy exiting the system, in terms of enthalpy (ΔH), and the electrical energy fed from the outside (E_e).

$$\eta = \frac{\Delta H}{E_e} \tag{6}$$

where E_e is the electrical energy input equal to current ($z*F$) multiplied the operating potential E.
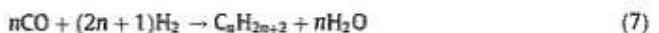
Considering Eq. (4) it can be easily calculated that efficiency is equal to 1 at thermoneutral conditions, where all electrical energy and relative heat losses are converted into chemical energy. In a real system, external thermal contribution may occur and thermoneutral voltage shifts toward higher or lower values if heat is respectively subtracted or supplied to the system.

2.1. Gas-to-liquid: Fischer-Tropsch synthesis

Fischer-Tropsch synthesis is a catalytic gas-to-liquid polymerization process, yielding light refinery gases, a crude blend of hydrocarbons (gasoline and diesel cuts) and waxes. The synthesis process typically takes place at temperatures in the range of 200–240 °C (for low temperature FT applications – LTFT) and 300–350 °C (high temperature FT applications – HTFT) and pressure of about 20–40 bar [41].

State-of-the-art reactors use two types of catalyst: iron and cobalt. The choice of the catalyst is determined by the application. To this end, the latter is more selective toward middle carbon cuts, maximizing diesel production. In addition, other features that support the use of cobalt catalysts are: better performance in terms of CO conversion rates and reduced ageing phenomena. Cost and a poor flexibility to H_2/CO ratio are main drawbacks. However, the second is not an issue whereas syngas composition can be regulated. Thus, an SOE unit assures a constant gas composition with a designed H_2/CO ratio.

From the chemical point of view, Fischer-Tropsch synthesis is a catalytic polymerization consisting of a multi-step mechanism. The first is CO adsorption onto the catalyst surface. Hence, the kinetic of the process is mainly controlled by CO reaction rate [42]. Then, adsorbed CO loses its oxygen atom and it establishes chemical bonds with hydrogen atoms, creating the basic monomer –CH_2–. The reaction mechanism carries on until the chain reaches termination and, then, molecules are desorbed. Typical products are hydrocarbons, alcohols, aldehydes, chetons and so on, featuring a variable-lenght –CH_2– bone. The specific catalyst and the operational conditions (temperature and reactants partial pressure) govern the carbon chain growth, determining the process yield upon each carbon cut. Process chemistry is expressed by the following reactions, concerning paraffins (7), olefins (8) and alcohols (9) production. Varying the integer value attributed to n, Reactions (7)–(9) describe the stoichiometric reactions of all the possible Fischer-Tropsch products, ranging from lower carbon cuts ($n = 1$ methane, $n = 3$ propane) up to upper ones ($n > 30$, paraffinic waxes).

$$nCO + (2n+1)H_2 \rightarrow C_nH_{2n+2} + nH_2O \tag{7}$$

$$nCO + 2nH_2 \rightarrow C_nH_{2n} + nH_2O \tag{8}$$

$$nCO + 2nH_2 \rightarrow C_nH_{2n+1}OH + (n-1)H_2O \tag{9}$$

Typical Fischer-Tropsch catalysts exhibit a variable selectivity upon different carbon cuts. This behavior is described by the chain growth probability factor, called α.

In Fig. 1, a typical products distribution is depicted: the vertical axis reports the mass yield, while the horizontal axis the chain growth probability. Thus, carbon cuts are grouped according to the category listed in Fig. 1 legend.
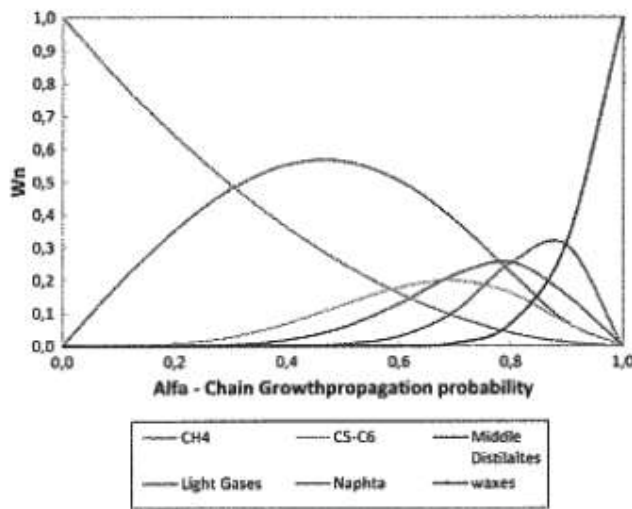
Fig. 1. Fischer–Tropsch products spectrum: mass fraction of several carbon cuts versus catalyst chain growth probability.

From the simple explanation of the mechanism provided previously, it is possible to argue that the closer is α to 1, the more compounds with high carbon number are likely to form. Cobalt catalysts exhibits α values in the range of 0.8–0.94: this is the reason why middle distillates are most favored product of a Co-based Fischer–Tropsch process (Fig. 1).

Besides catalyst performance, even process conditions have an influence on selectivity, and consequently on the yield associated to each carbon cut. When temperature is increased, selectivity shifts products yield to lower carbon number and chain branching is favored. Alcohols synthesis is inhibited. Olefins-to-paraffins ratio, instead, does not change with temperature when dealing with cobalt catalysts. Instead, the effect of increasing pressure is to shift the chain growth probability to higher carbon cuts and to disadvantage branching. Since the process is controlled by CO reaction rate, this determines the conversion efficiency. For SoA catalysts, 80–90% conversion efficiency is expected.

Finally, it is also interesting to point out that Reactions (3)–(5) are globally exothermal. Hence, the perspective to integrate a Fischer–Tropsch process in a system with heat sinks such as SOEs, is very challenging.

3. Experimental activity

To support SOE modeling, a preliminary experimental activity was performed on a Jülich four-cells short stack (Table 1). Cell materials and test bench equipment are deeply discussed in a previous study [43], concerning high temperature steam electrolysis by means of Solid Oxide cells.

SOE stack is kept at constant temperature (750 °C) in an electric furnace. Such temperature was selected because is a trade-off between efficiency (high temperature) and material resistance (lower temperature). 750 °C is considered state of the art for SOFC materials and, consequently, also for SOE. Temperature variation is measured by two thermocouples placed on the interconnection plate inside the stack, the first close to the cathode inlet and the second close to the air inlet. Water is vaporized and mixed with pure gases by a Controlled Evaporation Mixture (CEM) system. Both inlet feed streams are heated up to 650 °C before entering the furnace.

Table 2 reports operating conditions used in the experimental activity. Tests were carried out supplying the anode with a constant air flowrate and varying cathode inlet feedstream composition in terms of $H_2O:CO_2:H_2$ ratios. Hydrogen is introduced to keep a reducing atmosphere and to protect materials from oxidation. Two compositions were considered with different $H_2O:CO_2:H_2$ ratios: namely 30–60–10 and 40–50–10.

$$V(j) = OCV + ASR\,j \qquad (10)$$

4. Process modeling

The paper aims at presenting the concept of electricity-to-liquid conversion accomplished by means of an integrated system consisting of a Solid Oxide Electrolyzer unit and a Fischer–Tropsch reactor. The concept study was developed with a system-level model: in particular, three possible system layouts were studied, evaluating both efficiency and impacts in terms of water consumption and stored carbon dioxide. In addition, SOE unit size is determined, in order to fulfil Fischer–Tropsch syngas requirements for a designed tail-end productivity.

All the calculations have been performed by using the Aspen Plus® environment, based on Nist libraries.

The plant is divided in two main sections: the first one is the electrolyzer unit, the second one is the liquid fuel synthesis unit. While SOE is supposed to operate at environmental pressure, to favor middle distillates selectivity, Fischer–Tropsch reactor is pressurized at 20 bar. Therefore, the two main sections need to be linked by a multistage intercooled compressor. In addition, heat recovery is performed at several levels of the process, so that reduced net heat demand contributes to increase the overall system efficiency.

Because of the down-scaling of the FT liquid fuel synthesis, crude refining is not provided, with the exception of a raw pre-flash separation that divides purge water from hydrocarbons and light refinery gases (hydrogen and carbon products with $n \leqslant 4$). Hence, crude fuel upgrading is to be done in a separate large scale optimized plant, where primary Fischer–Tropsch products can be easily transported.

Table 1
Jülich short-stack features.

Anode substrate	Ni/8YSZ cermet 1500 µm
Anode functional layer	Ni/8YSZ cermet 7–10 µm
Electrolyte	8YSZ 8–10 µm
Cathode functional layer	LSM/8YSZ 10–15 µm
Cathode current collector	LSM 60–70 µm
Stack design	F-design
Interconnect/cell frame	Crofer22APU
Anode contact layer	Ni-mesh
Cathode contact layer	Perovskite type oxide (LCC10)
Sealing	Glass–ceramic (87YSZ20)
Number of cells	4
Size of cells	$100 \times 100\ mm^2$
Active area per cell	$80\ cm^2$

Table 2
SOE experimental campaign: two tests were carried out varying cathode feeding composition.

Electrode feeding composition	Test 30–60–10		Test 40–50–10	
Cathode				
CO_2 (mol/h)	2.56	30%	3.41	40%
H_2O (mol/h)	5.12	60%	4.26	50%
H_2 (mol/h)	0.85	10%	0.85	10%
Anode				
Air (mol/h)	8.92	100%	8.92	100%

In the following, a detailed discussion is presented, describing how system parts were modeled. Afterwards, system performance evaluations of three different designs are shown.

4.1. SOE model

Since Aspen Plus® does not provide a built-in block to simulate the operation of a Solid Oxide Electrolyzer, this component has been modeled merging basic Aspen Plus® blocks and customized Fortran® routines. This unit considers SOE inlet gas temperature at 120 °C. The energy to increase reactants temperature from ambient conditions to 120 °C, included water evaporation, are not taken into account in this paragraph and are discussed in the system integration section. Therefore, the SOE model consists of three main blocks: cathode, electrolyte and anode.

Cathode is the reactants electrode, where inlet gases are supplied and electrolysis takes place. It is modeled by using a first equilibrium reactor, a splitter block, a stoichiometric reactor, a mixer block and a second equilibrium reactor. The first equilibrium reactor adjusts the cathode feedstream composition considering the stack temperature and pressure, according to Reactions (6) and (7). The splitter block divides the reactants stream into two branches, according to the reactants utilization. Reactants utilization (U_{react}, Eq. (11)) represents the conversion rate of reactants involved in the electrochemical process (Eqs. (1) and (2)). It is defined as the ratio between the electric current flowing through the electrolyzer ($j * A$) and the maximum current needed to have all the reactants converted into products ($z * F * Q_{react}$, where z is the number of electrons given by a mole of reactants, F is the Faraday constant and Q_{react} is the total reactant flowrate). U_{react} is assumed to be an input data for the model and it is set at 0.5.

$$U_{react} = \frac{jA}{zFQ_{react}} \quad (11)$$

Then, the stoichiometric reactor is fed with the reactants flow corresponding to the superimposed reactants utilization rate. The stoichiometric reactor accomplishes water (1) and carbon dioxide (2) electrochemical reactions. Oxygen is removed from co-electrolysis products and mixed together with the unreacted stream exiting from the upstream splitter in the following mixer block. Finally, an equilibrium reactor balances the products composition at the cathode outlet. The latter block takes into account the occurrence of RWGS (12) and methanation (13). All the reactions take place at atmospheric pressure and 750 °C.

$$CO_2 + H_2 \rightarrow CO + H_2O \quad (12)$$

$$CO + 3H_2 \rightarrow CH_4 + H_2O \quad (13)$$
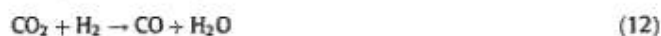
The electrolyte layer is modeled with a simple separator block, which separates oxygen anions (see Eqs. (1) and (2)) from the other cathode products. In such a manner, oxygen is separated from syngas.

The anode is the air electrode. Its function is to extract oxygen from the stack. In the model it is simulated with a gas mixer, whose inlet feedstreams are oxygen from the electrolyte and sweep air. It is common practice to supply air to the anode side because it facilitates oxygen removal and it lowers cells overpotentials due to a high oxygen concentration. Anode-sweep air flowrate is calculated in order to get an oxygen partial pressure of 0.5 bar at the anode exhausts. Lowering oxygen partial pressure would cause an increase in the sweep-air flowrate required and, accordingly, a larger heat demand to keep the anode temperature constant.

Finally, both anode and cathode feed streams temperature is increased to the expected value required at the inlet of the stack (650 °C) by means of heat exchanger blocks. In detail, heat is regeneratively recovered both in the cathode and the anode to increase gas inlet temperature. The amount of heat available is sufficient because oxygen stream from the electrolyte increases the total flow and, consequently, its thermal capacity in comparison with the anode inlet.

Assuming to operate the SOE stack at thermoneutral conditions, cathode feedstream composition was controlled to produce a syngas with the optimal H_2/CO ratio for the downstream Fischer-Tropsch process. As it was explained before, when middle distillates (which end in diesel cuts) are the preferred products, cobalt catalysts exhibit an enhanced selectivity for this particular application, yet requiring very slight variations of reactants H_2/CO ratio. Thus, to achieve an $H_2/CO = 2.1$ ratio at the stack outlet, cathode inlet composition is set according to the ratio $H_2O:CO_2$: H_2 58:34.5:7.5, that is within the range of reactants compositions used in the stack experimental characterization (Table 2). Moreover, hydrogen is fed to the cathode, in order to ensure a reducing atmosphere; as a design specification for the model development, hydrogen concentration in the cathode feed has to be in the range 7–8% [43].

In order to simulate the electric behavior, a Fortran® subroutine was implemented in the model. Thermoneutral conditions (5) are deduced from the overall enthalpy change occurring between the cathode inlet and the cathode outlet. Thus, ΔH (related to the thermoneutral potential according to Eq. (5)) is the sum of three terms: recovered heat necessary to bring cathode reactants up to the stack operational temperature (750 °C), co-electrolysis reactions enthalpy (cathode stoichiometric reactor net duty) and equilibrium reactions enthalpy (equilibrium reactors net duty). Then, stack voltage is set equal to thermoneutral voltage deduced from Eq. (5). Hence, the operational point current density is calculated by means of the polarization curve, presented in the Experimental activity Section (Eq. (10)). By using this routine, the electric power consumed by the SOE stack is determined. Then, system energy balance will lead to the calculation of the right stack size, as it is discussed later.

4.2. Fischer-Tropsch process model

Electrolysis syngas is drawn at the SOE outlet and then sent to an auxiliary section made of an intercooled compressor to achieve the required pressure before entering the Fischer-Tropsch reactor. Fischer-Tropsch synthesis is assumed to take place at 20 bar and reactor is kept isothermal at 230 °C [41].

The Aspen Plus® model of this part of the system is sketched with a splitter block, a stoichiometric reactor, a mixer block and a flash separator.

The splitter block divides the syngas feedstream in two branches: the first enters the stoichiometric block and its flowrate fraction, with respect to the total dry syngas flowrate, is calculated from the expected CO conversion efficiency (ε_{CO}, Eq. (14)) [44]; the second is shortcut to the mixer, where it is combined with Fischer-Tropsch products exiting the stoichiometric reactor. In the model ε_{CO} is set to 0.87 [44]. Splitter block rates were regulated accordingly, with an iterative calculation.

$$\varepsilon_{CO} = 1 - \frac{x_{COout}}{x_{COin}} \quad (14)$$

The stoichiometric reactor accomplishes several reactions (Table 3), providing the conversion of hydrogen and carbon monoxide to a hydrocarbon blend of alkanes and alkenes. Process selectivity toward each path is implemented in the block, using a mathematical model which considers the hydrocarbon chain growth probability over the possible products spectrum. The mathematical model employed is the Anderson–Schulz–Flory

Table 3
Fischer-Tropsch products: for every carbon cut considered, model compounds are selected. Then, polymerization reactions for selected model compounds are shown.

n range	Cut	Model n	Model molecules	Reaction
n = 1	Light gases 1	1	Methane	$CO + 3H_2 \rightarrow CH_4 + H_2O$
$2 \leqslant n \leqslant 4$	Light gases 2	3	Propane	$3CO + 7H_2 \rightarrow C_3H_8 + 3H_2O$
			Propene	$3CO + 6H_2 \rightarrow C_3H_6 + 3H_2O$
$5 \leqslant n \leqslant 6$	C5–C6	6	Exane	$6CO + 13H_2 \rightarrow C_6H_{14} + 6H_2O$
			Exene	$6CO + 12H_2 \rightarrow C_6H_{12} + 6H_2O$
$7 \leqslant n \leqslant 10$	Gasoline	8	Octane	$8CO + 17H_2 \rightarrow C_8H_{18} + 8H_2O$
			Octene	$8CO + 16H_2 \rightarrow C_8H_{16} + 8H_2O$
$11 \leqslant n \leqslant 19$	Middle distillates (Diesel)	16	Cetane	$16CO + 33H_2 \rightarrow C_{16}H_{34} + 16H_2O$
			Cetene	$16CO + 32H_2 \rightarrow C_{16}H_{32} + 16H_2O$
$n \geqslant 20$	Waxes	30	Paraffin wax (C30)	$30CO + 61H_2 \rightarrow C_{30}H_{62} + 30H_2O$

(ASF) distribution [45] described by Eq. (15). For every carbon cut (represented by the parameter n), it relates the products mass fraction (W_n) to the catalyst chain growth probability (α).

$$W_n = n\alpha^{n-1}(1 - \alpha)^2 \tag{15}$$

The ASF function does not take into account any difference among compounds containing the same number of carbon atoms. In other words, for a given n, that is representative of a particular carbon cut, W_n is then the sum of paraffins, oleifins, alcohols and minor species.

However, some distinctions within the same carbon cut can be done considering the catalyst features. In this study we assumed to work with cobalt catalysts; thus, the following approximations are acceptable:

- The synthesis of alcohols, other oxygenated compounds and aromatic hydrocarbons is not favored, so all possible products derived from Eq. (9) can be neglected;
- The relative amount of alkanes and alkenes can be modeled as well. Therefore, the olefins-to-paraffins ratio (O/P) is introduced in Eq. (16). According to this model [46], for every carbon number n, O/P depends only on the catalyst nature, represented by the constant coefficient k. From the model assumptions, k is set to 0.3.

$$\left(\frac{O}{P}\right)_n = e^{-kn} \tag{16}$$

For simplicity, the model considers just a discrete number of possible products, as it is summarized in Table 3: each carbon cut, corresponding to an n range, is represented by one or two model compounds.

Thus, assuming a chain growth probability $\alpha = 0.94$ [41], the ASF distribution in the model is evaluated for every integer n ranging from 1 up to 50. Then, considering Table 3 n ranges, the overall mass fraction yield is evaluated for every discrete n (implementing ASF mathematical model). In order to consider the olefins production per every carbon cut, the O/P ratio was calculated and applied to the discrete ASF distribution results. From those data, the model provides the mass yield for every discrete cut.

Then, the stoichiometric reactor outlet stream and the dry syngas streams that bypassed the reactor are mixed in a mixer block, and gas phase equilibria are adjusted through Gibbs energy variation minimization.

At the end, resulting products ("syncrude") are sent to a flash separator (condenser) that models the first stage of raw products upgrading. Light gases, liquid phase ("crude") and water are separated.

Flash separator temperature is calculated to optimize phase separation and minimize the solubility of hydrocarbons into water.

The model of the Fischer-Tropsch section ends without considering further refining, for the reasons already described.

4.3. Auxiliaries

Between the SOE and FT sections some auxiliary components are necessary, namely a condenser and an intercooled compressor. The condenser is necessary because water needs to be removed from the Fischer-Tropsch feedstream. Since the SOE operates at 50% reactants utilization, syngas still contains much water. Water condensation and removal is necessary for three reasons:

reducing compressor feedstream mass flowrate, compression work substantially decreases, with a benefit on system efficiency;
lowering compressor inlet stream temperature, compression work decreases;
when water content is high, Fischer-Tropsch catalysts degradate, leading to a loss of efficiency.

Water separation is mandatory for the mentioned reasons; in addition to that, water separation from syngas allows water recycling, in order to reduce process net material consumption.

Therefore, water was condensed by means of a flash separator operating at ambient pressure and 35 °C. Condenser temperature is determined according to the steam partial pressure in syngas collected at SOE outlet. Since steam fraction in syngas is expected to be around 30% at the given operational point of the electrolyzer, condenser temperature must be lower than 68 °C. Afterwards, dry syngas is sent to a multistage intercooled compressor that achieves an overall pressure ratio of 20. In the model, this is simulated with two compressor blocks, separated by a heat exchanger. Syngas temperature at the heat exchanger outlet is controlled to fulfil Fischer-Tropsch temperature requirements at the last compressor stage exit. Finally, other auxiliary components are introduced in the system, but their operation will be discussed in the following section because it concerns the specific layout that is implemented (see Fig. 2).

4.4. System configurations

In this study, three plant layouts were considered (Fig. 3). In particular, they are referred as layout A, B and C. For all the layouts considered, system design specifications are Fischer-Tropsch synthesis productivity (set to 1 bbl/day) and SOE cathode outlet stream quality, expressed as H_2/CO ratio (set to 2.1). Then, according to specific system layouts (A, B, C), SOE feeding flowrate and composition are determined accordingly. Hereinafter, a description of each layout is reported.

Layout A is the base case and it consists of an SOE section connected to the FT section through an intercooled compressor (Fig. 3A). Layout A features an open loop strategy and no material recirculation is performed. Consequently, SOE feeding flowrates (water, carbon dioxide and hydrogen) are calculated in order to
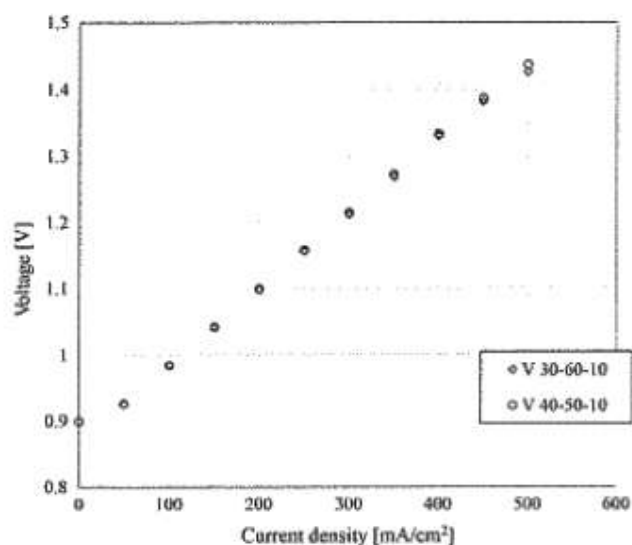
Fig. 2. SOE experimental results: polarization curves (average on four cells) obtained on Table 2 cathode feeding compositions.

provide enough dry syngas for the nominal FT productivity of 1 bbl/day.

Layout B and C have closed loops, performing material recirculation and heat recovery. This strategy aims at improving overall efficiency, while reducing net material consumptions. As far as material recycling is concerned, both waste water and light gases coming out from Fischer-Tropsch synthesis can be re-used within the system itself, with a noticeable effect on the overall plant efficiency. Water is produced as a waste in two sections of the plant: syngas condenser prior intercooled compressor and syncrude condenser downstream the FT synthesis. Water recovered from syngas cooling has a fairly good purity because of the negligible solubility of the other gases. The only exception is carbon dioxide; however, low carbon dioxide traces are acceptable when recirculating recovered water to the SOE inlet. Water removed from the syncrude stream might contain hydrocarbons trace, which is not a problem, since they are supposed to be reformed. Then, light gases fractions extracted from the Fischer-Tropsch syncrude exhibit high hydrogen and carbon dioxide concentrations. This makes those gases recirculation to the SOE inlet very attractive. Light gases contain lower hydrocarbons as well (propane and propene), according to the model proposed above (Table 3).

In layout B (Fig. 3B), syncrude light gases are sent to a reformer and, then, reformate gas enters a shift converter. Reformer and shift converter water requirements are fulfilled with recycled water. Then, the gas stream exiting the shift converter is recirculated to the SOE cathode inlet. Net SOE reactants demand is calculated to reach the nominal flowrate required according to the plant size. Operating separately reforming and shift, temperature control allows reaching maximum conversion efficiency in both reformer and shift converter.

In the model, both reformer and shift converter are simulated with the Aspen Plus® equilibrium reactor. Reformer block operates at 700 °C and 1 bar with a $S/C = 2$, while shift conversion takes place at 310 °C and 1 bar. Shift conversion temperature is much lower because typical reforming temperature will favor the reverse equilibrium, decreasing the final hydrogen concentration. Thus, a heat exchanger to cool the gas is necessary in between the two reactors. Finally, gas coming out of the shift converter is ready to be mixed with reactants makeup stream feeding the cathode fresh

feed stream before the stack inlet. Overall SOE reactants preheating is ensured by the mixing of the makeup stream and shift products. Despite this fact, the system complexity grows because of additional system units. External reforming and shift conversion realize a process that is globally endothermal, increasing the system heat demand. Then, to keep the overall efficiency at a high level, heat recovery requires a supplementary heat exchanger.

Differently from layout B, layout C has no external reforming (Fig. 3C), although some streams are recirculated. In particular, Fischer-Tropsch light gases and recovered water are directly recirculated to the SOE cathode inlet. Since SOE operational temperature is 750 °C and SOE catalysts are nickel-based, methane and low hydrocarbon reforming is likely to happen inside the SOE. Shortcutting unreformed gases directly into the stack simplifies the plant scheme, reducing the components number. Nonetheless, cathode recycled streams are cooled down to water condensation temperature before being sent to the SOE inlet. This increases the heat demand to reach 120 °C at the SOE inlet. Reforming and shift reaction happen at stack temperature, yielding a mixture of hydrogen, carbon dioxide and carbon monoxide. Yet, small amounts of higher hydrocarbons produced in the Fischer-Tropsch reactor could be present in the gas phase coming out of the syncrude condenser. While a large steam concentration in the SOE feedstream favors hydrocarbons reforming, some hydrocarbon fractions could be responsible of carbon deposition on the SOE stack. In such configuration, the necessary energy to support internal reforming is provided by the SOE stack; then, running the stack at its maximum efficiency, thermoneutral voltage is shifted with regard to the other layouts and a change in the power density occurs as well.

In this case, SOE cathode feedstream water fraction must fulfill both reforming and electrolysis demand (always keeping SOE reactants utilization at 50%). System layouts that were just discussed are compared considering both overall and single blocks performance. Regardless of the configuration, the Fischer-Tropsch block efficiency and productivity is the same in any case, because operational and inlet conditions are fixed as design specifications. Therefore, A, B and C configurations show different efficiency at system level. Clearly, besides different stream recirculation strategies, also heat management changes, affecting the overall efficiency.

All design specifications are summarized in Table 4, reporting the model section whom they refer to and the system layout in which they are implemented.

4.5. Parameters definitions

Some definitions are needed to compare the different layouts investigated. All the definitions are based on the lower heating value. In detail, they are: SOE block efficiency in Eq. (17) (it considers as inputs electrical power, thermal power and power associated to hydrogen, while output power is the term related to syngas exiting the stack) and FT block efficiency, related both to syncrude (18) and crude (19) production.

$$\eta_{SOE} = \frac{\sum_{syngas} \dot{m}_j \, LHV_j}{V\,i + Q_{net,SOE} + \sum_{soe} \dot{n}_i \, LHV_i} \tag{17}$$

$$\eta_{FT} = \frac{\sum_{syncrude} \dot{m}_j \, LHV_j}{\sum_{syngas} \dot{n}_i \, LHV_i} \tag{18}$$

$$\eta_{GTL} = \frac{\sum_{crude} \dot{m}_j \, LHV_j}{\sum_{syngas} \dot{n}_i \, LHV_i} \tag{19}$$

While, the overall system performance is described by η_{tot} (Eq. (20)), dividing the crude stream enthalpy flow by system total power consumption (SOE feedings in terms of hydrogen, electricity and heat, compressors' work and total heat sinks requirements).
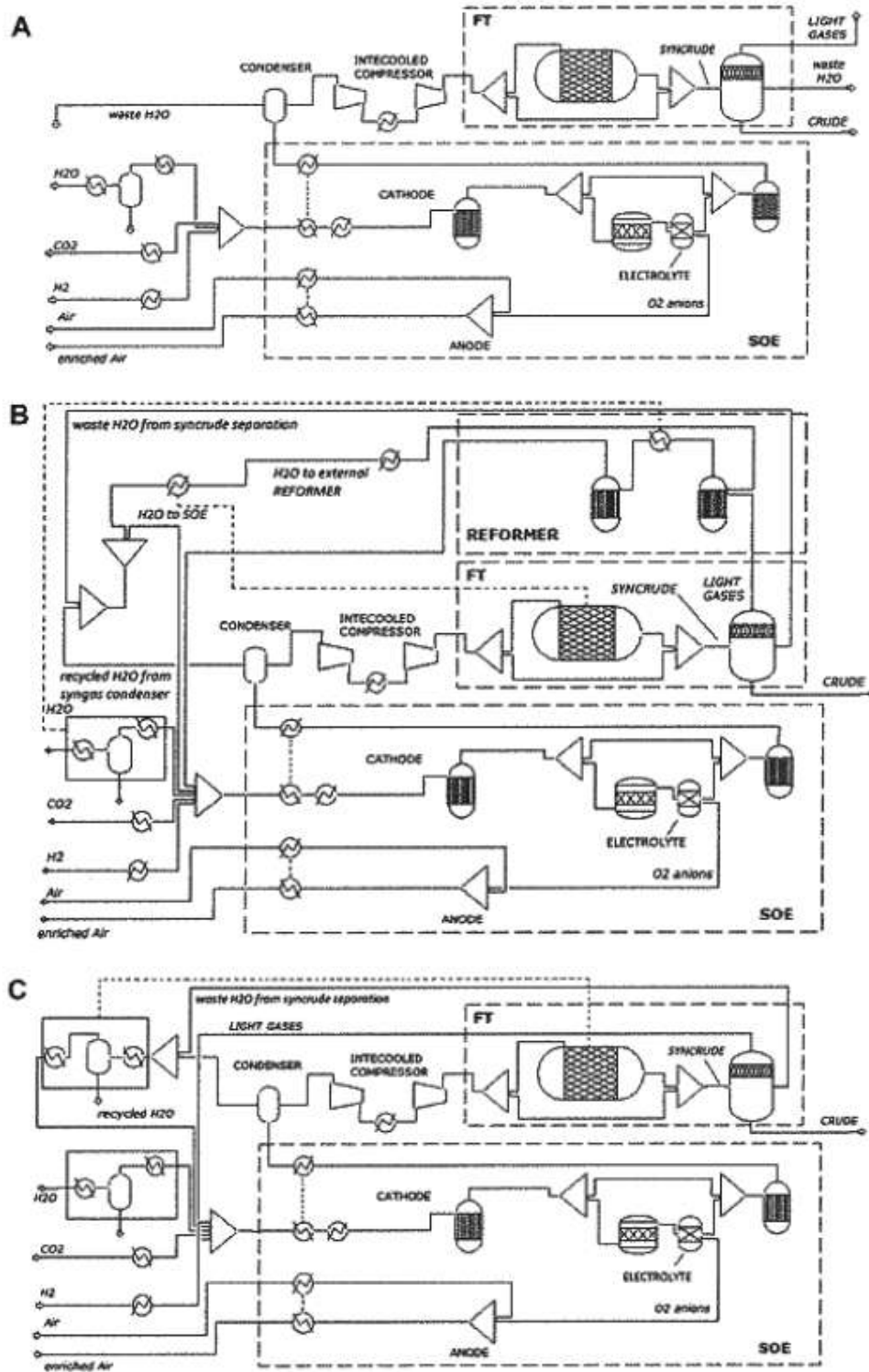
Fig. 3. System layouts: basic integration of SOE with FT (A), recirculation of reformate Fischer-Tropsch lighter gases to SOE inlet (B), recirculation of unreformed Fischer-Tropsch lighter gases to SOE inlet (C).

$$\eta_{tot} = \frac{\sum_{crude} \dot{m}_j \, LHV_j}{\sum_{soec} \dot{n}_i \, LHV_i + (VI)_{soec} + W_{aux} + Q_{net,system}} \qquad (20)$$

$$\frac{p_{el}}{p_{tot}} = \frac{(VI)_{soec}}{\sum_{soe} \dot{n}_i \, LHV_i + (VI)_{soec} + W_{aux} + Q_{net,system}} \qquad (21)$$

Then, with reference to the Second Law of Thermodynamic, other two parameters are introduced: the ratio between electrical input power and total input power (Eq. (21)) and the exergetic efficiency (Eq. (22)).

$$\eta_{ex} = \frac{\sum_{crude} \dot{m}_j \, LHV_j}{\sum_{soe} \dot{n}_i \, LHV_i + (VI)_{soe} + W_{aux} + \sum_k Q_k \left(1 - \frac{T_{ref}}{T_k}\right)} \qquad (22)$$

Table 4
Model design specification summary.

Model section	Design specification	Set point	Layout
SOE	Anode feeding inlet temperature	120 °C	A, B, C
SOE	SOE operational temperature and pressure	750 °C, 1 bar	A, B, C
SOE	SOE operative point	Thermoneutral	A, B, C
SOE	Cathode feeding H_2 + CO concentration	7–8%	A, B, C
SOE	Anode outflow O_2 concentration	50%	A, B, C
SOE	Reactant utilization	50%	A, B, C
SOE	Cathode outflow H_2/CO ratio	2.10	A, B, C
FT	Synthesis temperature and pressure	230 °C, 20 bar	A, B, C
FT	Chain growth probability	0.94	A, B, C
FT	CO conversion efficiency	0.87	A, B, C
FT	Crude synthesis productivity	1 bbl/day	A, B, C
External reformer	Steam-to-carbon ratio	2	B
External reformer	Reforming temperature and pressure	700 °C, 1 bar	B
External shift converter	WGS temperature and pressure	310 °C, 1 bar	B
Heat exchangers	Temperature difference at pinch point	10 °C	B, C

Finally, primary materials (hydrogen, water and carbon dioxide) consumptions are estimated, relating the net consumptions achieved to the system nominal power. Therefore, consumption factors are introduced in Eqs. (23)–(25).

$$H_2O_{consumption}\left[\frac{ton}{MJ}\right] = \frac{net H_2O}{power out} \tag{23}$$

$$H_2{}_{consumption}\left[\frac{ton}{MJ}\right] = \frac{net H_2}{power out} \tag{24}$$

$$CO_2{}_{consumption}\left[\frac{ton}{MJ}\right] = \frac{net CO_2}{power out} \tag{25}$$

4.6. Stack sizing

In the Introduction section, the working principle of an SOE was explained, with particular attention to the thermoneutral voltage that achieves the highest SOE efficiency in any system configuration. Conversely, because of different system configurations implemented in layouts A, B and C, the enthalpy difference that determines the thermoneutral voltage changes. In particular, in layouts A and B enthalpy differences take into account the electrochemical process occurring in the stack, SOE equilibria and sensible heat necessary to rise SOE cathode temperature (covering the thermal gap between 650 °C and 750 °C). Layout C enthalpy difference includes the enthalpy change caused by the reforming of light hydrocarbons recycled to the stack from the syncrude products separation. Owing to the endothermic contribution of reforming, the operational voltage at thermoneutral conditions in layout C is expected to be higher.

Moreover, since the components total flow is controlled by the final liquid fuel productivity, the SOE block has to supply a suitable amount of syngas to the Fischer-Tropsch block.

As a consequence, it is necessary to calculate the stack size for every system layout. To this end, the model developed in this study permits to evaluate SOE unit enthalpy requirements. Then, operational current density (and, consequently SOE unit power density) is determined as the value that produces such overpotentials to match thermoneutral voltage. In other words, operational voltage

(represented by the SOE cells characteristic curve, Eq. (10)) and thermoneutral voltage (Eq. (5)) are equal.

Once current density is calculated and total current is known by assuming a reactant utilization coefficient and syngas Fischer-Tropsch requirements, total SOE active area can be easily found.

5. Results

In this Section, results about the three layouts are presented. It is important to remind the assumption that the design specification that determines components sizing is Fischer-Tropsch liquid fuel productivity (Table 4) which is constant for all the evaluated configurations.

At first, for each block (SOE and FT) feeding streams flowrate and composition are shown, together with product streams flowrate and composition. The SOE performance section reports results concerning the electrolyzer, while the Fischer-Tropsch performance section is relative to the liquid fuel synthesis. Then, efficiency calculations are performed, according to the definitions given at Eqs. (17)–(19) with regard to SOE and FT process respectively.

Finally, system performance and material consumption are calculated according to the previously given definitions. All results concerning the system are reported and discussed in the overall system evaluation section.

5.1. SOE performance

Table 5 reports cathode and anode feed streams and outlet streams of the SOE, calculated according to three layouts (A, B and C). After supplying the makeup streams, cathode feeding flowrates are the same for layouts A and B, while in layout C, in which reforming and shift take place inside the stack at 750 °C, complete CO conversion to H_2 is not achieved and CO is still present among reactant species. Then, to obtain a H_2/CO ratio of 2.1 in the produced syngas, cathode inlet composition was modified with respect to layouts A and B, controlling the makeup flowrates of reactants after light gases recirculation from the syncrude separator block.

When performing reformate gases recirculation (layout B) and Fischer-Tropsch light gases direct recovery (layout C), hydrogen content of recycled stream totally fulfils SOE requirements. In fact,

Table 5
SOE model results. Cathode outflow composition is the same for layout A, B and C. Unit performances calculated in the table are relative to SOE stack operating without recycled feeding and heat recovery (layout A).

	Layouts A and B		Layout C		Layouts A, B, C	
	Cathode feed (mol/h)	Mole frac (%)	Cathode feed (mol/h)	Mole frac (%)	Cathode out (mol/h)	Mole frac (%)
H_2O	1259	58.2	1303	60.2	631	29.2
CO_2	745	34.5	691	32.0	372	17.2
H_2	158	7.3	117	7.8[a]	783	36.2
CO	–	–	51		374	17.3
CH_4	–	–	–	–	1.33	0.1
Total	2162	100	2162	100	2162	100
	Anode feed (mol/h)	Mole frac (%)	Anode feed (mol/h)	Mole frac (%)	Anode out (mol/h)	Mole frac (%)
O_2	180	21	180	21	681	50
N_2	681	79	681	79	1362	50
Total	861	100	861	100	1430	100

[a] 7.8% is the overall molar fraction given by the sum of hydrogen and carbon monoxide.
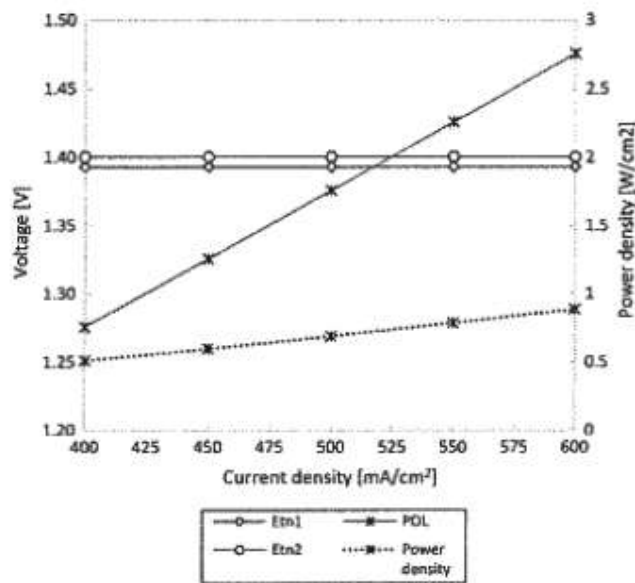
hydrogen concentration achieved in both systems (7.3% and 7.8% respectively) satisfies the design requirements (Table 4).

Concerning anode inlet and outlet streams, flowrate and composition do not change with system layouts.

In all layouts SOE operates at thermoneutral voltage, calculated by the Fortran subroutine based on SOE characteristic V–j Eq. (10). Since negligible differences occur between the two experimental curves used for the linear regression of the V–j equation, it is reasonable to believe that Eq. (10) is suitable for all layouts presented, despite slight variations in the cathode feeding composition.

In Fig. 4, SOE stack polarization characteristic is plotted together with voltages related to the thermoneutral conditions of layouts A–B and layout C. The first voltage, referred as E_{tn1}, is calculated considering layout A–B enthalpy changes inside the stack. Then, the second one, E_{tn2}, is related to layout C enthalpy change. Thermoneutral conditions are calculated considering in the energy balance also the thermal energy necessary to preheat SOE reactants from 650 °C to operational temperature and enthalpy variations of all reactions taking place in the electrolyzer.

Hence, the model subroutine determines the operational point for each layout as the intersection of the polarization curve (POL, Fig. 4) with the thermoneutral voltage. With 50% reactants utilization, in cases A and B, the stack worked at a power density of 0.716 W/cm² (E_{tn1} = 1.39 V). Conversely, in case C the stack working point is shifted to a higher value of power density, 0.735 W/cm² (E_{tn2} = 1.40 V).

5.2. Fischer-Tropsch process performance

After water removal from SOE cathode outflow, dry syngas is fed to the Fischer-Tropsch block: Table 6 shows Fischer-Tropsch inlet stream composition. Taking this input, the FT Aspen Plus® model, based on a discretized ASF distribution, gave the products spectrum shown in Fig. 5.

A few carbon cuts were selected: methane (C1), propane and propene (C3), hexane and hexene (C6), octane and octane (C8), hexadecane and hexadecene (C16), waxes (C30). C6 are low carbon number compounds which have to be further refined. Most of the

Table 6
Fischer-Tropsch input streams and products. Syncrude refers to the whole products stream going out of the Fischer-Tropsch reactor, while Crude relates to Fischer-Tropsch deprived of light gases. Power and efficiency calculations are based on species LHV.

	Feed flow rate (mol/h)	Mole fraction (%)
FT inputs (layouts A, B, C)		
H_2	783	51.2
H_2O	0	0
CO	374	24.4
CO_2	372	24.3
CH_4	1.33	0.1
Total	1532	100
H_2/CO	2.10	

	Components mole flow (mol/h)	Components mole fraction (%)	Power output (kW)	Power allocation (%)
Syncrude				
H_2	69.07	8.16	4.55	6.83
H_2O	345.37	40.78	0.00	0.00
CO	30.29	3.58	5.55	8.33
CO_2	372.12	43.94	0.00	0.00
CH_4	3.39	0.40	0.76	1.14
C_3H_6	2.29	0.27	1.22	1.83
C_3H_8	3.21	0.38	1.83	2.75
C_6H_{12}	0.51	0.06	0.55	0.83
C_6H_{14}	2.69	0.32	2.96	4.44
C_8H_{16}	0.47	0.06	0.57	0.86
C_8H_{18}	4.86	0.57	5.84	8.76
$C_{16}H_{32}$	0.06	0.01	0.17	0.25
$C_{16}H_{34}$	7.98	0.94	20.89	31.36
$WAXC_{30}$	4.48	0.53	21.74	32.63

Energy efficiency		
Power in	(kW)	126.4
Power out	(kW)	66.28
Efficiency	(%)	52.57

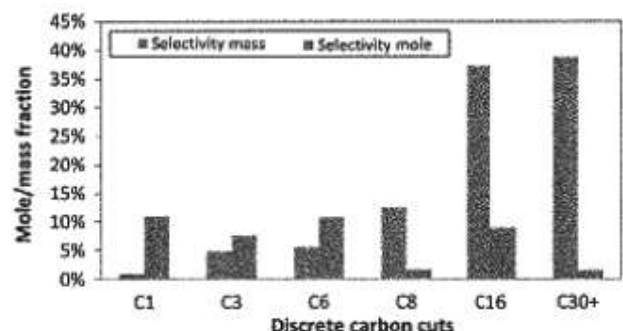|	Crude production (bbl/day)	Power allocation (kW)
Crude		
C_6	0.06	2.67
Gasoline	0.15	6.17
Diesel	0.43	21.06
$WAXC_{30}$	0.36	21.74
Total	1.00	51.63
Gas-to-liquid		
Power in	(kW)	126.4
Power out	(kW)	52
Efficiency	(%)	40.95

Fig. 5. Aspen Fischer-Tropsch model results: products mole and mass fractions. Products spectrum reflects superimposed assumptions about catalyst selectivity.

production is shifted to middle and high carbon numbers (diesel). In this simulation, considering the application of a cobalt catalyst, the occurrence of oxygenates and polycyclic species was neglected.

Table 7

System performance in cases A (basic SOE and Fischer-Tropsch integration), B (SOE and Fischer-Tropsch integration, with external steam reforming and cathode feed recirculation), C (SOE and Fischer-Tropsch integration, with internal steam reforming and cathode feed recirculation).

	Layout A	Layout B	Layout C
Power in (kW)	87.92	77.63	79.70
Auxiliaries Power in (kW)	5.7	5.7	5.7
$Q_{net,system}$ (kW)	17.54	8.90	4.86
Power out (crude) (kW)	51.63	51.63	51.63
E_{th} (V)	1.39	1.39	1.40
A (m^2)	10.43	10.43	10.21
η_{SOE} (%)	79	79	78
η_{GTL} (%)	40.95	40.95	40.95
η_{tot} (%)	46.4	56.0	57.2
W_{in} (kW)	98.07	89.54	86.45
W_{out} (kW)	51.63	51.63	51.63
η_{ex} (%)	52.6	57.7	59.7
$\frac{Rel}{Pot}$ (%)	69.7	88.0	90.1
H_2O consumption (ton/MJ)	121,944	33,707 (−72%)	33,701 (−73%)
H_2 consumption (ton/MJ)	1694	0 (−100%)	0 (−100%)
CO_2 consumption (ton/MJ)	176,397	79,844 (−55%)	79,795 (−51%)

The model was tuned to get a daily liquid fuel production of 1 bbl, corresponding to a chemical storage production capacity of nearly 52 kW.

Then, Table 6 shows efficiency calculations performed according to the definition given above. The total energy efficiency of the system is 52.57% (Eq. (18)), while considering just the crude fraction as valuable product, gas-to-liquid efficiency is 40.95% (Eq. (19)). At system level, power losses occurring when neglecting the gas fraction of the Fischer-Tropsch products are recovered, by performing gas recirculation. Of course, this does not happen for the open loop design studied in layout A.

5.3. Overall system evaluation: layouts comparison

All results concerning the three system layouts presented in this work are displayed in Table 7. Model outcomes are expressed in terms of SOE stack features (thermoneutral voltage, active area, unit efficiency), net power required by the system (SOE power in, auxiliaries power in, net heat demand), power associated to crude production, exergy evaluation, efficiency indexes and material consumption coefficients.

5.3.1. Layout A

Layout A depicts system performance when neither material recirculation, nor heat recovery is performed. Such results were used mainly to assess single components performance. In particular, the FT block performance evaluated in layout A are equal to cases B and C, since FT feeding stream and operational conditions are imposed as design specifications. As a consequence, the auxiliary components (mainly the intercooled compressor) operating between the SOE and the FT process demand the same power consumption in all systems. Thus, considering SOE unit performance, results slightly differ just for cathode feeding composition change (in layout C the water fraction is higher). This has an impact on the net electrical power required to reach thermoneutral conditions and on the thermal energy necessary to pre-heat reactants at SOE inlet temperature. Thus, SOE stack efficiency is lower in layout C than in layouts A and B.

5.3.2. Layout B

The first scenario considers gases recirculation to the SOE cathode inlet. Feeding Fischer-Tropsch light gases to an external reactor, performing separate reforming and shift conversion, hydrogen fraction substantially increases. Overall hydrogen gain is 56.2%, with regard to total hydrogen required at SOE cathode inlet. In detail, after the reforming stage, 27.2% of final hydrogen is recovered, while throughout the following shift conversion, the additional gain is 29%.

On one hand, this solution supplies entirely the system hydrogen demand (hydrogen net consumption is zero), but on the other hand, it entails some drawbacks: increased complexity and increased heat demand. Thus, the integrated system is equipped with two heat exchangers. The first is meant to produce superheated steam for the external reformer, assuming as hot source the Fischer-Tropsch reactor. The latter is operated at 230 °C and, since FT synthesis is exothermal, it needs cooling (waste heat is about 15.6 kW) to keep isothermal conditions. Fig. 6 shows hot and cold curves for the heat recovery steam generator where reformer superheated steam is produced. However, superimposing a pinch-point temperature difference of 10 °C, superheated steam exits the heat exchanger at 220 °C and an additional heat source is necessary to superheat reforming steam from 220 °C up to 700 °C. Considering steam thermal capacity to satisfy a $S/C = 2$, additional heat source power is 3.97 kW. Then, reformer reactor requires 4.93 kW to sustain the process at 700 °C. This thermal power provides also the heat to raise light gases temperature from 25 °C (Fischer-Tropsch products separation tower conditions) to 700 °C. Then, after the reformer stage, shift conversion takes place at 310 °C; therefore, the second heat exchanger cools down reformate gases from 700 °C to 310 °C and waste heat (5.7 kW) is sufficient to vaporize the makeup water stream feeding the SOE
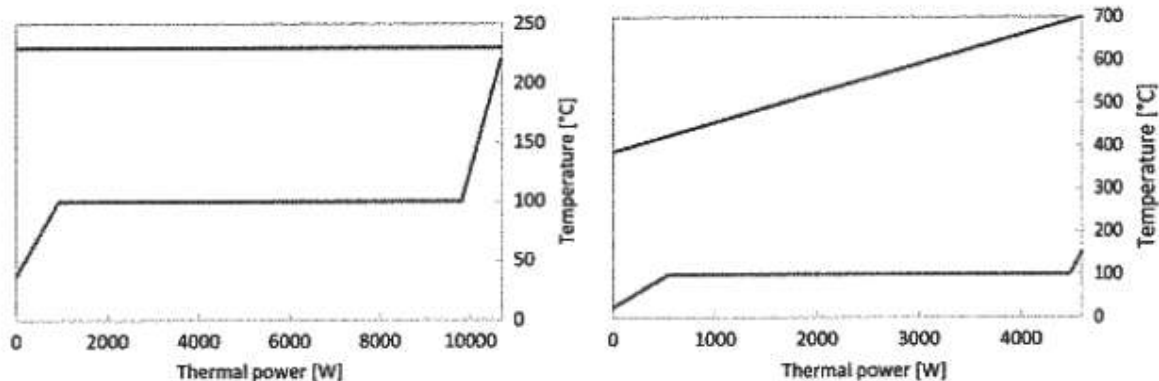

Fig. 6. Layout B heat exchangers diagrams: (left) Fischer-Tropsch reactor cooling thermal balance: heat sink is H_2O recycled to the reformer; (right) cold stream is reintegration water, hot stream is reformed gas.
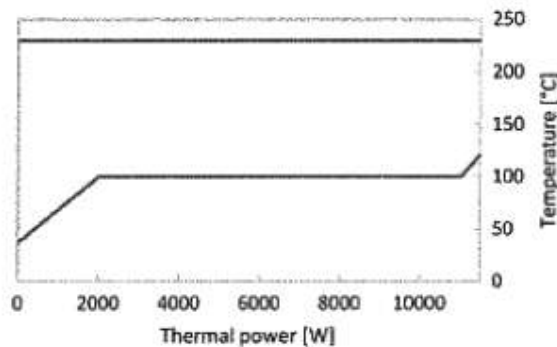
Fig. 7. Layout C heat exchanger diagrams: Fischer-Tropsch heat is used to evaporate water and to achieve superheating.

cathode (Fig. 6). Since the S/C ratio for the reformer is quite high, no more water is supplied to the shift converter.

Streams recirculation covers completely hydrogen requirements, but water and carbon dioxide net consumption are still positive and they call for a makeup stream (with reference to base case layout A, water and carbon dioxide net consumption reductions are respectively 72% and 55%). Besides net consumption reduction, streams recirculation is useful also to increase system energy efficiency. In fact SOE cathode feed stream temperature is already high because recycled streams coming from the shift converter, that is operated at 310 °C, are directly mixed with water and carbon dioxide makeup feed streams.

Based on the definition given at Eq. (20), the overall energy efficiency for layout B is 56%, while according to Eq. (22), exergetic efficiency is 57.5% (Table 7).

5.3.3. Layout C

Performing internal reforming inside the SOE unit, the plant layout turns out to be less complex. Material consumption reduction is: 100% for hydrogen, 51% for carbon dioxide and 73% for water. Thus, cathode water and carbon monoxide makeup stream flowrates were calculated based on the forecast stream composition after achieving SOE internal reforming + shift equilibrium at 750 °C. As a consequence of stack temperature (750 °C), RWGS is expected to be favored and, due to this, carbon monoxide is not totally shifted into hydrogen.

Recovered waste water is heated up to superheated steam, using the Fischer-Tropsch reactor as hot source, which provides 15.6 kW. Heat exchanger hot and cold curves are depicted in Fig. 7. Then, prior SOE inlet superheated steam is mixed to light gases coming from syncrude separation tower and makeup feed streams (water and carbon dioxide). Concerning the latter streams, makeup water needs an additional 4.85 kW heat source, in order to complete phase transition to steam.

The overall energy efficiency of layout C, based on the definition given by Eq. (20), is 57.2%, while, despite the highest p_{el}/p_{tot} ratio, exergetic efficiency, according to Eq. (22), is 59.7% (Table 7). In comparison with previous results, it appears that layout C produces the best performance, together with a system complexity reduction. In addition to that, the change in cathode feeding composition together with a shift of the thermoneutral point leads to a minor extension of the SOE stack size (see active area results, Table 7), with an impact on the system costs. Despite the discussed advantages of layout C, this design introduces the risk of cell materials poisoning due to exposure to light gases; therefore, such issue could limit the applicability of layout C system design.

6. Conclusions

Our work aimed at showing a conceptual design of an electricity-to-liquid fuel system, made of a Solid Oxide Electrolyzer (SOE) stack working in co-electrolysis and a Fischer-Tropsch reactor enhanced for middle-distillates production. In the outlook of distributed generation and energy storage, a basic assumption of this work was the Fischer-Tropsch unit down-scaling, in order to couple the process with a RES-driven electrolyzer. Hence, crude fuel upgrading is to be done in a separate optimized plant, where primary Fischer-Tropsch products can be easily conveyed and post processed.

A system-level model was built for three different system configurations: a basic open loop layout (A), a closed loop layout with reformate gases recirculation (B), a closed loop layout with direct recirculation of Fischer-Tropsch light gases (C). The SOE block was modeled according to experimental data; in the reference to base case (A) where inlet gas composition was $H_2O:CO_2:H_2$ 58:34.5:7.5, at thermoneutral conditions SOE efficiency was estimated to be around 79% (LHV basis). Stack size, in order to supply enough syngas to feed a downstream 1 bbl/day Fischer-Tropsch reactor, was expressed in terms of total active area required; hence the result is 10.43 m^2 with regard to the base case A. Then, taking into account all syncrude components, Fischer-Tropsch energy efficiency was calculated to be 52.7% (LHV basis), while considering only the crude fraction, the efficiency is 40.95%. It is worth to recall that the efficiency of the synthesis is strongly dependent on the hypothesis about the catalyst which enhances CO conversion efficiency and selectivity on different carbon cuts.

The efficiency of the whole system was calculated for the three layouts, which differ from the point of view of waste streams recirculation and internal heat recovery management. Layouts B and C are closed-loop system design, aimed at increasing the performance in comparison with the base open-loop system design (layout A). Among them, the highest first law efficiency is achieved in layout C, where light gas fractions are recirculated directly to the SOE stack. Layout C energy efficiency is slightly higher than the one of layout B (57.2% versus 56%) and design complexity is much lower. However, it should be reminded that degradation phenomena that could occur while supplying unreformed gas to the stack are not considered in this work. As far as material consumption is concerned, layout C achieves the following reductions: −73% water, −51% carbon dioxide and −100% hydrogen. From an exergetic point of view, layout C has a larger electrical consumption than layout B, since its thermoneutral condition is achieved at higher values of power density, namely 0.735 W/cm^2, instead of 0.716 W/cm^2. Layout C was found to have the best second law efficiency too. A follow-up of the study will consider a change in SOE operational temperature that may cause different results due to variation of thermal equilibrium and SOE efficiency.

Finally, keeping the liquid fuel daily productivity unchanged, the SOE stack size required is smaller for case C, with a further consequence on the economic viability of this solution.

References

[1] Graves C, Ebbesen SD, Mogensen M, Lackner KS. Sustainable hydrocarbon fuels by recycling CO_2 and H_2O with renewable or nuclear energy. Renew Sustain Energy Rev 2011;15:1–23. http://dx.doi.org/10.1016/j.rser.2010.07.014.

[2] Ferrero D, Lanzini A, Santarelli M, Leone P. A comparative assessment on hydrogen production from low- and high-temperature electrolysis. Int J Hydrogen Energy 2013;38:3523–36. http://dx.doi.org/10.1016/j.ijhydene.2013.01.065.

[3] Gharibi H, Atikol U, Andrews J, Shabani B. Re-envisioning the role of hydrogen in a sustainable energy economy. Int J Hydrogen Energy 2012;37:1184–203. http://dx.doi.org/10.1016/j.ijhydene.2011.09.137.

[4] Kim S-D, Yu J-H, Seo D-W, Han I-S, Woo S-K. Hydrogen production performance of 3-cell flat-tubular solid oxide electrolysis stack. Int J Hydrogen Energy 2012;37:78–83. http://dx.doi.org/10.1016/j.ijhydene.2011.09.079.

[5] Moçoteguy P, Brisse A. A review and comprehensive analysis of degradation mechanisms of solid oxide electrolysis cells. Int J Hydrogen Energy 2013:1–16. http://dx.doi.org/10.1016/j.ijhydene.2013.09.045.

[6] Nguyen VN, Fang Q, Packbier U, Blum L. Long-term tests of a Jülich planar short stack with reversible solid oxide cells in both fuel cell and electrolysis modes. Int J Hydrogen Energy 2013;38:4281–90. http://dx.doi.org/10.1016/j.ijhydene.2013.01.192.

[7] O'Brien JE, Stoots CM, Herring JS, Lessing PA, Hartvigsen JJ, Elangovan S. Performance measurements of solid-oxide electrolysis cells for hydrogen production. J Fuel Cell Sci Technol 2005;2:156. http://dx.doi.org/10.1115/1.1895946.

[8] Petipas F, Fu Q, Brisse A, Bouallou C. Transient operation of a solid oxide electrolysis cell. Int J Hydrogen Energy 2013;38:2957–64. http://dx.doi.org/10.1016/j.ijhydene.2012.12.086.

[9] Udagawa J, Aguiar P, Brandon NP. Hydrogen production through steam electrolysis: Model-based steady state performance of a cathode-supported intermediate temperature solid oxide electrolysis cell. J Power Sources 2007;166:127–36. http://dx.doi.org/10.1016/j.jpowsour.2006.12.081.

[10] Wang X, Yu B, Zhang W, Chen J, Luo X, Stephan K. Microstructural modification of the anode/electrolyte interface of SOEC for hydrogen production. Int J Hydrogen Energy 2012;37:12833–8. http://dx.doi.org/10.1016/j.ijhydene.2012.05.093.

[11] Zhang H, Lin G, Chen J. Evaluation and calculation on the efficiency of a water electrolysis system for hydrogen production. Int J Hydrogen Energy 2010;35:10851–8. http://dx.doi.org/10.1016/j.ijhydene.2010.07.088.

[12] Ebbesen SD, Mogensen M. Electrolysis of carbon dioxide in solid oxide electrolysis cells. J Power Sources 2009;193:349–58. http://dx.doi.org/10.1016/j.jpowsour.2009.02.093.

[13] Petersen G, Viviani D, Magrini-Bair K, Kelley S, Moens L, Shepherd P, et al. Nongovernmental valorization of carbon dioxide. Sci Total Environ 2005;338:159–82. http://dx.doi.org/10.1016/j.scitotenv.2004.06.025.

[14] Shi Y, Luo Y, Cai N, Qian J, Wang S, Li W, et al. Experimental characterization and modeling of the electrochemical reduction of CO_2 in solid oxide electrolysis cells. Electrochim Acta 2013;88:644–53. http://dx.doi.org/10.1016/j.electacta.2012.10.107.

[15] Stempien JP, Ding OL, Sun Q, Chan SH. Energy and exergy analysis of Solid Oxide Electrolyser Cell (SOEC) working as a CO_2 mitigation device. Int J Hydrogen Energy 2012;37:14518–27. http://dx.doi.org/10.1016/j.ijhydene.2012.07.065.

[16] Zhan Z, Zhao L. Electrochemical reduction of CO_2 in solid oxide electrolysis cells. J Power Sources 2010;195:7250–4. http://dx.doi.org/10.1016/j.jpowsour.2010.05.037.

[17] Bierschenk DM, Wilson JR, Barnett SA. High efficiency electrical energy storage using a methane–oxygen solid oxide cell. Energy Environ Sci 2011;4:944. http://dx.doi.org/10.1039/c0ee00457j.

[18] Ebbesen SD, Graves C, Mogensen M. Production of Synthetic Fuels by Co-Electrolysis of Steam and Carbon Dioxide. Int J Green Energy 2009;6:646–60. http://dx.doi.org/10.1080/15435070903372577.

[19] Ebbesen SD, Høgh J, Nielsen KA, Nielsen JU, Mogensen M. Durable SOC stacks for production of hydrogen and synthesis gas by high temperature electrolysis. Int J Hydrogen Energy 2011;36:7363–73. http://dx.doi.org/10.1016/j.ijhydene.2011.03.130.

[20] Graves C, Ebbesen SD, Mogensen M. Co-electrolysis of CO_2 and H_2O in solid oxide cells: performance and durability. Solid State Ionics 2011;192:398–403. http://dx.doi.org/10.1016/j.ssi.2010.06.014.

[21] Li W, Wang H, Shi Y, Cai N. Performance and methane production characteristics of H_2O–CO_2 co-electrolysis in solid oxide electrolysis cells. Int J Hydrogen Energy 2013;38:11104–9. http://dx.doi.org/10.1016/j.ijhydene.2013.01.008.

[22] Stoots C, O'Brien J, Hartvigsen J. Results of recent high temperature coelectrolysis studies at the Idaho National Laboratory. Int J Hydrogen Energy 2009;34:4208–15. http://dx.doi.org/10.1016/j.ijhydene.2008.08.029.

[23] Sunfire. Sunfire power-to-liquid: n.d. <http://www.sunfire.de/en/produkte/fuel/power-to-liquids>.

[24] Perego C, Bortolo R, Zennaro R. Gas to liquids technologies for natural gas reserves valorization: the Eni experience. Catal Today 2009;142:9–16. http://dx.doi.org/10.1016/j.cattod.2009.01.006.

[25] Wilhelm D, Simbeck D, Karp A, Dickenson R. Syngas production for gas-to-liquids applications: technologies, issues and outlook. Fuel Process Technol 2001;71:139–48. http://dx.doi.org/10.1016/S0378-3820(01)00140-0.

[26] Hamelinck C, Faaij a, Deuuil H, Boerrigter H. Production of FT transportation fuels from biomass; technical options, process analysis and optimisation, and development potential. Energy 2004;29:1743–71. http://dx.doi.org/10.1016/j.energy.2004.01.002.

[27] Hu J, Yu F, Lu Y. Application of Fischer–Tropsch synthesis in biomass to liquid conversion. Catalysts 2012;2:303–26. http://dx.doi.org/10.3390/catal2020303.

[28] Zhu XG, Long SP, Ort DR. What is the maximum efficiency with which photosynthesis can convert solar energy into biomass? Curr Opin Biotechnol 2008;19:153–9. http://dx.doi.org/10.1016/j.copbio.2008.02.004.

[29] Pro BH, Hammerschlag R, Mazza P. Energy and land use impacts of sustainable transportation scenarios. J Clean Prod 2005;13:1309–19. http://dx.doi.org/10.1016/j.jclepro.2005.05.005.

[30] O'Brien JE, McKellar MG, Stoots CM, Herring JS, Hawkes GL. Parametric study of large-scale production of syngas via high-temperature co-electrolysis. Int J Hydrogen Energy 2009;34:4216–26. http://dx.doi.org/10.1016/j.ijhydene.2008.12.021.

[31] O'Brien JE, McKellar MG, Harvego E a, Stoots CM. High-temperature electrolysis for large-scale hydrogen and syngas production from nuclear energy – summary of system simulation and economic analyses. Int J Hydrogen Energy 2010;35:4808–19. http://dx.doi.org/10.1016/j.ijhydene.2009.09.009.

[32] Sun X, Chen M, Jensen SH, Ebbesen SD, Graves C. Thermodynamic analysis of synthetic hydrocarbon fuel production in pressurized solid oxide electrolysis cells. Int J Hydrogen Energy 2012;37:17101–10. http://dx.doi.org/10.1016/j.ijhydene.2012.08.125.

[33] Fouih YEl, Bouallou C. Recycling of carbon dioxide to produce ethanol. Energy Proc 2013;37:6679–86. http://dx.doi.org/10.1016/j.egypro.2013.06.600.

[34] Redissi Y, Bouallou C. Valorization of carbon dioxide by co-electrolysis of CO_2/H_2O at high temperature for syngas production. Energy Proc 2013;37:6667–78. http://dx.doi.org/10.1016/j.egypro.2013.06.599.

[35] Becker WL, Braun RJ, Penev M, Melaina M. Production of Fischer-Tropsch liquid fuels from high temperature solid oxide co-electrolysis units. Energy 2012;47:99–115. http://dx.doi.org/10.1016/j.energy.2012.08.047.

[36] Shell GtL; n.d. <http://www.shell.com/global/future-energy/natural-gas/gtl/story/accessible-version.html>.

[37] PetroSA; n.d. <http://www.petrosa.co.za/>.

[38] Sasol; n.d. <http://www.sasol.com/>.

[39] Rentech; n.d. <http://www.rentechinc.com/>.

[40] Hargreaves N. GTL adds value to gas production. Pet Technol Q. Gas 2012:25–8.

[41] Steynberg AP, Dry ME, editors. Fischer-Tropsch technology Centi G, editors. Studies in surface science and catalysis, vol. 152.

[42] Yates I, Satterfield C. Intrinsic kinetics of the Fischer-Tropsch synthesis on a cobalt catalyst. Energy Fuels 1991;5:168–73. http://dx.doi.org/10.1021/ef00025a029.

[43] Penchini D, Cinti G, Discepoli G, Desideri U. Theoretical study and performance evaluation of hydrogen production by 200 W solid oxide electrolyzer stack. Int J Hydrogen Energy 2014;39:9457–66. http://dx.doi.org/10.1016/j.ijhydene.2014.04.052.

[44] Di Michele A. Sonochemical synthesis of metal nanoclusters and their use in the Fischer-Tropsch process. Thesis, Università degli Studi di Perugia; 2007.

[45] Tavakoli A, Sohrabi M, Kargari A. Application of Anderson-Schulz-Flory (ASF) equation in the product distribution of slurry phase FT synthesis with nanosized iron catalysts. Chem Eng J 2008;136:358–63. http://dx.doi.org/10.1016/j.cej.2007.04.017.

[46] Shi B, Davis BH. Fischer-Tropsch synthesis: the paraffin to olefin ratio as a function of carbon number. Catal Today 2005;106:129–31. http://dx.doi.org/10.1016/j.cattod.2005.07.159.

CrossMark

SOFC fuelled with reformed urea

Giovanni Cinti [a,*], Umberto Desideri [b]

[a] Università degli Studi di Perugia, via Duranti 93, 06125 Perugia, Italy
[b] Università degli Studi di Pisa, Largo Lucio Lazzarino, 56122 Pisa, Italy

HIGHLIGHTS

- We studied the global benefits of utilization of urea as a fuel.
- Urea utilization on solid oxide fuel cell (SOFC) was evaluated.
- We investigated decomposition of urea and a model was developed.
- A SOFC stack was fed with simulated decomposed urea gas stream.
- Data were used to implement a model reaching up to 60% of theoretical efficiency.

ARTICLE INFO

ABSTRACT

Solid Oxide Fuel Cell (SOFC) can be operated with a wide variety of fuels and in a large range of operating conditions. Taking advantage of high temperature and nickel based catalysts several compounds such as methane, ethanol and ammonia can be internally reformed or thermally decomposed producing hydrogen rich gas streams. In this study urea was investigated as a potential fuel for SOFC, since it is a widely available product in the fertilizers' market, safe to be handled and used, and can be recovered from biomass or water treatment plants as a byproduct. An additional pathway for green urea can be based on green hydrogen via electrolysis powered by renewable energy sources and CO_2 recovered from carbon capture plants. Urea decomposition was studied and reproduced in the experimental activity to evaluate its effect on the performance of SOFCs. A gas stream, obtained by simulating decomposed urea with technical gases mixtures, was fed into an SOFC stack, varying the operational temperature and the steam to carbon ratio. Experimental results produced efficiencies higher than 40%. Based on experimental data a 0-D model was developed and operational conditions were expanded, reaching an overall efficiency of 60%.

© 2015 Elsevier Ltd. All rights reserved.

1. Introduction

World energy scenario is nowadays dominated by the research of new sustainable fuels. New fuels and utilization technologies are investigated to reduce emissions in power generation systems and to increase the share of programmable renewable energy, which is becoming more and more important to counterbalance the deployment of solar and wind energy systems. In fact, together with environmental issues, electric grids with high renewable energy penetration are facing the problem of balancing intermittent renewable energy sources with large fossil fired power plants, which need hours to change the power output or to be shut down

or started up. Hence, the request of small, flexible and high efficiency systems for distributed generation. In this scenario Solid Oxide Fuel Cells (SOFC), operating with unconventional or renewable fuels are being investigated as a potential solution to this problem. In this framework, well known and commonly used chemicals, such as urea, can be used as a fuel and can play an important role.

Several studies have demonstrated the capability of high temperature fuel cells to use different gases as fuels, obtaining with most of them power at a higher efficiency than with combustion based power plants.

Among the different fuels that have been studied in high temperature fuel cells, it is worth mentioning ammonia [1–5], biogas [6–14], syngas from biomass gasification [15–18], hydrogen rich mixtures of gases [7], CO rich fuels [19–22]. Even though the performance with those unconventional fuels has always been high,

* Corresponding author.
E-mail addresses: giovanni.cinti@unipg.it (G. Cinti), umberto.desideri@unipi.it (U. Desideri).

most of those fuels had important drawbacks in terms of toxicity, flammability and storage when compared to gasoline, natural gas, diesel oil, LPG.

Starting from the results of previous researches with the above mentioned fuels, the authors of this paper decided to explore the potential of urea as a fuel for a solid oxide fuel cells. Urea combines the positive effects of ammonia and CO, with a substantially reduced danger and toxicity and with a very easy storage characteristic as a solid substance. Urea can be considered as a way to store hydrogen in a compound, even though it is not a carbon free fuel.

To understand the potential of urea as a high temperature fuel cell fuel, an experimental activity was performed together with the development of a numerical simulation of a solid oxide fuel cell using this new fuel. The results are encouraging and very interesting performance is expected even when highly diluted with water. This paper may open a new line of research to assess all critical issues determined by the use of urea as a fuel. To the best knowledge of the authors the use of urea as a high temperature fuel cell fuel has been neither studied nor demonstrated. The only reference found about fuel cell operating with urea is the study of Lan et al. [23], but it is focused on alkaline fuel cells (AFC).
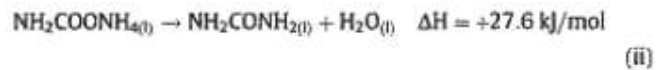
2. Urea as a fuel

Urea has a large worldwide production estimated at 150 million of tons per year [24]. The wide diffusion as a chemical allows to take advantage of a capillary and efficient distribution system and, at the same time, of a mature production technology with high efficiency and competitive costs. Urea is mainly used as a slow release fertilizer but it recently found an important market in selective catalytic reduction (SCR) systems to reduce NOx emissions in fossil fired power plants. Other uses of urea are in zootechnics and petroleum industries. Urea diluted with water at 32.5 wt% was recently commercialized with the trade name of AdBlue, and used in the truck transport sector as a fuel additive to reduce nitrogen oxides to comply with the Euro VI standard.

An alternative source of urea is waste water from urea production plants, estimated up to 1.1–1.6 kg/$t_{ureaproduced}$ [25], or directly from municipal waste waters due to the fact that urea is main component of human and animal urine. An adult man's urine contains 2 wt% of urea. Considering normal urine output a total of 11 kg of urea per person-year can be recovered yielding 18 kg of hydrogen, which is sufficient to power a car for 2700 km [23]. These data show how big the potential of urea, as a fuel, is. In addition, extracting urea from wastewater improves the final emissions. Thus, using urea from wastewaters can be considered part of the waste treatment process with important benefits in terms of energy balance due to the replacement of an energy demanding system, with an energy producing technology. Any pathway including the recovery of urea from wastewaters requires a clean up system to achieve a sufficient purity from contaminants such as sulfur and chlorine, which cause irreversible damage and efficiency decay to SOFCs, as well

as any other energy system. Fig. 1 is a scheme of the urea utilization pathways just described.

As far as the advantages of using urea as a fuel are concerned, it is worth to mention that it is an extremely stable solid crystalline odorless chemical. If it is considered as a fuel, it features a high energy density due to its solid state with the additional characteristics of being neither flammable nor toxic. Considering, in addition, that each cubic decimeter of urea contains 86 g of H_2 whereas the same volume of liquid hydrogen at −252 °C contains 70 g only [23], it is evident that urea is an excellent way of storing and transporting hydrogen. Table 1 reports the main chemical and physical characteristics of urea [26].

Urea was discovered in 1773 by Rouelle and the most widely used synthesis process is the Stamicarbon, that produces urea starting from ammonia and carbon dioxide. The process is based on the following reactions:

$$2NH_{3(g)} + CO_{2(g)} \rightarrow NH_2COONH_{4(l)} \quad \Delta H = -100.5 \text{ kJ/mol} \tag{i}$$

$$NH_2COONH_{4(l)} \rightarrow NH_2CONH_{2(l)} + H_2O_{(l)} \quad \Delta H = +27.6 \text{ kJ/mol} \tag{ii}$$

The above reactions show that CO_2 is required for urea synthesis, which is usually obtained from natural gas reforming, that is used to provide hydrogen for ammonia synthesis. If the process is well balanced CO_2, that is a byproduct of the Haber–Bosch process, is separated and recovered in urea.

There is also a sustainable pathway to produce urea. If electrolysis is used to produce hydrogen from renewable energy, ammonia can be produced without the use of fossil fuels. Renewable energy sources such as sun or wind can supply electricity to the electrolyzer, nitrogen can be directly separated from air, while CO_2 can be recovered from off gases of power plants or from biogas. Urea can thus reach two important goals of recent research in the energy field: storing renewable energy into a solid fuel, contributing to balancing programmable and unprogrammable energy sources and storing CO_2 into a solid fuel, potentially closing the carbon cycle and producing additional power from a single emission of CO_2.

Table 1
Urea main characteristics.

Urea	
H_2 gravimetric density	6.7 wt%
H_2 volumetric density	0.088 kg_{H2}/dm^3
Fusion temperature (solid state)	133 °C
Fusion latent heat	−246.5 kJ/kg
Water solubility (1 atm – 20 °C)	1193 g/dm³
Self injection temperature	Not flammable
Molar weight	60.06 g/mol
Normal density	1320 kg/m³
LHV	18650 kJ/kg

Table 2
Physical and chemical characteristics of AdBlue.

AdBlue	
H_2 gravimetric density	2.2 wt%
H_2 volumetric density	0.024 kg_{H2}/dm^3
Freezing temperature	−11.5 °C (N.B. no negative impact were detected from freezing-defreezing cycle)
Boiling temperature	103 °C
Optimal storage temperature	20 °C (24 months guarantee)
Density	1089.5 kg/m³
Self ignition temperature	Not flammable
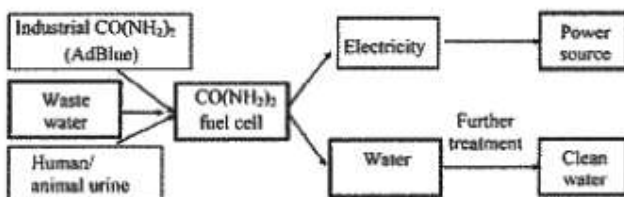
Fig. 1. Urea pathways from source to final use [23].

Table 3
Fuel matrix comparing main energy carrier characteristic.

Fuel	Storage conditions		Molar mass (g/mol)	Density (kg/m³)	LHV (MJ/kg)	Energy density (GJ/m³)	Cost (c€/kg)	Energy Cost (€/MJ)
	T (°C)	P (bar)						
Gaseous hydrogen (H₂) [30]	20	250	2.02	17.86	120.21	2.15	251.90	2.10
Methanol (CH₃OH) [31]	20	1	32.04	790.95	19.7	15.58	33.90	1.72
Natural Gas (CH₄) [32]	20	250	16.04	195.36	50	9.77	96.42	1.93
Gasoline (C₈H₁₈) [33]	20	1	114.23	702.31	43.6	30.62	78.74	1.81
GPL (Propane C3H8) [33]	20	1013.2	44.09	500.56	46.35	23.20	80.91	1.75
Urea (CO(NH₂)₂) [34]	20	1	60.05	1320.00	10.53	13.89	25.33	2.41
AdBlue (32.5 wt% Urea) [35]	20	1	31.67	1087.00	3.42	3.72	38.64	11.30

Theoretical urea decomposition starts at its fusion temperature, 133 °C, via the following reactions [27]:

$$NH_2CONH_{2(l)} \rightarrow NH_{3(g)} + HNCO_{(g)} \qquad \text{(iii)}$$

$$HNCO_{(g)} + H_2O_{(g)} \rightarrow NH_{3(g)} + CO_{2(g)} \qquad \text{(iv)}$$

In reality, urea decomposition is more complex and is further described in the following section.

About the use of urea in fuel cells, the theoretical value of the open circuit voltage (OCV) is 1.146 V, close to hydrogen 1.23 V [23] while the reversible efficiency is 102.9%, i.e. 20% higher than hydrogen's. Note that reversible efficiency of fuel cells can be higher than 100% due to the positive variation of entropy, meaning that, differently from hydrogen and similarly to direct carbon, the cell operates with a heat input directly converted in electricity [23].

Due to wide diffusion of SCR applications AdBlue™ was also studied. AdBlue™ is a registered brand by VDA, the German automotive industry association, and it is a solution of urea in water, with a weight fraction of 32.5%. The brand guarantees high purity urea and deionized water used during production. The use of such liquid was considered in this study as potential vector of urea. Like urea, AdBlue is neither flammable nor toxic nor risky to manipulate. The production takes advantage of the high dilution of urea into water that occurs during urea production process or simply via dissolution of technical urea into deionized water. The main drawback is, of course, a lower energy density because inert water is a useless mass in energetic terms and fuel density indexes are strongly penalized. A crucial advantage is the cost that nowadays is competitive with urea, since a commercial distribution system is already strongly developed. The application in fuel cells benefits of the availability of water for urea reforming even if the steam to carbon ratio is not optimized for such reaction (see following paragraph). Even if AdBlue purity is guarantee from producers included absence of main impurities [28], level of tolerance in fuel cell may be lower of standard SCR and a specific study may be necessary before a commercial utilization of AdBlue as a fuel cell fuel. Table 2 reports the main chemical and physical characteristics of AdBlue.

Differently from hydrogen, urea is not a carbon free fuel and, when reacting, each mole of urea produces one mole of carbon dioxide. In addition, considering the specific application on SOFCs, the presence of carbon required a specific analysis to avoid carbon deposition. The most interesting solution is to add steam to reduce the risk of carbon deposition, enhancing, at the same time, steam reforming of urea. Considering that steam is usually obtained from water, a solution of urea and water represents a suitable input to the system.

To evaluate the potential of urea as a fuel, this compound was compared to more widely used fuels and other potential candidate for energy storage in chemical. Table 3 reports the results of such analysis. Chemical data were taken from National Institute of Standards and Technology [29] while market costs are referred to December 2014. AdBlue was also considered in the study.
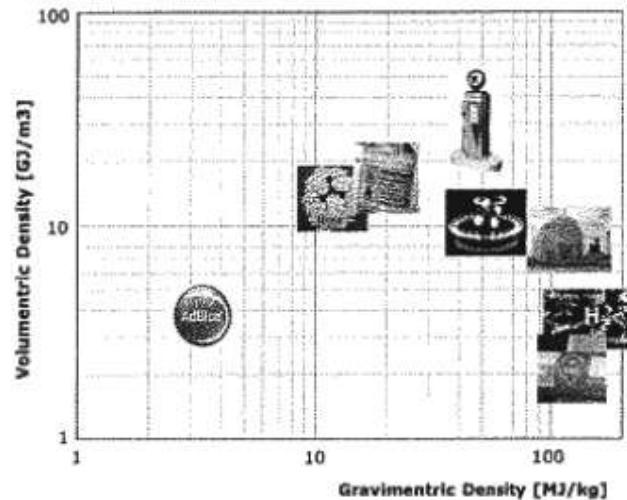

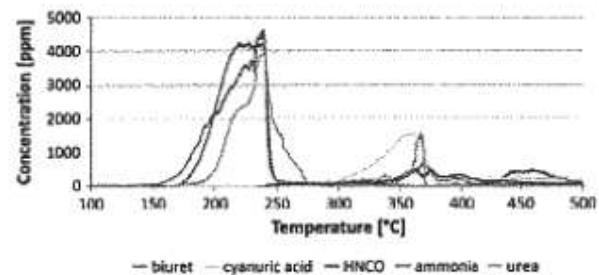Fig. 2. Visual graph comparing energy densities of different fuels.

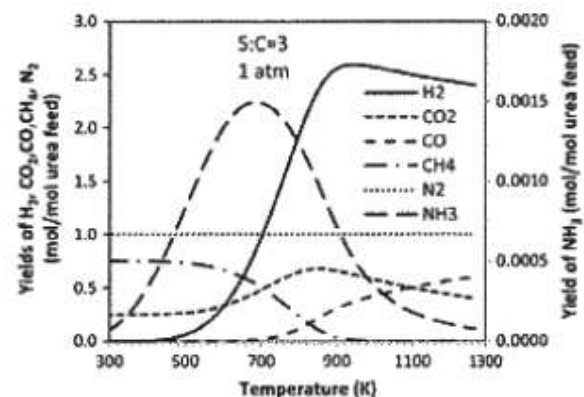Fig. 3. Urea decomposition related to temperature variation.

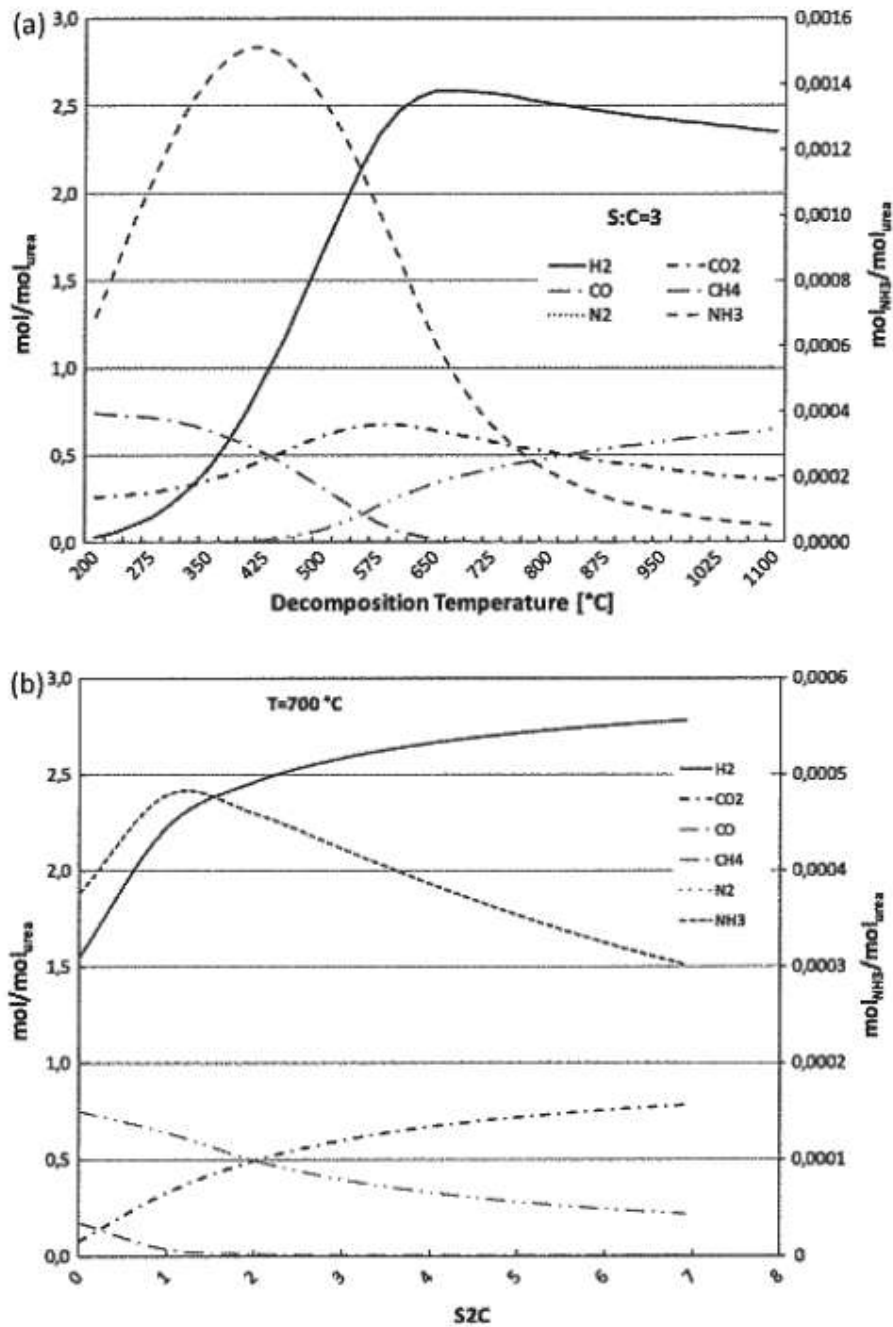Fig. 4. Steam reforming of urea at high temperature [39].

Fig. 5. Simulation results of urea steam reforming at constant S:C (a) and constant temperature (b).

To better visualize the potential of urea as energy vector, gravimetric and volumetric energy densities of all studied compounds were plotted in Fig. 2. As expected urea can easily compete with hydrogen due to its much higher volumetric density, while AdBlue is strongly penalized by the large amount of water contained in the solution.

From the economic point of view, the last column of Table 3 shows how urea and AdBlue are convenient in terms of cost per mass while such advantage is reduced when considering energy cost, due to the high energy of hydrocarbons and the effect of dilution with water in AdBlue. However, the comparison of energy costs is not an absolute indicator because a complete cost evaluation has to consider the efficiency of the technology transforming fuel into electricity.

Summing all characteristic listed here above, the main advantages of using urea as a fuel are:

• High energy density, both gravimetric and volumetric.
• Solid state (easy to be transported).
• Well known synthesis process.
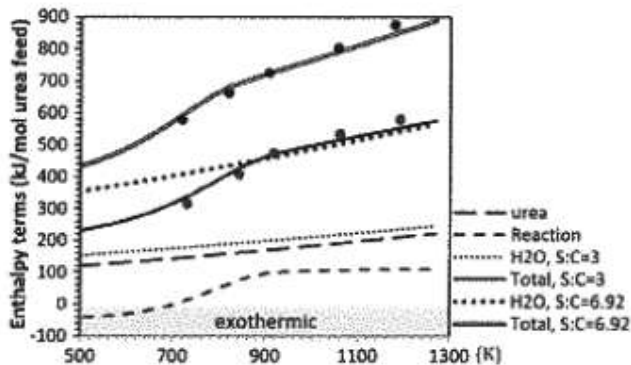• Existing distribution system.
• Not toxic, not flammable.

Fig. 6. Enthalpy of urea decomposition: compare between different models.

Table 5
Experimental test conditions.

Anodic compositions					Cathodic flow	Temperature	S:C
CO_2 (Nl/h)	CO (Nl/h)	H_2 (Nl/h)	N_2 (Nl/h)	H_2O (g/h)	Aria (Nl/h)	T (°C)	
6.86	13.38	46.62	20.93	11.87	400	700	1
5.90	14.17	45.83	20.26	11.69	400	750	1
5.27	14.75	45.25	20.07	11.94	400	800	1
12.05	7.99	52.01	20.13	38.90	400	700	3
11.14	8.87	51.13	20.03	39.35	400	750	3
10.35	9.65	50.35	20.01	39.91	400	800	3
15.63	4.37	55.63	20.01	98.69	400	700	6.92
14.94	5.07	54.93	20.00	99.19	400	750	6.92
14.26	5.74	54.26	20.00	99.71	400	800	6.92

Table 4
Stack characteristic.

Stack characteristic	
Number of cells	4
Cell dimension	100 × 100 mm
Active area	8000 mm²
Total active area	32,000 mm²
Anodic substrate	Ni/8YSZ cermet 1500 μm
Anode functional layer	Ni/8YSZ cermet 7–10 μm
Electrolyte	8YSZ 8–10 μm
Cathode functional layer	LSM/8YSZ 10–15 μm
Cathode current collector	LSM 60–70 μm
Interconnection	Crofer22APU
Anodic contact layer	Ni-mesh
Cathode contact layer	Perovskite type oxide (LCC10)
Sealing	Glass–ceramic (87YSZ20)

- Renewable production pathways are available.
- CO_2 can be stored.
- Competitive cost compared with others fuels.

while main drawbacks are:

- Not a carbon free fuel.
- Reforming is required.

3. Urea decomposition

As anticipated in previous paragraph the decomposition of Urea is a complex process. Thanks to the utilization of urea in SCR systems, thermal decomposition of urea was deeply studied in recent years. An alternative to thermal decomposition is the electro-catalytic oxidation of urea [36]. Via this latter process hydrogen is separated and, after purification, can be directly sent

Fig. 7. Carbon deposition study of tested compositions.

to any type of fuel cell. The main drawback is the electrical consumption, typical of such processes. In addition, due to the high operational temperatures, SOFCs may internally reform the fuel with a significant economical advantage and system simplicity. Thermal decomposition, deeply studied in SCR systems [37], is extremely complex at low temperature, 200 °C, obtaining several intermediate compounds which may cause solid depositions.

A complete study of urea decomposition at higher temperature was considered because SOFCs operate in the range 700–800 °C. Sebelius et al. [38] demonstrated that the increase of temperature strongly simplifies the decomposition model and intermediate products such as biuret or cyanuric acid disappear when the temperature reaches 500 °C. Fig. 3 shows the results obtained in the study.
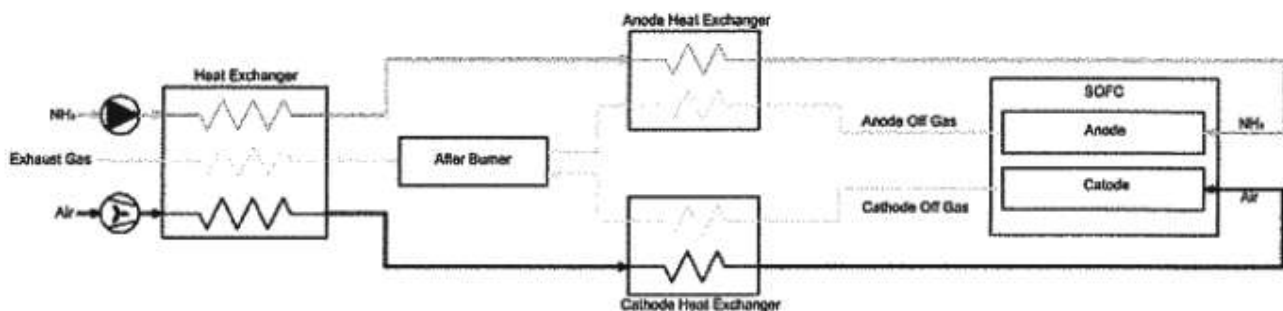
Fig. 8. System scheme.

Dupont et al. [39] performed a theoretical study of urea decomposition at SOFC operational temperature, considering water addition to enhance steam reforming as primary decomposition pathway and to manage and optimize carbon content in the compound. Theoretical steam reforming of urea is:

$$NH_2CONH_2 + H_2O \rightarrow N_2 + 3H_2 + CO_2 \qquad (v)$$
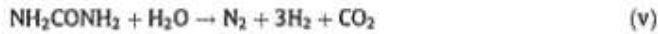
One of study result is reported in Fig. 4 were concentration of products is plotted as a function of temperature. Water is an additional resource requirement and introduces system complexity such as water management in terms of pressure, heating and water recovering. This could be a problem in isolated applications, or where the system operates far from a water source. This problem is, however, common to all systems where fuel steam reforming is necessary. A solution could come directly from the fuel due to the high dilution of urea in water. In such case energy density decreases but no additional source of water is required. The study also evaluates the efficiency, calculated as the ratio between chemical energy of hydrogen produced and all heat requirement for heating of reactants and reaction enthalpy. Urea has a great
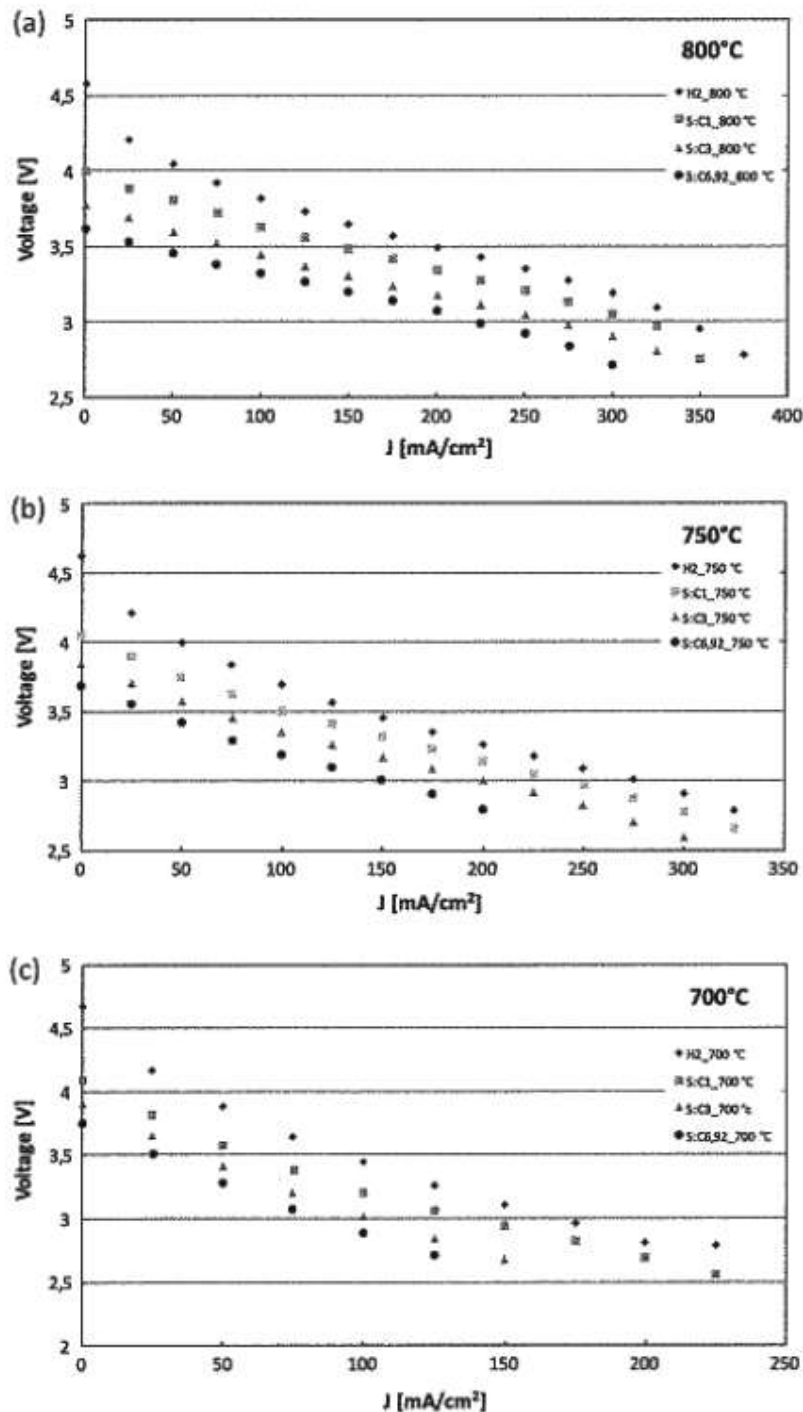
Fig. 9. Polarization results at 800 °C (a), 750 °C (b) and 700 °C (c).

potential, especially for small steam to carbon ratios, with similar enthalpy balance than steam methane reforming and a bigger advantage calculating the Gibbs free energy.

From those studies it is possible to deduce that urea is decomposed at high temperature in hydrogen, carbon dioxide, carbon monoxide, methane, nitrogen and ammonia. All these components can be fed to a SOFC that perfectly operates with them.

4. Methods

With the aim of simulating urea reforming, a commercial software, Aspen One, was used and a very simple model based on a

Gibbs reactor was developed varying steam to carbon (S:C) ratio and equilibrium temperature. Note that urea contains only one atom of carbon so steam to carbon and steam to urea ratios are the same. Dry products obtained for one mole of urea are plotted in Fig. 5. In detail, in Fig. 5a results are plotted at S:C = 3 at different temperature while in Fig. 5b temperature is constant at 700 °C and S:C varies from 0 (no water) to 6.92 that is exactly AdBlue concentration. Stoichiometry of urea reforming is S:C = 1.

Complete urea decomposition was obtained for all conditions but significant variations were obtained caused by reactions of methane steam reforming, water–gas shift of CO and ammonia cracking.

Fig. 10. Voltage decay at 800 °C (a), 750 °C (b) and 700 °C (c).

$$CH_4 + H_2O \rightarrow 3H_2 + CO \quad \text{methane steam reforming} \qquad (vi)$$

$$CO + H_2O \rightarrow H_2 + CO_2 \quad \text{water–gas shift} \qquad (vii)$$

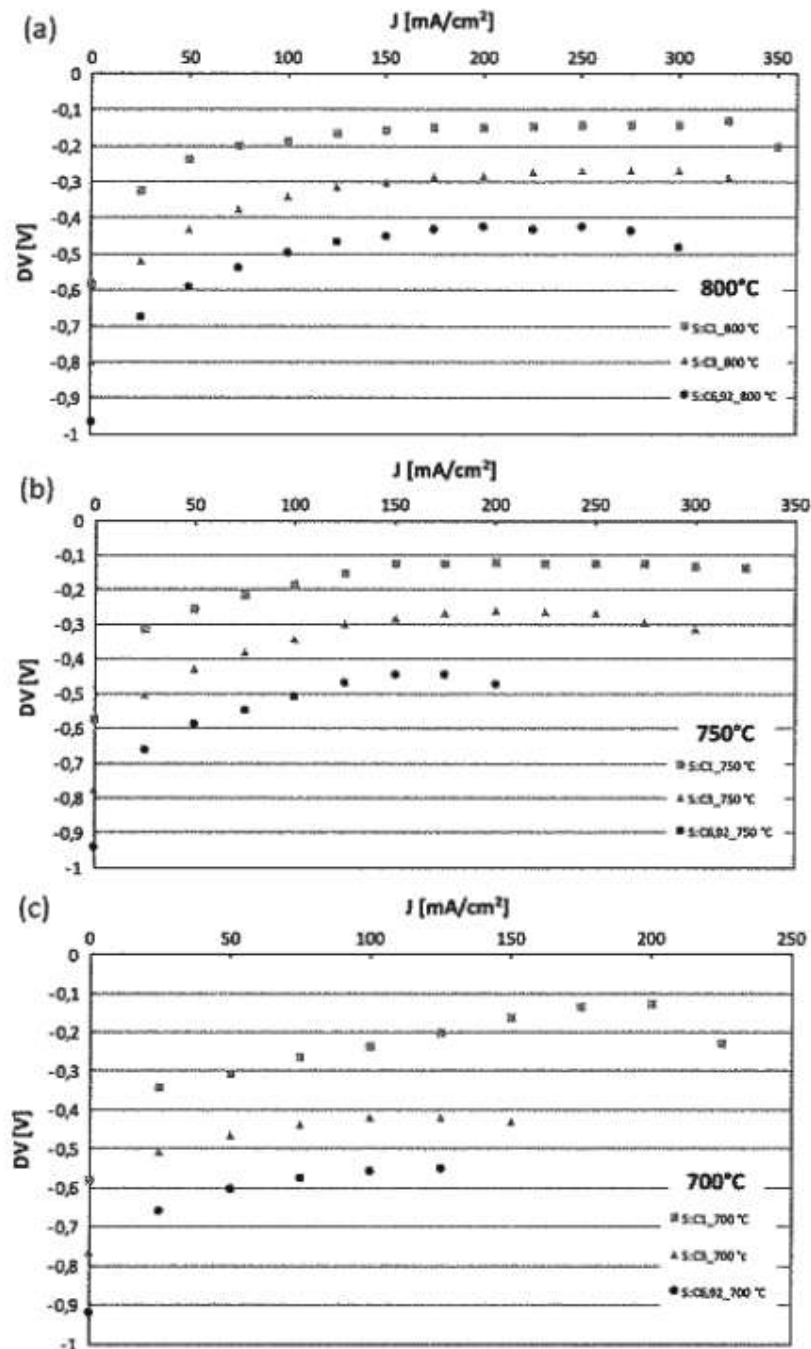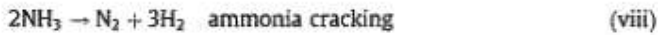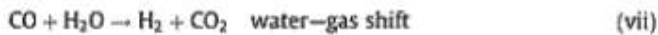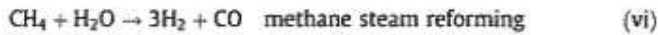$$2NH_3 \rightarrow N_2 + 3H_2 \quad \text{ammonia cracking} \qquad (viii)$$

Nitrogen is constant at all conditions once urea is completely decomposed because the only variation comes from reaction of ammonia whose concentration is an order of magnitude smaller than that of other compounds. Considering Fig. 5a, the maximum hydrogen mole ratio with urea was obtained at 700 °C but still smaller than three, which is the theoretical maximum from one reformed mole of urea (see Reaction (v)). Increasing the temperature, CH_4 and CO_2 decrease due to the increase of reverse water-gas shift. In Fig. 5b hydrogen content increases with S:C while CO decreases due to the contribution of the shift reaction. The drawback of a larger water dilution is the energetic cost of the heat required to vaporize and superheat such an amount of steam to 700 °C. In Fig. 6 the obtained results in dots are compared with reference [39], showing a good agreement. The figure reports overall enthalpy, included reaction heating, in terms of kJ per each mole of urea. The graph shows that the process is endothermic at both plotted S:C ratios and above 700 °C the only reaction component adsorbs heat. Such energy requirement can be used, like in systems based on steam methane reforming, to absorb part of the heat developed by the cell.

5. Experimental campaign

The model was used to define test conditions for the experimental activities. Considering an external reactor for urea decomposition, the fuel cell behavior was studied when operating with the equilibrium composition as predicted by Aspen simulation. The experimental study was performed in a stack supplied by Forschungszentrum Jülich. The stack is based on four planar ASC cells separated by Crofer interconnections. Anodic and cathodic feed gases, flow along parallel and counter flow channels. Table 4 reports all stack details.

The test rig was described in a previous paper [19]. Temperature is controlled by a furnace hosting the stack controlling operation temperature and by a cable heater used to raise inlet gas temperature to 650 °C. Each gas flow is controlled by a flow meter controller while water has a separate line where flow is controlled and water evaporated and mixed with other gasses. The electric current is controlled by an electronic load. Sensors are

placed in the stack to measure cell voltages and two temperatures, one close to anode inlet/cathode outlet (T1) and the other close to anode outlet/cathode inlet (T2).

The experimental measurements were performed by varying the operational temperature and the S:C ratio. To reduce number of test, three values for each parameter were selected for a total of 9 single test conditions. Considering previous considerations on urea decomposition three temperatures, 700, 750 and 800 °C, were selected. S:C equal to zero was not considered due to the high risk of carbon deposition. The three selected values of S:C were: S:C = 1 (stoichiometric), S:C = 3 (the best performing in [39]) and S:C = 6.92 (as in AdBlue). For the nine test conditions above, the molar compositions were calculated. To define the total flow, an equivalent hydrogen (H_{2eq}) of 1 Nl/min was used. H_{2eq} is defined in Eq. (1) as the equivalent amount of hydrogen obtained when all active compounds react to produce hydrogen considering Reactions (vi), (vii), and (viii).

$$H_{2eq}(mol) = [H_2 + 1,5 * NH_3 + CO + 4 * CH_4](mol) \qquad (1)$$

Cathode flow was kept constant at 400 Nl/h. Model results are summed in Table 5. Ammonia and methane were excluded because their amount was negligible.

Obtained compositions were compared to the ternary diagram to evaluate the risk of solid carbon formation in the cell. Fig. 7 shows obtained results: all nine cases are below carbon deposition boundary line. The temperature does not cause any difference, whereas the position of the three S:C values show that, as expected, the increase of water content reduces the risk of carbon deposition. The study shows an additional advantage of urea compared with other fuels, in particular methane, due to the presence of oxygen in the fuel.

6. System model

To perform a complete system evaluation a 0-D model was developed. This simple solution was used to calculate the energy balance and global efficiencies of a preliminary system using data from the experimental activity. The system scheme is shown in Fig. 8: one single passage in the stack is performed without recirculation. Both anode and cathode streams are heated up to reach SOFC operational temperature, by recovering heat from off gasses and from unburned fuel. During operation SOFCs can not use all the fuel and anode outlet still contains H_2 and CO, that can supply energy to the system. The ratio between reacting fuel and total fuel
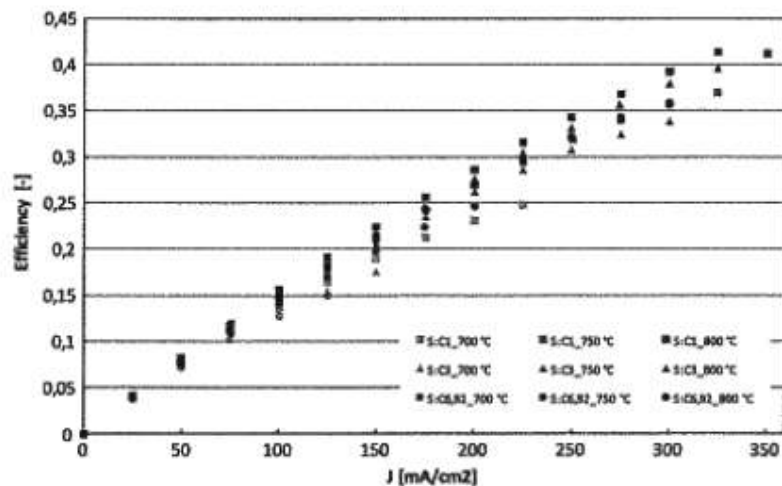
Fig. 11. Efficiency as function of current density of all test performed.
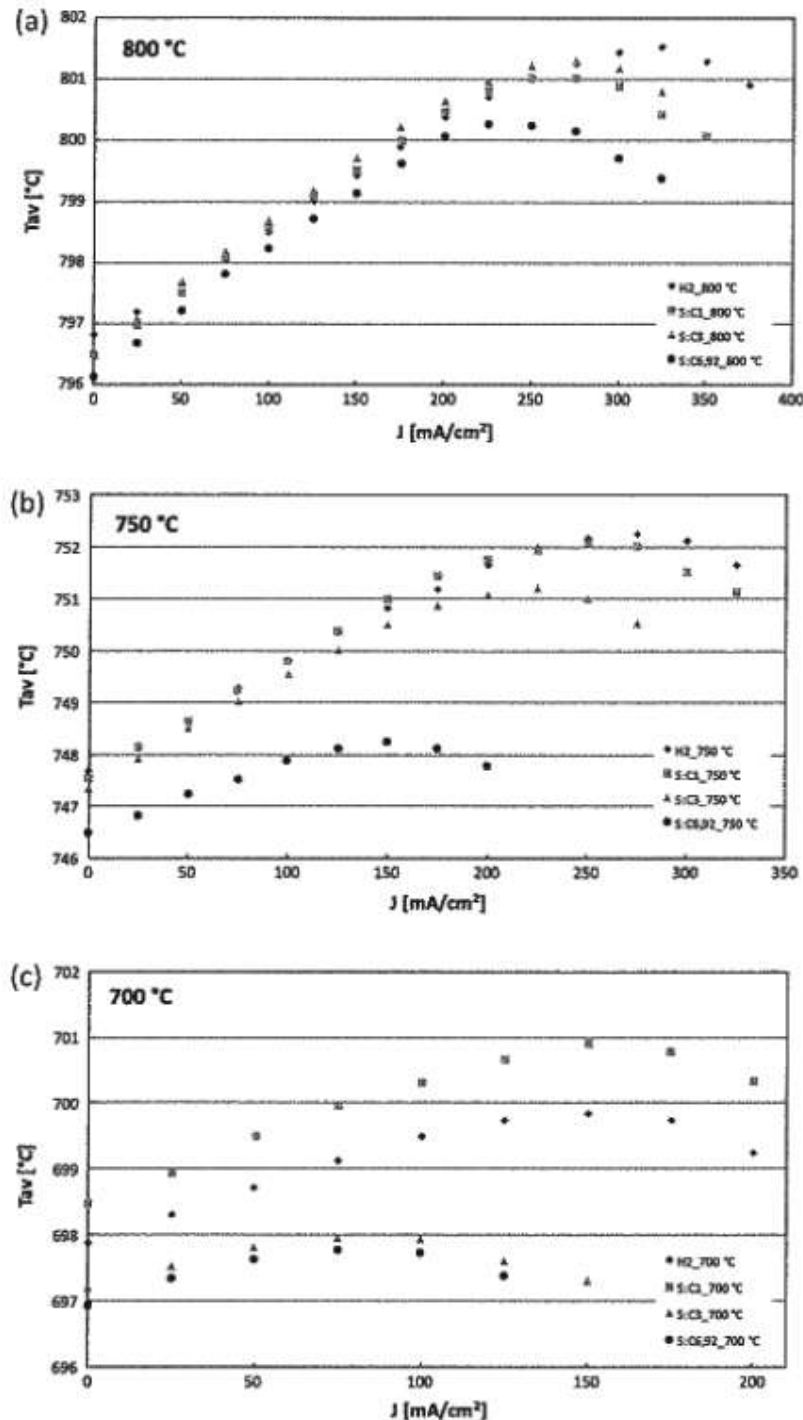
Fig. 12. Temperature behavior of polarization performed at 800 °C (a), 750 °C (b) and 700 °C (c).

flow is defined as fuel utilization (Uf). The cathode operates with an excess of air and the gas flow exiting the cell still contains a large amount of unreacted oxygen. Utilization of oxygen (Uox) is the equivalent of Uf on the cathode side. The fuel is a solution of urea diluted in water. From a thermodynamic point of view there is no difference if such solution is the original fuel or if it is mixed onsite, in both cases the heat duty to treat the urea mixture is equivalent. Both air and fuel entering the system are compressed to compensate circuit pressure losses but, while air is compressed

with a standard blower, urea, in a liquid state, is pressurized by a pump, obtaining a significant energy saving compared with gaseous fuels. Assumed compressor efficiency was 80% and compression work was calculated from air mass flow and a total pressure drop of 80 mbar. Two heat exchangers are used before and after the catalytic burner that recovers the additional energy from unreacted fuel and avoids the emission of toxic compounds such as CO and NH_3. The burner operates at 330 °C with off gases from the cell, that have to be cooled down. High temperature heat

recovery is realized in two separate heat exchangers operating separately with anodic and cathodic flows. Low temperature heat exchange is realized in one single device, where burner off gasses are used to heat up urea solution and air from ambient temperature. All heat exchangers are modeled with a heat transfer efficiency of 90%. In the low temperature heat exchanger the liquid is vaporized. The decomposition of urea is modeled in the anodic high temperature heat exchanger using Aspen model for chemical equilibrium calculations. Heat duty of reactions is included in the calculations.

The stack determines both anodic and gas flows. Once fuel inlet and fuel utilization are defined, chemical equilibrium is calculated at operational temperature. The stack is assumed as adiabatic and no heat losses are introduced. Air flow is calculated to balance stack temperature and adsorbs the heat produced during operation inside the stack. Such amount of heat is not lost but recovered in the heat exchangers. As a result, the utilization of oxygen is very low in the SOFCs. The definition of Uf allows to calculate, using

experimental data, the total current (see Eq. (2)) and operational voltage. Stack power is the product of total current and total voltage. Total current is calculated as follows:

$$I = \frac{U_f * F * k * n_{fuel}}{n_{cells}} \qquad (2)$$

where F is Faraday constant, k is the maximum available number of electrons from each mole of fuel, n_{fuel} is molar flow of fuel and n_{cells} total number of cells (in this case 4).

7. Results

Fig. 9 shows the polarization curves at 800 °C, 750 °C, and 700 °C respectively. The test was performed keeping the fuel and temperature unchanged and varying the current with a step of 2 A, for 2 min at each step. Data were sampled at 1 Hz. Plotted values
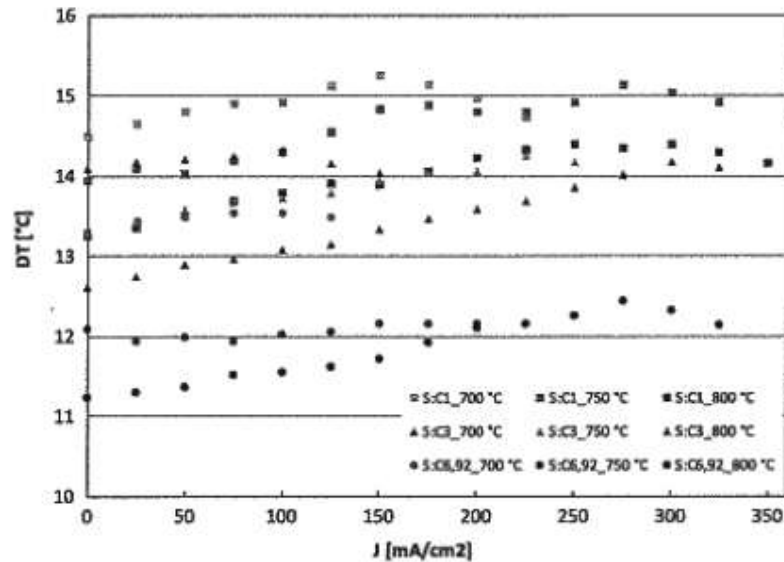

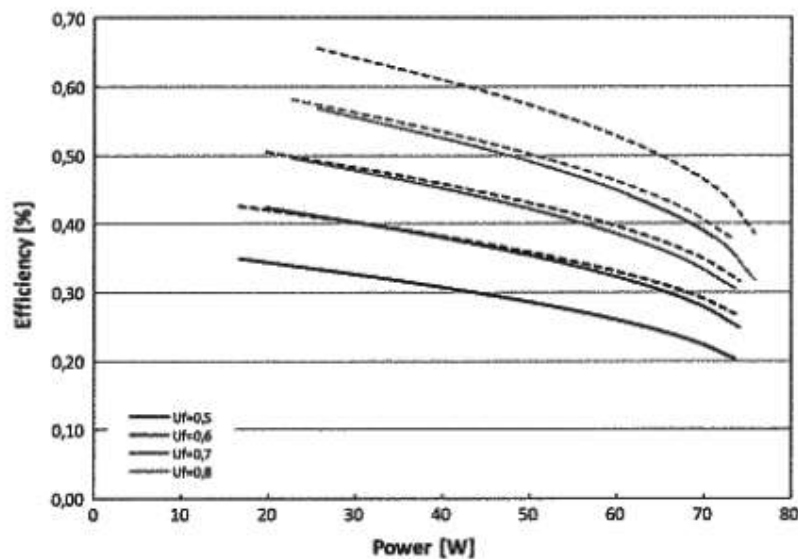Fig. 13. Temperature difference of test performed.

Fig. 14. Stack (dotted line) and system (dashed line) efficiency.

are average calculated at each step of current. In each graph, the three S:C compositions are compared with the reference composition of pure hydrogen. Stack performances in terms of OCV and cells resistance were not optimal due to the fact that the stack was already used in previous test camping. Results are still interesting and valuable in terms of trends and comparison with reference test.

All the tests show that, whichever the temperature, an increase of S:C corresponds to a reduction of performance. This is mainly related to the dilution of active compounds caused by the increase of steam content. The same reason justifies a lower performances compared with pure hydrogen flow, due to the presence of inert gases such as N_2, CO_2 even at low S:C compositions. The effect of dilution is well shown by the open circuit voltage (OCV), while along the curves the voltage difference is reduced due to new reactions that are activated when steam is produced by electrochemical reaction, such as the water–gas shift reaction of carbon monoxide. A deeper analysis is by possible studying voltage decay between the reference compositions and the studied ones. Fig. 10 shows voltage decay of all nine polarizations curves grouped at different temperatures. Performance reduction caused by urea dilution can be quantified easily and it results independent from temperature, confirming that water content is the main cause of decay. The experimental activities suggests that the best performing composition is that with the S:C = 1 and not the one with S:C = 3 as found in reference [39].

If we compare the same compositions at different temperatures we can notice that OCV values increase when temperature decreases. This is a typical behavior of high temperature fuel cell due to the increase of reversible potential at lower temperatures.

Fig. 11 shows the efficiency calculated as the ratio between power output and inlet chemical energy, which is the gas stream LHV. Values up to 40% efficiency were obtained, with the best performing conditions at high temperature and low S:C ratios.

Fig. 12 shows the stack temperature behavior at 800 °C, 750 °C and 700 °C respectively. Temperature is calculated as the average between the two thermocouple located in the stack.

All graphs show a trend of temperature similar to the reference one and the effect of the increase of power output and the relative heat developed inside the stack. Generally speaking, the increase of water decreases the average temperature, due to the larger amount of heat adsorbed by the inlet flows entering at a lower temperature (650 °C). It is interesting to note that when the temperature decreases, the S:C = 1 ratio shows a higher temperature than the reference case. This is caused by the water gas shift reaction that is exothermic and has a bigger effect at lower temperature. The same reaction also occurs at higher S:C ratios, but the effect disappears due to the dominant role played by water content.

Fig. 13 shows the temperature differences between the T1 (anode) and T2 (cathode) thermocouples. Those tests are useful to determine the temperature gradient in the stack that has to be as small as possible to reduce material thermal stresses during operation. The results show almost constant values of the temperature difference when the current density is changed, whereas it changes when varying the temperature and the S:C ratio. This supports the assumption that the optimal S:C ratio is the minimum one. The temperature difference, as absolute value, increases with temperature mainly because there is a scale factor with no specific relation with compositions.

7.1. Model results

Experimental results were used in the model to evaluate the overall efficiency. The efficiency was calculated at the best conditions of temperature, 800 °C, and Steam to Carbon ratio, S:C = 1.

A linear regression of experimental data was used to calculate voltage. The following equation was used:

$$V = -0.0041J + 3.9621 \tag{3}$$

where J is the current density.

The system efficiency was calculated by subtracting the compressor energy from power output. Fig. 14 shows the stack and system efficiency as a function of stack power output.

As in all SOFC systems, the efficiency increases in rated power operation. System efficiencies in the range of 40–60% were obtained at high Uf for all power outputs. Model results confirm the great potential of urea as a fuel in SOFC based power system.

8. Conclusions

The potential of urea as a fuel for fuel cell power systems was investigated. High energy density and low cost are optimal characteristics compared to other potential energy vector. In addition, two different sustainable pathways for urea production were indicated integrating CO_2 storage in solids. A system operating with diluted urea was modeled integrating the steam reforming of the solid fuel. Experimental activity demonstrated the operation of SOFC stack when fed with a composition simulating reformed urea reaching efficiencies up to 40%. System operating with urea can reach up to 55% efficiency at 800 °C and Uf = 0.8. The use of AdBlue as fuel is also interesting since it is an available, safe and low cost product, but energy density and stack performance are strongly penalized by the water content.

References

[1] Cinti G, Desideri U, Penchini D, Discepoli G. Experimental analysis of SOFC fuelled by ammonia. Fuel Cells 2014;14:221–30.
[2] Wojcik A, Middleton H, Damopoulos I, Van herle J. Ammonia as a fuel in solid oxide fuel cells. J Power Sources 2003;118:342–8.
[3] Maffei N, Pelletier L, Charland JP, McFarlan A. An ammonia fuel cell using a mixed ionic and electronic conducting electrolyte. J Power Sources 2006;162:165–7.
[4] Xie K, Ma Q, Lin B, Jiang Y, Gao J, Liu X, et al. An ammonia fuelled SOFC with a $BaCe_{0.9}Nd_{0.1}O_{3-\delta}$ thin electrolyte prepared with a suspension spray. J Power Sources 2007;170:38–41.
[5] Dekker NJJ, Rietveld G. Highly efficient conversion of ammonia in electricity by solid oxide fuel cells. J Fuel Cell Sci Technol 2006;3:499–502.
[6] Lunghi P, Bove R, Desideri U. Life-cycle-assessment of fuel-cells-based landfill-gas energy conversion technologies. J Power Sources 2004;131:120–6.
[7] Desideri U. Perspectives on the use of molten carbonate fuel cells with renewable energy sources. Invit. keynote lect. al first int conf fuel cell sci eng technol; 2003.
[8] Sánchez D, Monje B, Chacartegui R, Campanari S. Potential of molten carbonate fuel cells to enhance the performance of CHP plants in sewage treatment facilities. Int J Hydrogen Energy 2013;38:394–405.
[9] Guerra C, Lanzini A, Leone P, Santarelli M, Beretta D. Experimental study of dry reforming of biogas in a tubular anode-supported solid oxide fuel cell. Int J Hydrogen Energy 2013;38:10559–66.
[10] Laycock CJ, Staniforth JZ, Ormerod RM. Biogas as a fuel for solid oxide fuel cells and synthesis gas production: effects of ceria-doping and hydrogen sulfide on the performance of nickel-based anode materials. Dalton Trans 2011;40:5494–504.
[11] Spiegel R, Preston J. Technical assessment of fuel cell operation on landfill gas at the Groton, CT, landfill. Energy 2003;28:397–409.
[12] Desideri U, Lunghi P, Ubertini S. Thermodynamic analysis of a molten carbonate fuel cell systems using waste derived fuel gas. Am Soc Mech Eng Adv Energy Syst Div AES 2000;40:267–75.
[13] Desideri U, Lunghi P, Zepparelli F. A comparison between life cycle assessment of an mcfc system, An LFG – MCFC System, and traditional energy conversion systems. In: ASME 2004 2nd int conf fuel cell sci eng technol; 2004. p. 331–8.
[14] Desideri U, Lunghi P, Burzacca R. Assessment of reversible and irreversible effect on fuel cell performances due to polluted fuels. Fuel Cell Semin, November 18–20, Palm Springs, California, USA; 2002.
[15] Baron S, Brandon NP, Atkinson A, Steele B, Rudkin R. The impact of wood-derived gasification gases on Ni-CGO anodes in intermediate temperature solid oxide fuel cells. J Power Sources 2004;126:58–66.
[16] Omosun A, Bauen A, Brandon NP, Adjiman CS, Hart D. Modelling system efficiencies and costs of two biomass-fuelled SOFC systems. J Power Sources 2004;131:96–106.

[17] Colantoni S, Corradetti A, Desideri U, Fantozzi F. Thermodynamic analysis and possible applications of the integrated pyrolysis fuel cell plant (IPFCP). In: ASME turbo expo 2007 power land, Sea, Air; 2007. p. 427–36.

[18] Corradetti A, Desideri U. Analysis of biomass integrated gasification fuel cell plants in industrial CHP applications. ASME 2006 4th int conf fuel cell sci eng technol; 2006. p. 605–13.

[19] Penchini D, Cinti G, Discepoli G, Sisani E, Desideri U. Characterization of a 100 W SOFC stack fed by carbon monoxide rich fuels. Int J Hydrogen Energy 2013;38:525–31.

[20] Andreassi L, Toro C, Ubertini S. Modeling carbon monoxide direct oxidation in solid oxide fuel cells. J Fuel Cell Sci Technol 2009;6:21307.

[21] Shi Y, Li C, Cai N. Experimental characterization and mechanistic modeling of carbon monoxide fueled solid oxide fuel cell. J Power Sources 2011;196:5526–37.

[22] Chen W-H, Lin M-R, Leu T-S, Du S-W. An evaluation of hydrogen production from the perspective of using blast furnace gas and coke oven gas as feedstocks. Int J Hydrogen Energy 2011;36:11727–37.

[23] Lan R, Tao S, Irvine JTS. A direct urea fuel cell – power from fertiliser and waste. Energy Environ Sci 2010;3:438.

[24] USGS – Science for a Changing World. <http://minerals.usgs.gov/minerals/pubs/commodity/nitrogen/>, n.d. (accessed February 05 2015).

[25] Matijašević L, Dejanović I, Lisac H. Treatment of wastewater generated by urea production. Resour Conserv Recy 2010;54:149–54.

[26] Rollinson AN, Jones J, Dupont V, Twigg MV. Urea as a hydrogen carrier: a perspective on its potential for safe, sustainable and long-term energy supply. Energy Environ Sci 2011;4:1216.

[27] Zamfirescu C, Dincer I. Utilization of hydrogen produced from urea on board to improve performance of vehicles. Int J Hydrogen Energy 2011;36:11425–32.

[28] Automotive Grade Urea Solution – Quality Assurance Guidance Document; 2011. p. 1–22.

[29] National Institute of Standards and Technology; n.d., <http://webbook.nist.gov/>.

[30] Fch Ju. Fuel Cells and Hydrogen – Joint Undertaking – European Commission, Fuel Cell and Hydrogen Joint Undertaking (FCH JU); 2011.

[31] Methanex; n.d., <http://www.methanex.com/our-Business/pricing>

[32] NGVA Europe; n.d., http://www.sviluppoeconomico.gov.it/images/stories/prezzi_petroli/Struttura/Struttura_PI_2014_12_15.pdf.

[33] Sviluppo Economico – MISE; n.d., http://www.sviluppoeconomico.gov.it/images/stories/prezzi_petroli/Struttura/Struttura_PI_2014_12_15.pdf.

[34] Index Mundi; n.d., <http://www.indexmundi.com/commodities/?commodity=u>.

[35] as24.com. n.d., <http://www.as24.com/As24/as24-website.nsf/VS_SWIPUC/5AF53C07BF18F7A1C125783E002F6F527OpenDocument&UNI=354E9D6F29E37094C12577F300519DA0&LG=FR>.

[36] Vedharathinam V, Botte GG. Understanding the electro-catalytic oxidation mechanism of urea on nickel electrodes in alkaline medium. Electrochim Acta 2012;81:292–300.

[37] Bernhard AM, Peitz D, Elsener M, Wokaun A, Kröcher O. Hydrolysis and thermolysis of urea and its decomposition byproducts biuret, cyanuric acid and melamine over anatase TiO2. Appl Catal B Environ 2012;115–116:129–37.

[38] Sebelius S, Le TT, Pettersson LJ, Lind H. Identification of urea decomposition from an SCR perspective: a combination of experimental work and molecular modeling. Chem Eng J 2013;231:220–6.

[39] Dupont V, Twigg MV, Rollinson AN, Jones JM. Thermodynamics of hydrogen production from urea by steam reforming with and without in situ carbon dioxide sorption. Int J Hydrogen Energy 2013;38:10260–9.
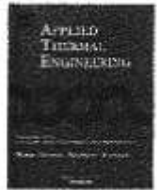
Research Paper

Solid oxide fuel cell performance comparison fueled by methane, MeOH, EtOH and gasoline surrogate C_8H_{18}

CrossMark

Vincenzo Liso [a,*], Giovanni Cinti [b], Mads P. Nielsen [a], Umberto Desideri [b]

[a] Department of Energy Technology, Aalborg University, Aalborg 9220, Denmark
[b] Department of Industrial Engineering, University of Perugia, Perugia, Italy

ABSTRACT

Carbon deposition is a major cause of degradation in solid oxide fuel cell systems. The ability to predict carbon formation in reforming processes is thus absolutely necessary for stable operation of solid oxide fuel cell systems. In the open literature it is found that the steam input is always considered in large excess compared to what required by the reforming process with the purpose of reducing carbon formation and avoiding rapid degradation of the cell performance. This makes it difficult to consistently compare system performance with different fuels. In this work, the molar compositions at equilibrium are calculated for a minimum steam to carbon ratio for each fuel type. We carry out a thermodynamic analysis of fuel/steam system using Gibbs Free Energy minimization method. A mathematical relationship between Lagrange's multipliers and carbon activity in the gas phase was deduced. Minimum steam required for the reforming process for each fuel was related to the heat required for the reforming process and fuel cell open circuit voltage. Furthermore, in an experimental test, steam reforming product compositions were used to evaluate and compare SOFC performance with different hydrocarbons. Comparing the model to the experimental activity, it is revealed that at temperatures exceeding 800 °C the gas composition is dominated by hydrogen and carbon monoxide for any of the fuels considered leading to similar cell polarization curves performance for different fuels. The main effect on the performance is related to OCV values which are dependent on different steam content for each fuel. It was concluded that the magnitude of the heat requested for the fuel reforming process is the major difference in system performance when comparing different fuels. However, reforming kinetic effects can become predominant rather than thermodynamics, especially at lower temperatures.

© 2016 Elsevier Ltd. All rights reserved.

1. Introduction

A solid oxide fuel cell stack (SOFC) is a promising technology for the conversion of chemical energy into electricity and heat. Due to the high temperature operation, this type of fuel cell can use different fuels such as natural gas, alcohols and gasoline. In particular, alcohols such as methanol or ethanol can be produced by renewable energy sources. In comparison with hydrogen, alcohols have the advantage of easy storage and safe handling. Alcohols show a reasonable energy density and may be appropriate particularly for applications in remote areas not covered by the electrical grid. Natural gas and gasoline have the advantage of the existing distribution and dispensing infrastructure.

In order to operate the cell, the fuel must be converted into hydrogen and lower the content of higher hydrocarbons in a pre-reformer or in the anode channel. Despite for SOFC-based system, complete internal reforming has been demonstrated to be possi-

ble; most systems for stationary application favor external pre-reforming, because it yields the highest amount of hydrogen [1–3].

For the pre-reforming process, steam reforming is considered one of best options since it delivers the highest hydrogen yield. However, carbon deposition can cause catalyst deactivation both in the reformer and fuel cell [4]. For this reason, thermodynamic analyses have been carried out in many studies to predict conditions under which carbon formation is inhibited during steam reforming [5,6].

It is demonstrated that carbon deposition can be minimized by providing sufficient H_2O in the fuel stream. However, steam generation increases system complexity and control. Therefore it is important from operational standpoint to identify operating conditions that avoid carbon formation and maximize the hydrogen yield while simultaneously minimizing the heat input required for steam generation and the endothermic reforming process [4,5].

Previous studies have focused on carbon deposition in reforming processes and at SOFC level. In particular, in [7,8] the cell performance for different fuels, namely methane, methanol, ethanol and gasoline, was analyzed by using chemical equilibrium models. Besides, an extensive theoretical and experimental work on fuel options for SOFC was carried out by Sasaki et al. in four reports

* Corresponding author. Tel.: +004521370207; fax: +45 9815 1411.
E-mail address: vli@et.aau.dk (V. Liso).

[6,7,9,10]. System considerations were not included in these works. On the other hand when systems based on SOFC are analyzed, only nominal operating conditions for temperature and steam to carbon ratio in the pre-reformer and fuel cell are considered [11]. In this case the most representative values based on those available in open literature are chosen.

In this work the reformation of different fuels for SOFC systems is compared using chemical equilibrium and system level analysis is drawn. The thermodynamic conditions for carbon formation are examined through the analysis of carbon activity in the reformate gas. A mathematical relationship between Lagrange's multipliers and the carbon activity, with reference to the graphite phase, is deduced, enabling to calculate the carbon activity in the reformer gas. From this, it is possible to predict if carbon will precipitate inside the reformer.

In most cases the equilibrium in steam reforming process is analyzed for a fixed and optimal steam to carbon ratio at different temperature (e.g. research work in [12–14]). Depending on the fuel, steam input is always in excess with the purpose of reducing the risk of carbon formation. This makes it difficult to consistently compare the reforming of different fuels in a system. In this work the molar compositions at equilibrium are calculated for a minimum steam to carbon ratio, making it easier to compare different fuels. For each fuel composition, the heat input for the endothermic reforming process is estimated and the fuel cell performance is calculated in terms of electromotive force (EMF) and maximum cell efficiency.

2. Methodology

Different mathematical methods were developed to explain and predict the behavior of solutions in dynamic equilibrium. Minimization of the Gibbs free energy and the law of mass action are among the most used especially in numerical simulations [15].

The Gibbs free energy minimization approach was introduced in 1958 by White et al. [16]; since then it has been used in most computer programs for chemical equilibrium calculations for its ability to generalize any reaction scheme (e.g. combustion, reforming). The law of mass action, on the other hand, requires that the stoichiometric reaction scheme is known. The two methods produce similar results.

In this study, the Gibbs free energy minimization was applied to analyze thermodynamic equilibrium of steam reforming of different fuels. The equilibrium conversion of CH_4, MeOH, EtOH and C_8H_{18} was studied in the temperature range of 250 °C–1000 °C. It should be noted that complete thermodynamic equilibrium was assumed. However, a deviation of the chemical composition may be registered in a reforming reactor due to slow kinetics of the steam reforming reactions.

For simplicity, only the following species were considered in the calculations in this study: $H_2(g)$, $H_2O(g)$, $O_2(g)$, $CO(g)$, $CO_2(g)$, $CH_4(g)$, solid graphite C, n-C_8H_{18} and alcohols CH_3OH and C_2H_5OH. Methane was chosen as representative of natural gas as it is its main constituent while n-octane and its isomers were considered to represent thermodynamic properties of gasoline. The model was developed in EES and the results were validated using CEA-NASA, a program that calculates chemical equilibrium product concentrations from any set of reactants and determines thermodynamic properties for the product mixture based JANAF thermochemical database. The total pressure considered for this simulation was 1 bar. Partial pressures were derived from the chemical compositions by assuming fuel gas species as ideal. As steam generation requires a significant energy input, the heat required to elevate the temperature of reactants (i.e. fuel and steam) to the reforming temperature was estimated.

Compared to the CEA-NASA software package, the mathematical formulation based on the Lagrange Method of Undetermined Multipliers can be reproduced in any numerical equation solver making this option more adaptable to different software platforms. The mathematical formulation has also the advantage to explicitly impose zero thermodynamic carbon activity (i.e. no carbon formation).

In order to consistently compare the amount of steam required in the reforming process for different fuels, the minimum steam-to-carbon ratio that inhibits carbon formation was calculated using each temperature. This is obtained imposing zero thermodynamic carbon activity in the steam reforming equilibrium model.

Even though the reforming process is usually achieved for different fuels at different temperatures, we have assumed one temperature of reforming for all types of fuel. In fact as the reforming process is comprised of mainly equilibrium limited reactions, the high temperature in the cell channels would lead to complete the reforming process reactions.

The electromotive force represents the open circuit voltage. The irreversible voltage loss (i.e. activation, ohmic and concentration polarizations) is mainly a function of current density and stack temperature. Since these parameters are equivalent in each stack and the main scope of this research is a thermodynamic comparison of different fuels, it was assumed that the EMF is a good indicator of the fuel cell performance.

3. Thermodynamic model definition and validation

3.1. Model definition

The equilibrium state of a chemical reactive system is characterized by a minimum value of the total Gibbs free energy of a reactants and products mixture at a specified temperature and pressure. If it is assumed that the condensed species possess negligible volume compared to the gas phase in a chemical product mixture, the equation of state for the product species can be simplified by assuming ideal gas behavior for the entire mixture (i.e. $PV = nRT$).

If the mixture obeys the ideal gas law, the Gibbs free energy of a mixture can be expressed by the product of the chemical potential, μ_i, and the number of mole, n_i, of each i-th gas species.

$$G = \sum_{i=1}^{c} n_i \mu_i \qquad (1)$$

The chemical potential of an ideal gas mixture is defined as:

$$\mu_i = \mu_i^\circ + R_{Univ} T \ln\left(\frac{y_i P}{P^\circ}\right) \qquad (2)$$

where μ_i° is the chemical potential of i-th species at temperature T and standard state pressure P°, which is normally chosen to be 1 atm, and can be expressed as:

$$\mu_i^\circ = h_i^\circ - T s_i^\circ \qquad (3)$$

$y_i P / P^\circ$ in Eq. (2) represents the activity, a_i, for each of the species, namely C, H and O:

$$a_i = \frac{y_i P}{P^\circ} \qquad (4)$$

a_i can be used to study the carbon deposition. In particular if carbon activity, a_c, is greater than unity, the gas phase is not in equilibrium and carbon deposition may occur. If carbon activity is less than one, carbon formation will be not be feasible [17].

As solid carbon, only graphite was taken into account for simplicity, whereas various carbon-based materials such as amorphous

carbon, carbon nanotubes, and carbon nanofibers could have slightly different thermochemical properties [18].

When solid carbon (Graphite) is involved in the system, the chemical equilibrium takes place between substances in more than one phase. As the solid species does not contribute to the system pressure, the Gibbs free energy can be assumed equal to the standard Gibbs free energy of formation, i.e. $\mu_{C(S)} = \mu^\theta_{C(S)}$.

Therefore the member of moles of each atom that is present (E_j) can be determined. The number of moles must remain constant as required by mass conservation law. The initial number of moles of each element is given by:

$$E_{0,j} = \sum_{i=1}^{C} n_{0,i} e_{i,j} \quad \text{for } j = 1 \ldots E \tag{5}$$

where $n_{0,i}$ is the initial number of moles of each substance and $e_{i,j}$ is the number of moles of the element j in a mole of substance i, and E is the total number of atoms. The number of moles at equilibrium is:

$$n = \sum_{i=1}^{C} n_i \tag{6}$$

and the molar fraction of each gas component is given by:

$$y_i = \frac{n_i}{n} \quad i = 1 \ldots C \tag{7}$$

The Lagrange Method of Undetermined Multipliers is implemented by the following equations:

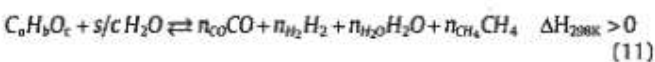$$\varphi_j = \sum_{i=1}^{C} n_i e_{i,j} - E_{0,j} = 0 \quad \text{for } j = 1 \ldots E \tag{8}$$

$$\mu_i + \sum_{j=1}^{E} \lambda_j e_{i,j} = 0 \quad \text{for } i = 1 \ldots C \tag{9}$$

The nonlinear system (Eqs. 1–9) was solved by using the Newton–Raphson method implement in EES, Engineering Equation Solver. As this problem is convex, the global minimum of this equation system is independent from the initial guess values [19].
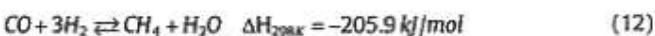
Remembering that $\mu_i = G_i^\theta + RT \ln a_i$, we can calculate the carbon activity in the reforming process using Eq. (9) as follows:

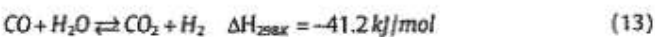$$a_c = e^{-(\mu_c^\theta + \lambda_c)/RT} \tag{10}$$

The overall reforming mechanism can be divided in three reactions: the endothermic steam reforming reaction (11), and the exothermic methanation reaction and the slightly exothermic water gas shift reaction (13):

$$C_a H_b O_c + s/c\, H_2O \rightleftarrows n_{CO}CO + n_{H_2}H_2 + n_{H_2O}H_2O + n_{CH_4}CH_4 \quad \Delta H_{298K} > 0 \tag{11}$$

Methanation reaction:

$$CO + 3H_2 \rightleftarrows CH_4 + H_2O \quad \Delta H_{298K} = -205.9 \, kJ/mol \tag{12}$$

Water gas shift reaction:

$$CO + H_2O \rightleftarrows CO_2 + H_2 \quad \Delta H_{298K} = -41.2 \, kJ/mol \tag{13}$$

Therefore the only species present at equilibrium are fuel ($C_a H_b O_c$), steam (H_2O), hydrogen (H_2), carbon monoxide (CO), methane (CH_4), carbon dioxide (CO_2), water (H_2O) and graphite (C). Graphite is formed via the Boudouard reactions scheme from carbon monoxide at the catalyst surface. This reformer process is well suited of steady-state operation and can deliver relatively high concentrations of hydrogen. The most important parameter of reforming is the initial gas composition that consists of fuel and steam, i.e. $C_a H_b O_c + S/C\, H_2O$ in Eq. (11), where the steam-to-carbon ratio, S/C, is defined as:

$$S/C = \frac{n_{H_2O}}{a \cdot n_{C_a H_b O_c}} \tag{14}$$

where a indicates the number of carbon atoms in the hydrocarbon. The electrochemical charge-transfer reactions in a SOFC take place in the membrane-electrode assembly (MEA). During this process, the Gibbs free energy (or chemical potential energy) of the global reaction of fuel and oxidizer is converted into electricity. The reversible cell potential (Nernst Potential) E_{rev} between fuel and oxidizer streams is calculated as:

$$E_{rev} = -\frac{\Delta G^\circ}{n_e F} + \frac{RT}{n_e F} \ln\left(\frac{p_{H_2} p_{O_2}^{1/2}}{p_{H_2O}} \right) \tag{15}$$

where ΔG° is the is the standard-state Gibbs free energy change associated to the global oxidation reaction occurring in the cell anode-side, i.e. $H_2 + \frac{1}{2}O_2 \rightarrow H_2O$. E_{rev} is also used to predict the open circuit voltage, OCV. It is important to recall that as air passes through a fuel cell, the oxygen is used, and so the partial pressure will be reduced. Similarly, the fuel partial pressure will often decline, as the proportion of fuel reduces and reaction products increase. Besides, parasitic process may reduce the E_{rev} voltage. In practice lower OCV values are measures compared to those calculated by Eq. (15). The reversible potential, however, varies along the channel length as the fuel is depleted and diluted.

The decrease in power density is due to the fuel dilution effect; diluted fuel results in a lower average current density, and for the cases studied here power density solely depends on the current density due to the constant operating voltage during data logging. The Nernst potential is the voltage which drives reversible electrode reactions. This reversible voltage, generated by the overall cell reaction, is a function of the local temperature, pressure, and reactant concentrations. As reactants are utilized, their concentrations change. Since the Nernst potential is dependent upon the concentrations of reactants, it varies with the degree of utilization. Because of depletion and dilution of the fuel and oxidizer streams, this potential can vary along the length of the cell. Each of the over-potentials increases with increasing current density. Irreversible voltage loss is mainly a function of current density and stack temperature. Since these parameters are equivalent in each stack, it is assumed that the Nernst potential of each stack would be reduced by the same amount.

The maximum SOFC efficiency was calculated as:

$$\eta = \frac{qE}{\Delta H^\circ} \tag{16}$$

where F is the Faraday constant, E_{rev} is the reversible cell potential described in Eq. (15) and ΔH° is the standard enthalpy change associated to the global oxidation reaction occurring in the cell anode-side, i.e. $H_2 + \frac{1}{2}O_2 \rightarrow H_2O$.

3.2. Model validation

The chemical equilibrium model was validated comparing the code developed in EES – Engineering equation solver – and the CEA-NASA computer program [20]. The results are shown in Table 1. In the calculation only species with molar fraction more than 5.0E-06 is considered. The error between the EES model and the CEA-NASA computer program reference was computed as a relative difference which takes the "sizes" of the molar fractions into account.

Table 1

Comparison of the results obtained by the model and CEA-NASA code for CH4, MeOH, EtOH and C8H18 at (Steam/Fuel of Reactant = 2.5; P = 1 atm).

Molar fraction (X)	500 °C			800 °C		
	CEA-NASA	Model	Diff%	CEA-NASA	Model	Diff%
CH4	0.142	0.142	0.154	0.001	0.001	1.098
H2O	0.414	0.413	0.103	0.222	0.222	0.020
CO	0.013	0.013	0.383	0.129	0.129	0.008
CO2	0.078	0.078	0.102	0.052	0.052	0.038
H2	0.352	0.352	0.130	0.596	0.596	0.008
C	0	0		0	0	
CH3OH	0	0		0	0	
CH4	0.079	0.079	0.238	0.000	0.000	0
H2O	0.489	0.489	0.081	0.369	0.369	0.012
CO	0.014	0.014	0.568	0.096	0.096	0.021
CO2	0.117	0.117	0.008	0.085	0.085	0.023
H2	0.299	0.300	0.130	0.449	0.449	0.015
C	0	0		0	0	
C2H5OH	0	0		0	0	
CH4	0.171	0.200	15.512	0.001	0.001	8.612
H2O	0.365	0.333	9.406	0.186	0.146	24.029
CO	0.023	0.025	11.794	0.184	0.209	13.005
CO2	0.141	0.148	4.1818	0.066	0.056	15.127
H2	0.299	0.294	1.646	0.563	0.586	3.975
C	0	0		0	0	
C8H18	0	0		0	0	
CH4	0.226	0.200	12.305	0.0197	0.020	1.098
H2O	0.139	0.130	7.6322	0.0088	0.012	0.018
CO	0.007	0.007	3.3426	0.1193	0.116	0.008
CO2	0.020	0.020	1.3138	0.0020	0.003	0.038
H2	0.264	0.300	12.683	0.5685	0.561	0.008
C	0.343	0.346	1.0421	0.2862	0.288	0.008

The comparison is expressed as a ratio and is a non-dimensional number expressed as percentages.

$$Diff\% = \frac{|X_{CEA} - X_{EES}|}{(|X_{CEA}| + |X_{EES}|)/2} \cdot 100 \tag{17}$$

4. Results

4.1. Minimum reactants S/C ratio comparison

The minimum steam-to-carbon ratio was determined imposing carbon activity, a_c, in Eq. (10) equal to unity.

$$a_c = e^{-(\mu_c^0 + \lambda_c)/RT} = 1 \tag{18}$$

This ensures that the molar fraction of C (graphite) is 0 in the considered temperature range.
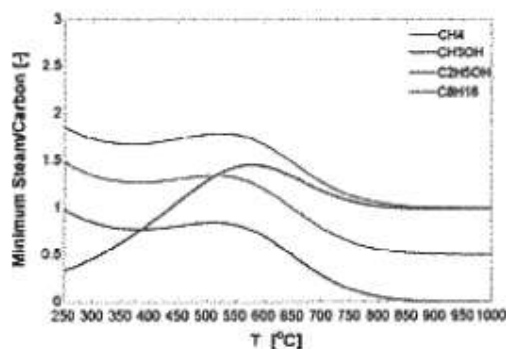

Fig. 1. Minimum steam to carbon ratio of the reforming reactants at different temperatures.

Fig. 1 shows the minimum steam to carbon ratios at temperature between 250 and 1000 °C for all chosen fuels. This temperature range was chosen as representative because it includes both the steam reforming and the solid oxide fuel cell operating temperature ranges. With an increasing carbon to hydrogen ratio, the required S/C increases.

The carbon deposition region for methanol lies at lower temperatures while the region for methane lies at intermediate and higher temperatures. The amount of H_2O (g) formed from the methanol-based fuels shown in Fig. 1 is much higher than that from the methane-based. This feature may be understood as alcohols could be regarded as hydrated hydrocarbons. Therefore, compared to alkanes (C_nH_{2n+2}), less amount of H_2O is needed to prevent carbon deposition especially at higher temperature.

Methanol has a smaller area of carbonization than all other cases because it contributes the minimum number of carbon atoms per mole and requires the smallest stoichiometric factor for complete reforming.

With increasing carbon number of alcohols, the number of hydrogen and oxygen per carbon atom in an alcohol molecule decreases. This reveals that the temperature region of carbon formation slightly expanded with increasing carbon number, so that carbon deposition is thermodynamically expected.

SOFCs generally operated at temperatures above 800 °C. However, the stack could also encounter carbon deposition during preheating and pretreatment processes of fuel gases between room temperature and the operational temperature. In the SOFC temperature range of operation, the "driving force" for the carbon deposition reaction decreases with temperature. In practice, carbon deposition may be highly dependent also on kinetics. In fact, higher reforming reactivity occurs at high temperature and inlet steam concentration.

In Fig. 2, conversion at equilibrium is calculated by solving the coupled set of equations for minimum steam-to-carbon ratio at each specific temperature. Considering product distribution from the steam reforming, the yield of hydrogen production and carbon
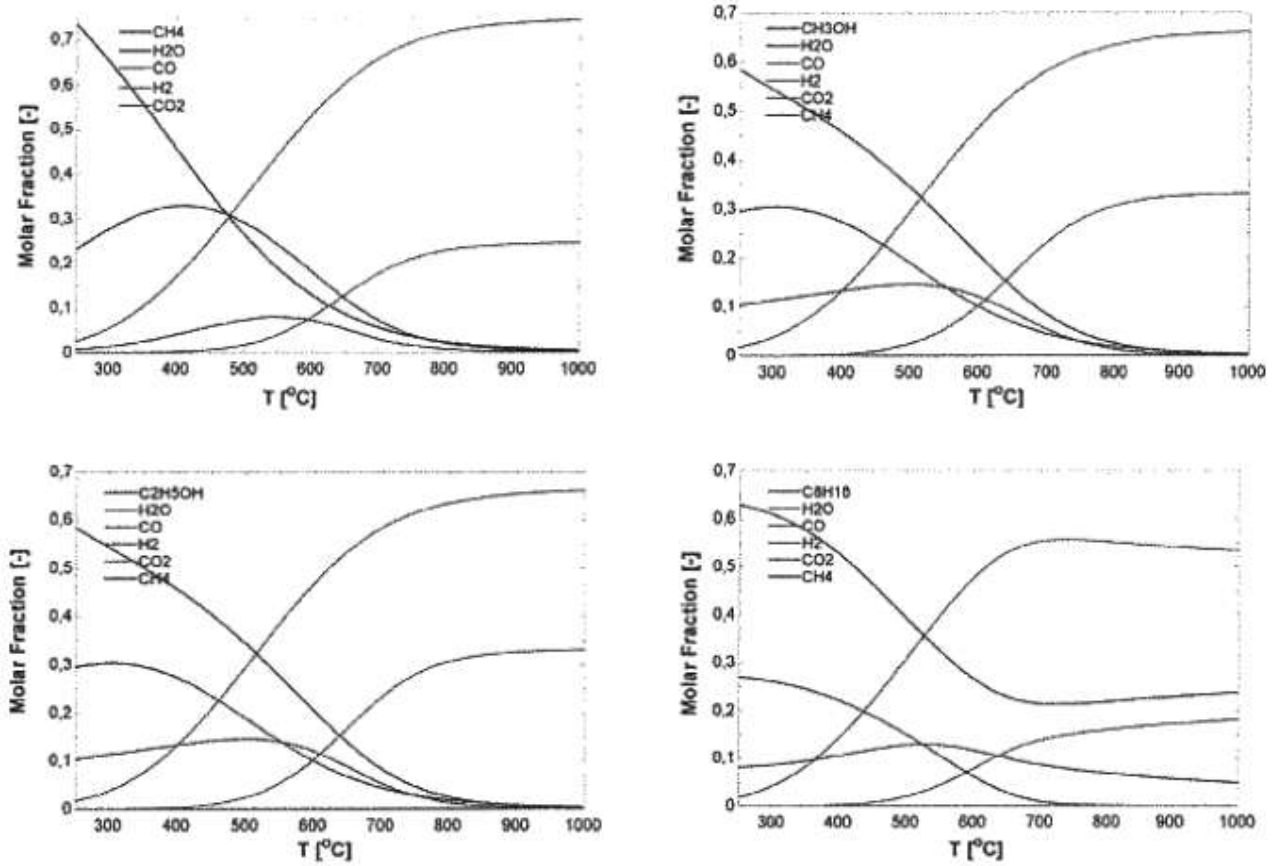
Fig. 2. Gas compositions at equilibrium for CH_4, CH_3OH, C_2H_5OH and C_8H_{18} when minimum steam to carbon ratio of the reactant is considered.

monoxide fraction increases with increasing temperature, whereas the carbon dioxide and methane production fraction decreases. Even if there is an uncertainty in choosing a single temperature to represent a real reformer which will have temperature differences among multiple catalyst tubes, an equilibrium analysis will still provide a more realistic estimation compared to other methods such as the extent of reaction.

The steam, hydrogen and carbon dioxide fraction increases with increasing inlet steam concentration, whereas the carbon monoxide fraction decreased. The yield of methane production is reduced at higher temperatures. It should be noted that the changes in the fractions of hydrogen, carbon monoxide, and carbon dioxide are mainly due to the influence of the mildly exothermic water–gas shift reaction $(CO + H_2O \rightarrow CO_2 + H_2)$, whereas the decrease of methane production is due to the further reforming to carbon monoxide and hydrogen. Alcohols show very similar molar fraction composition at high temperatures. The higher the molar carbon content in the fuel, the higher the reforming factor at a given temperature.

4.2. Steam reforming heat duty

Due to the endothermic nature of the overall reactions, the steam reforming of hydrocarbons requires a significant heat input to obtain the desired conversion to hydrogen. In this study, we define the heat duty as the heat required for the reforming reactions plus the heat required to heat the fuel to the required reforming temperature and the heat input to generate steam:

$$\dot{Q}_{Duty} = \Delta H_{Reac}^T + \Delta \dot{Q}_{Fuel}^{25 \rightarrow T} + \Delta \dot{Q}_{H2O}^{25 \rightarrow T} \tag{19}$$

In Fig. 3 the heat required to preheat fuel and water to the reforming temperature is shown (i.e. $\dot{Q}_{Fuel}^{25°C \rightarrow T} + \dot{Q}_{H_2O}^{25°C \rightarrow T}$). As the amount of steam is always larger in the fuel stream, this heat input is mainly
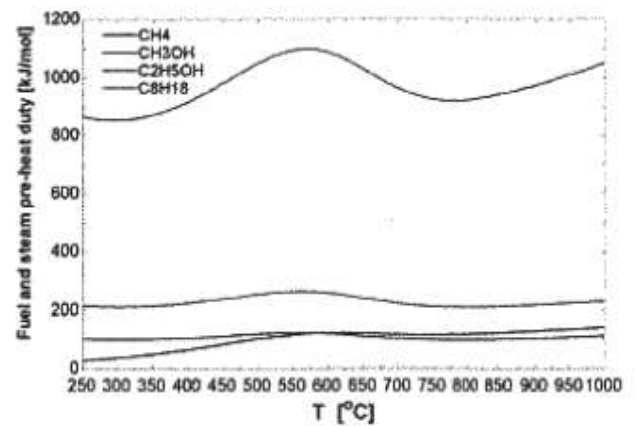

Fig. 3. Heat required to pre-heat fuel and water up to the reforming temperature in case of minimum steam to carbon ratio of the reactant.
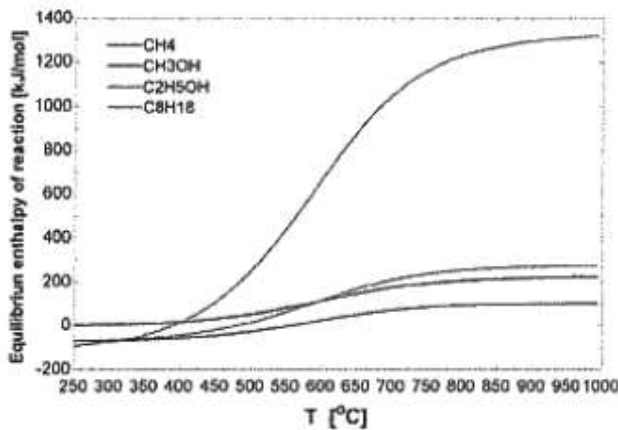
Fig. 4. Steam reforming heat of reaction of different fuels at different temperatures.

Table 2
Anode inlet gas composition for experimental activity at 800 °C considering minimum S/C of the reactant.

	H_2	CO	CO_2	CH_4	H_2O	Inlet S/C ratio
CH_4 (methane)	71.9%	23.01%	0.71%	2.36%	2.06%	1.01
CH_3OH (methanol)	63.6%	30.83%	1.27%	1.85%	2.44%	0.05
C_2H_5OH (ethanol)	63.6%	30.83%	1.27%	1.85%	2.44%	0.55
C_8H_{18} (gasoline surrogate)	64.9%	29.61%	1.17%	1.92%	2.40%	1.05

4.3. Cell performance and efficiency

The electro motive force is governed by Eq. (15) which depends on the types of fuel. The decrease in H_2 concentration is one of the main reasons explaining lower EMF and lower electrochemical performance [21]. The influence of temperature on the hydrogen partial pressure is logarithmic, which means that the voltage is not largely affected by the fuel composition but only depends on the working temperature as shown in Fig. 5.

4.4. Experimental test

Steam reforming product compositions were used to evaluate and compare SOFC performance with different hydrocarbons. The anode gas composition was calculated at chemical equilibrium at 850 °C. The used compositions are reported in Table 2. The table also lists the steam to carbon ratio (S/C) at equilibrium for the reforming reaction. The minimum S/C-ratio to thermodynamically avoid carbon formation was chosen in each case scenario. Since at high temperatures methanol and ethanol give same equilibrium composition, from now on only the ethanol composition is considered. For this reason only ethanol was considered for the experimental analysis.

The test was performed in a single SOFC cell, electrolyte supported. Fuel gas was normalized in order to have the same low heating value for each composition. Reference flow rate of hydrogen was selected equal to 36.14 mol/min. Air rate at cathode was kept constant during all tests at 120.48 mol/min. Both these values are indicated by cell supplier, Next Cell, as operative condition of the cell. With these fuel and air flow streams, utilization of fuel (U_f) is 20% at 500 mA/cm² and the utilization of oxygen (U_{ox}) at same current density is 14%. While U_{ox} is similar with operative conditions U_f is much lower than common values (around 0.8). Furnace temperature was fixed to 850 °C which is the temperature of operation of an electrolyte supported SOFC. Obtained gas stream values are reported in Table 3. Reference H_2 standard composition was used to compare results.

The cell is located inside a furnace and both cell and furnace temperatures are monitored. During the tests, temperature, gas flow rates, current and voltage are measured and controlled. Inlet anode gas is heated up using an electric heating cable which regulates the fuel inlet temperature in order to avoid steam condensation.

The anode current collector mesh is realized in nickel while at the cathode side it is made of silver. A sealing is placed around the mesh to avoid gas leakages. An electronic load in series with a power

used to generate steam. At high temperatures, a lower S/C-ratio is required. A lower amount of steam leads to less heat required and hence an almost flat trend of the heat duty over a large range of temperatures.

In Fig. 4, the enthalpy of reaction at different temperatures ΔH_{Reac}^I is shown. Higher temperatures require more heat for the reforming process. At low temperature ranges, the mildly exothermic methanation (Eq. 11) and shift reactions (Eq. 12) are more dominating than the steam reforming reaction causing negative values for ΔH_{Reac}^I. At high temperatures, n-octane shows higher heat of reaction due to greater bond energy of this molecule.
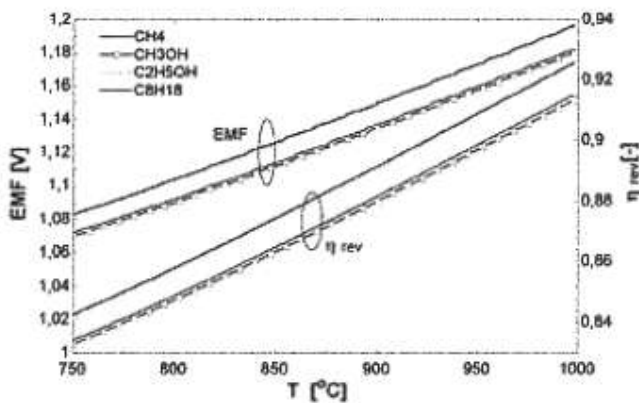

Fig. 5. Cell electromotive force e.m.f. and reversible efficiency when fuel composition produced by reforming process with minimum steam to carbon ratio.

Table 3
Anode inlet gas composition for experimental activity at 850 °C.

	Flows [mol/min]					Total anodic [mol/min]	Air [mol/min]
	H_2	CO	CO_2	CH_4	H_2O		
CH_4	24.90	7.97	0.24	0.82	0.75	34.68	120.48
C_2H_5OH (ethanol)	22.58	10.94	0.45	0.66	0.76	35.39	120.48
C_8H_{18} (gasoline surrogate)	22.95	10.47	0.41	0.68	0.76	35.28	120.48
Hydrogen	36.14	0	0	0	0.79	36.14	120.48

Table 4
Cell specifications.

Cell type	Electrolyte supported – planar
Dimension	5 cm × 5 cm
Active area (measured)	3.9 cm × 3.3 cm = 12.87 cm^2
Anode	50 μm Ni-GDC/Ni-YSZ multi-layer
Electrolyte	150 μm Ni-GDC/Ni-YSZ
Cathode	50 μm LSM/LSM-GDC multi-layer

supply permits cell current control and measurement. The test rig includes a cell voltage sensor and thermocouples located inside the cell housing and along the gas line. The cell temperature was calculated as the average between the temperatures measured inside the anodic and cathodic housing. Finally, the mechanical load is placed over the cathode and is regulated to obtain the required compression of the fuel cell assembly. Most important cell specifications are reported in Table 4.

Cell startup was carried out by following the procedure provided by the supplier. Selected gas compositions were delivered to the cell for one hour at open circuit voltage (OCV) to achieve voltage and temperature stabilization; after this phase, a complete cell polarization curve was performed. Each polarization was executed starting from OCV and increasing current with a 0.5 A step corresponding to 38.8 mA/cm^2. Each polarization point was kept for 2 minutes in order to reach steady-state operation. The procedure was interrupted when 0.6 V was reached. Data were logged at 0.5 Hz and grouped for each step of current. Average values for each condition were calculated and the distribution of data was verified to have a standard deviation below 1%. Polarization was performed in forward and reverse mode to reduce cell stress and to verify any hysteresis. No significant variation was ever measured between the two curves.

Cell voltages and temperatures are reported in Fig. 6. Reformed fuels produce similar OCV values due to the fact that the sum of concentration of inert gases, such as H_2O and CO_2, does not participate in the electrochemical reactions. This is in accordance with thermodynamic calculation results presented with OCV ranges

around 1.1 V. A detailed data fitting with the thermodynamic model was not considered relevant for the scope of this research as the purpose of this study was to explore fuel cell response to different fuels rather than a full polarization curve model validation.

As expected, the anode temperature is higher when using pure hydrogen as fuel compared to other fuels. In this case, the heat generated by the electrochemical reaction is not absorbed by the endothermic steam reforming reactions like in the other cases.

To have a detailed analysis of the results, polarization data were plotted as the difference between each of the three tested compositions which were compared with the reference. A voltage-decay was thus defined as the difference between the measured data and the reference composition for each value of current density. In Fig. 7 these results are plotted. It is important to note that all positive and negative decays are below 5 mV, so the results are quire similar. Going into details we can observe that the OCV values are affected by the hydrogen concentration and ethanol and gasoline, where the hydrogen concentration is smaller and differs from methane. Specifically, gasoline and ethanol decay at OCV compared to reference is higher due to smaller H_2 concentration. This difference is reduced along polarization curve. We can imagine that when water is produced due to the electrochemical reaction, the shift reaction contributes to reduce difference in pure hydrogen concentration. For values above 100 mA/cm^2 the decay becomes negative, meaning that reformed fuels perform better than the reference. This difference is mainly due to the fact that the reference test was performed after the others and the cell and a small degradation occurred.

In conclusion, the experimental activity shows that the defined compositions subject to these conditions have similar effect both in terms of performance and in terms of thermal balance. A reduction of current affects polarization performance mainly with an increase of OCV and an increase of internal resistance with a general effect of reducing performances. If the reforming temperature is reduced, the composition will have minimum change in terms of the inlet gas LHV and consequently in terms of performance. The parameter that strongly affects the performance in the cell is the steam content: if reforming conditions are kept so to have minimum
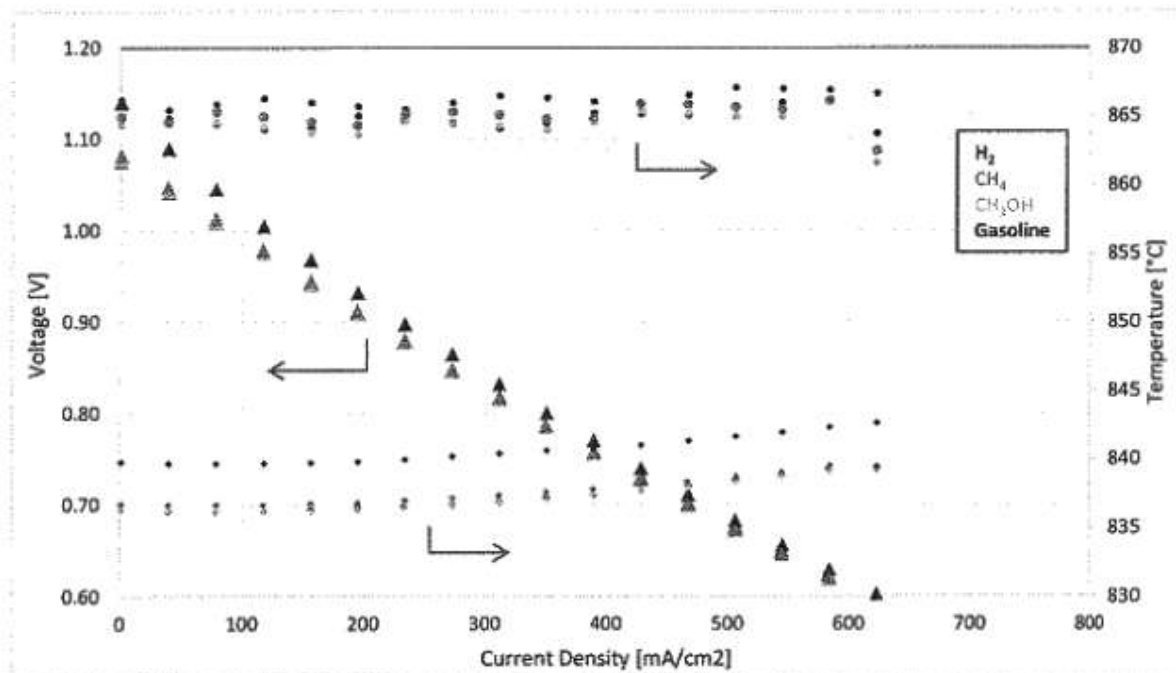
Fig. 6. Polarization curves and anode and cathode temperatures of tested gas compositions.
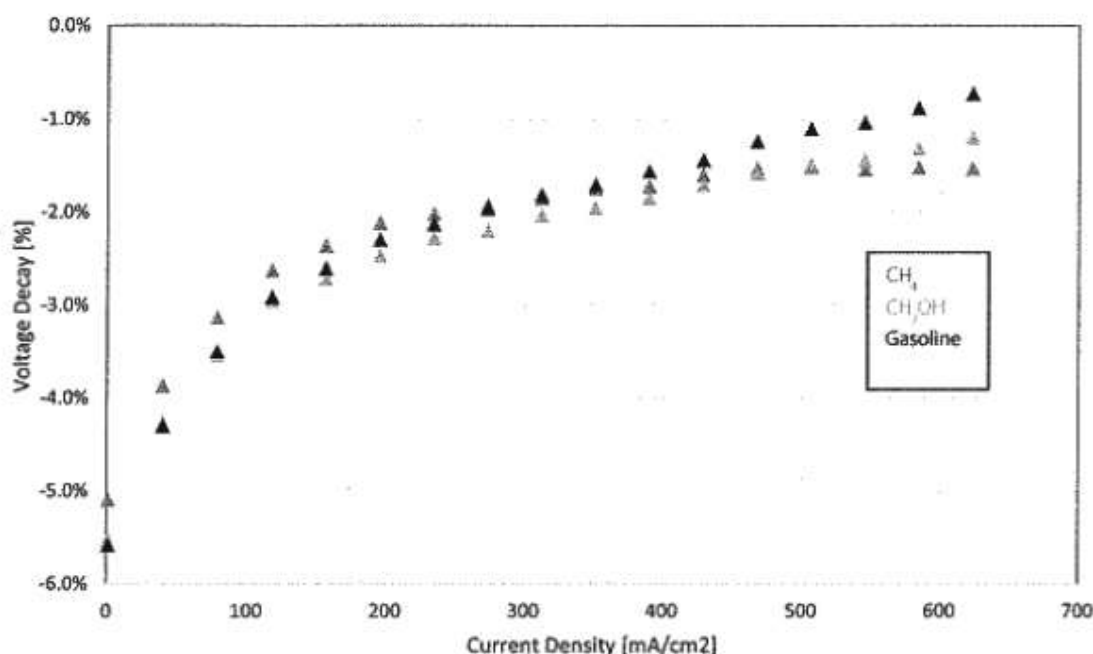
Fig. 7. Voltage decay of each composition tested compared to pure hydrogen.

steam content, the hydrogen concentration and the OCV value will have optimal conditions in terms of energy performance.

5. Conclusion

A major concern when operating SOFCs with hydrocarbons or syngas fuels is the formation of solid carbon through undesired side reactions. The mechanisms for solid carbon deposition are not yet fully known, but they will almost certainly depend on the operating conditions in the cell, e.g., temperatures and most notably the steam content in the fuel stream.

Using a chemical equilibrium model based on Gibbs free energy minimization of the gas mixture, the amounts of reforming reaction products have been calculated for various SOFC fuels. The product compositions have been used to compare the SOFC performance during an experimental test on a single cell. In order to consistently compare the system performance using different fuels for each case study, minimum steam-to-carbon ratios in terms of chemical equilibrium to prevent carbon formation were used. The developed model can be reproduced in any numerical equation solver making it adaptable to different software platforms.

The experimental tests confirm the simulation revealing that the steam reformed product composition shows similar electromotive force (EMF) output for optimal conditions. In fact, at temperatures exceeding 800 °C, the gas composition is dominated by hydrogen and carbon monoxide for any fuel considered. Besides, the cell polarization curves showed similar performance for different fuels if a high degree of fuel pre-reforming is considered.

This leads to conclude that most of the burden in system performance is accounted for by the heat requested for the fuel reforming process. Specifically, heat for steam generation is a major contributor to the heat loss in the energy system. The highest amount of heat required for the steam production was observed in the case gasoline surrogate was used as a fuel. Besides, if reforming conditions

are kept close to minimum steam content, system energy performance will be improved.

Nomenclature

SOFC	Solid oxide fuel cell
s	Entropy
F	Faradays constant, coulomb/mol
G	Gibbs free energy, J/mol
R	Ideal gas constant, J/(mol K)
y	Molar fraction
E	Moles of each chemical element
n_e	Number of electrons transferred in the electrochemical reaction
n	Number of moles
a	Species activity
S/C	Steam-to-carbon ratio
T	Temperature, K
h, H	Enthalpy, J/mol

Greek letters

μ	Chemical potential, J/mol
η	Fuel cell theoretical efficiency
φ	Lagrange function
λ	Lagrange undetermined multiplier

Subscripts

i	Molecule or gas species
j	Chemical element

References

[1] EG&G Technical Services I. Fuel Cell Handbook. U.S. Dept of Energy; 2004.
[2] V. Liso, M.P. Nielsen, S.K. Kær, Ejector design and performance evaluation for recirculation of anode gas in a micro combined heat and power systems based on solid oxide fuel cell, Appl. Therm. Eng. 54 (2013) 26–34.
[3] H. Xu, Z. Dang, B.-F. Bai, Analysis of a 1 kW residential combined heating and power system based on solid oxide fuel cell, Appl. Therm. Eng. 50 (2013) 1101–1110.
[4] R.K. Ahluwalia, X. Wang, Buildup of nitrogen in direct hydrogen polymer-electrolyte fuel cell stacks, J. Power Sources 171 (2007) 63–71.
[5] T. Elmer, M. Worall, S. Wu, S.B. Riffat, Emission and economic performance assessment of a solid oxide fuel cell micro-combined heat and power system in a domestic building, Appl. Therm. Eng. 90 (2015) 1082–1089.
[6] P.A. Pilavachi, S.D. Stephanidis, V.A. Pappas, N.H. Afgan, Multi-criteria evaluation of hydrogen and natural gas fuelled power plant technologies, Appl. Therm. Eng. 29 (2009) 2228–2234.
[7] F. Coutelieris, The importance of the fuel choice on the efficiency of a solid oxide fuel cell system, J. Power Sources 123 (2003) 200–205.
[8] S.L. Douvartzides, F.A. Coutelieris, K. Demina, P.E. Tsiakaras, Fuel options for solid oxide fuel cells: a thermodynamic analysis, AIChE J. 49 (2003) 248–257.
[9] D. Shekhawat, J.J. Spivey, D.A. Berry, Fuel Cells: Technologies for Fuel Processing, Elsevier Science, 2011.
[10] H. Wen, J.C. Ordonez, J.V.C. Vargas, Optimization of single SOFC structural design for maximum power, Appl. Therm. Eng. 50 (2013) 12–25.
[11] V. Liso, M.P. Nielsen, S.K. Kær, Evaluation of different system configurations for solid oxide fuel cell-based micro-CHP generators in residential applications, Eur. Fuel Cell Forum (2009) 1–14.
[12] K. Sasaki, Y. Teraoka, Equilibria in fuel cell gases: I. equilibrium compositions and reforming conditions, J. Electrochem. Soc. 150 (2003) A878.
[13] K. Sasaki, Y. Teraoka, Equilibria in fuel cell gases II. The C-H-O ternary diagram, J. Electrochem. Soc. 150 (2003) A885.
[14] Y. Yang, X. Du, L. Yang, Y. Huang, H. Xian, Investigation of methane steam reforming in planar porous support of solid oxide fuel cell, Appl. Therm. Eng. 29 (2009) 1106–1113.
[15] J. Rostrup-Nielsen, L.J. Christiansen Concepts in syngas manufacture. 2011.
[16] W.B. White, S.M. Johnson, G.B. Dantzig, Chemical equilibrium in complex mixtures, J. Chem. Phys. 28 (1958) 751.
[17] A. Lima da Silva, C.D.F. Malfatti, I.L. Müller, Thermodynamic analysis of ethanol steam reforming using Gibbs energy minimization method: a detailed study of the conditions of carbon deposition, Int. J. Hydrogen Energy 34 (2009) 4321–4330.
[18] M. Cimenti, J.M. Hill, Direct utilization of liquid fuels in SOFC for portable applications: challenges for the selection of alternative anodes, Energies 2 (2009) 377–410.
[19] S. Klein, G. Nellis, Thermodynamics, Cambridge University Press, 2011.
[20] NASA. CEA Chemical Equilibrium with Applications, 2010.
[21] K. Sasaki, K. Watanabe, Y. Teraoka, Direct-alcohol SOFCs: current-voltage characteristics and fuel gas compositions, J. Electrochem. Soc. 151 (2004) A965.

Titolo del progetto:

"Analisi teorica e sperimentale della tecnologia Solid Oxide Cell sia per la generazione di potenza che per la produzione di syngas da fonte rinnovabile"

Relazione II anno di attività

Maggio 2016 – Aprile 2017

Giovanni Cinti Ph.D – RTDa tempo parziale

Attività di Ricerca

L'attività di ricerca ha riguardato lo studio della tecnologia SOFC/SOE per la produzione di potenza e per la produzione via elettrolisi di combustibili gassosi quali idrogeno o miscele ad alto contenuto di idrogeno (syngas).

In questo secondo anno l'attività ha esteso e completato gli studi sul funzionamento della tecnologia quale elettrolizzatore (SOE) integrando anche la valutazione sperimentale di stack per la produzione di potenza a partire da una miscela syngas prodotta da dry reforming. Il dry reforming permette di aumentare l'efficienza dei sistemi SOFC alimentati da gas di rete e eliminare la necessità di alimentare il banco con acqua di linea come nei sistemi steam refomring. Di contro questa tecnologia presenta problemi di inquinamento dovuto ai depositi di carbone sia nel reattore di reforming che nelle celle ad ossidi solidi. Lo studio si è concentrato soprattutto in questo secondo aspetto. L'attività ha riguardato sia lo studio bibliografico sul progetto del sistema e della tecnologia dry reforming, che l'attività sperimentale realizzata in laboratorio. Nel dettaglio le specifiche attività sono state:

- Studio bibliografico dei temi di ricerca riguardanti SOFC e SOE;
- Progettazione campagna prove finalizzata all'analisi delle performance della cella e allo studio dell'effetto della composizione;
- Realizzazione dei test;
- Analisi dati e studio dei risultati;
- Pubblicazione dei risultati in conferenze e giornali scientifici;
- Supporto alla rendicontazione dei progetti PON "FUEL CELL LAB" e "SMART GENERATION";
- Raccordo e coordinamento tra le attività del Dipartimento dell'Università degli Studi di Perugia e gli altri partner dei progetti PON;
- Partecipazione alla stesura e presentazione di progetti sottoposti a finanziamento a valere sotto il programma europeo HORIZON 2020 (NEPHTHYS, BIO-SPRING);
- Attività tecnica/sperimentale di laboratorio: utilizzo e progettazione di strumenti e tecniche per lo studio di sistemi celle a combustibile/elettrolizzatori ad alta temperatura;
- Supporto all'acquisto di strumenti e materiale di consumo necessari all'attività di ricerca;
- Partecipazione alle attività dell'associazione N.ERGHY di cui il Dipartimento è membro, associazione che gestisce in partenariato con la Commissione e il raggruppamento degli industriali i fondi Comunitari destinati ad Idrogeno e celle a combustibile;
- Attivazione e gestione di due progetti europei a valere sul fondo HORIZON2020: NET TOOLS e ELECTROU dei quali sono responsabile scientifico per l'Università degli Studi di Perugia;
- Attivazione e gestione del progetto H2 in ICE finanziato dalla Fondazione Cassa di Risparmio di Perugia del quale sono responsabile scientifico;
- Gestione del progetto H2 in ICE finanziato dalla cassa di risparmio di Perugia finalizzato allo studio di elettrolizzatori onboard. L'attività ha riguardato lo studio bibliografico sia del componente che degli effetti che H2 e HHO hanno su motori a combustione interna. In aggiunta sono stati realizzati dei test sperimentali sulla tecnologia tradizionale per l'elettrolisi a bordo e lo studio del sistema per capire i vantaggi ottenibili con una nuova tecnologia.

Pubblicazioni

Specificatamente alle attività di ricerca relative al progetto del contratto sono state pubblicati i seguenti lavori interamente riportati in allegato:

1. L. Barelli, G. Bidini, G. Cinti, F. Gallorini, M. Pöniz, *"SOFC stack coupled with dry reforming"*, Applied Energy, , Volume 192, 15 April 2017, Pages 498-507, ISSN 0306-2619, https://doi.org/10.1016/j.apenergy.2016.08.167.

2. L. Barelli, G. Bidini, G. Cinti, A. Ottaviano, *"SOFC regulation at constant temperature: Experimental test and data regression study"*, Energy Conversion and Management, Volume 117, 1 June 2016, Pages 289-296 ; doi:10.1016/j.enconman.2016.03.028

3. G. Cinti, D. Frattini, G. Bidini, U. Desideri, E. Jannelli *"Coupling Solid Oxide Electrolyser (SOE) and ammonia production plant"* Applied Energy, Volume 192, 15 April 2017, Pages 466-476, ISSN 0306-2619, https://doi.org/10.1016/j.apenergy.2016.09.026.

4. G. Cinti, G. Bidini, K. Hemmes *"An experimental investigation of fuel assisted electrolysis as a function of fuel and reactant utilization"*. Int J Hydrogen Energy Volume 41, Issue 28, 27 July 2016, Pages 11857-11867, ISSN 0360-3199; doi: 10.1016/j.ijhydene.2016.05.205.

In aggiunta grazie ad ulteriori collaborazioni sviluppate in questi anni e ad attività di ricerca svolte precedentemente sono stati pubblicati i seguenti lavori, anch'essi riportati in allegato:

5. A. Baldinelli, G. Cinti, U. Desideri, F. Fantozzi *"Biomass Integrated Gasifier-Fuel Cells: experimental investigation on wood-syngas tars impact on NiYSZ-anode Solid Oxide Fuel Cells"*, Energy Conversion and Management, Volume 128, 15 November 2016, Pages 361-370, doi: 10.1016/j.enconman.2016.09.048.

6. F. Fantozzi, A. Frassoldati, P. Bartocci, G. Cinti, F. Quagliarini, G. Bidini, E.M. Ranzi, *"An experimental and kinetic modeling study of glycerol pyrolysis"*, Applied Energy, Volume 184, 15 December 2016, Pages 68-76, ISSN 0306-2619, http://dx.doi.org/10.1016/j.apenergy.2016.10.018.

7. D. Frattini, G. Cinti, G. Bidini, U. Desideri, R. Cioffi, E. Jannelli *"A system approach in energy evaluation of different renewable energies sources integration in ammonia production plants"*. Renew Energy 2016;99:472–82; doi: 10.1016/j.renene.2016.07.040.

8. G. Cinti, G. Discepoli, E. Sisani, U. Desideri *"SOFC operating with ammonia: Stack test and system analysis"*. Int J Hydrogen Energy 2016; 41:13583–90; doi:10.1016/j.ijhydene.2016.06.070.

In stesura o in attesa di pubblicazione:

1. L. Barelli, G. Bidini, G. Cinti, A. Ottaviano, "Study of SOFC-SOE transition on a solid oxide stack";

2. L. Barelli, G. Bidini, G. Cinti, "Steam Vs dry reformer in a SOFC short stack: experimental study";

3. G. Cinti, A. Anca-Couce, P. Bartocci, G. Bidini, F. Fantozzi " Use Of Waste Glycerol Pyrolysis Products In Fuel Cells";

I risultati dell'attività di ricerca sono stati presentati in conferenze e meeting internazionali:

1. L. Barelli, G. Bidini, G. Cinti, "Effect of gas composition and operative temperature into SOFC/SOE transition" World Hydrogen Energy Conference 2016, Saragoza, June 13th-16th;

2. A. Anca-Couce, G. Cinti, P. Bartocci, G. Bidini, F. Fantozzi, *"Use Of Waste Glycerol Pyrolysis Products In Fuel Cells"*, Proceedings SUM2016, Third Symposium on Urban Mining and Circular Economy, 23 - 25 May 2016, Old Monastery of St. Augustine, Bergamo, Italy, © 2016 by CISA Publisher, Italy;

Attività didattica integrativa

Sullo stesso tema delle attività di ricerca è stata realizzata l'attività di formazione ed affiancamento – didattica integrativa - agli studenti iscritti al progetto di formazione del PON "SMART GENERATION". In particolare:

- Supporto alle attività di formazione riguardanti lo sviluppo e l'utilizzo di sistemi di controllo per banchi prova di celle a combustibile;
- Formazione teorica sull'idrogeno e celle a combustibile, sulle problematiche dell'integrazione e sui componenti necessari al funzionamento corretto del sistema;

CrossMark
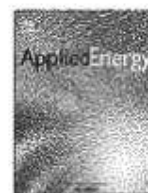
SOFC stack coupled with dry reforming

L. Barelli[a], G. Bidini[a], G. Cinti[a,*], F. Gallorini[b], M. Pöniz[c]

[a] Department of Engineering, University of Perugia, Via G. Duranti 1/A4, Perugia 06125, Italy
[b] Department of Engineering, University of Napoli "Parthenope", Centro Direzionale Isola C4, Napoli 80143, Italy
[c] EBZ GmbH, Germany

HIGHLIGHTS

- Integration of dry reforming and SOFC was studied.
- Dry reforming operation was analyzed by mean of experimental activity.
- Dry reforming compositions were used as anodic gas into a SOFC stack.
- High concentrated compositions do not cause increase of temperature.
- Higher power was obtained when higher concentrated fuel mixtures were used.

ARTICLE INFO

ABSTRACT

The study proposes an innovative CHP system based on the coupling of carbon dioxide dry reforming (CDR) and solid oxide fuel cell (SOFC) technology. To supply CO_2 at the CDR unit, increasing at the same time the overall utilization factor, SOFC anode off-gases are recycled for fuel reforming. In the CDR unit, in fact, the CO_2 in the anodic exhausts reacts with feeding low carbon fuels (in this case natural gas) producing hydrogen and carbon monoxide for the SOFC feeding, thus allowing an internal CO_2 reuse. In particular, the SOFC, characterized by high operating temperatures and significant recoverable heat, guarantees suitable temperature of the CDR process, highly endothermic. Moreover, compared to traditional CDR applications, lower temperatures are acceptable because SOFC tolerates feeding gas containing limited amounts of CO and CH_4. According to this concept, the SOFC stack can be conveniently fed by a dry reformer reactor. The present study addresses the experimental characterization of SOFC short-stacks performance, in terms of produced power and thermal behavior, when fed by different fuel mixtures produced through dry reforming.

© 2016 Elsevier Ltd. All rights reserved.

1. Introduction

Carbon dioxide is the major greenhouse gas that contributes to the global warming. In order to mitigate GHG environmental impact, technological strategies aiming to avoid or reuse CO_2 emissions become crucial. In this context, an increasing widespread of fuel cell systems, specifically under innovative configurations with improved efficiency, is expected in the next years. The scenario, in terms of the expected trend of the European fuel cell market revenue, is estimated in fact to reach 448mil€ by 2018. The unit shipments of fuel cells are expected to increase globally from 3776 units in 2012 to 338,727 units by 2018. Moreover, specifically for the stationary power generation, fuel cell applications are expected rising as they are very efficient sources of off grid power [1]: a long

term market valued for thousands of units annually is envisioned for the intermediate power range [2].

In [3], an innovative CHP system based on the coupling of carbon dioxide dry reforming (CDR) and solid oxide fuel cell (SOFC) technology is proposed, in the intermediate power range (from tens up to hundreds of kW) for distributed combined heat and power generation. With respect to SOFC coupled with conventional steam methane reforming, this system is characterized by enhanced electric and overall (in CHP applications) efficiency, with a CO_2 emission factor significantly reduced. According to this concept, the SOFC stack can be conveniently fed by a dry reformer reactor. Anode off-gases, containing CO_2, feed the dry reformer, where CO_2 reacts with the fuel (e.g. natural gas) producing hydrogen and carbon monoxide. An internal CO_2 reuse is then realized using the reformate gas as fuel in the SOFC. The heat required by the dry reforming process can be guaranteed by a suitable thermal integration of the SOFC stack and the reformer unit. The dry

* Corresponding author.
E-mail address: giovanni.cinti@unipg.it (G. Cinti).

operation mode makes the system frozen-resistant; moreover no external water is needed. This autarkic operation represents a key factor, which can be well coupled to applications in the mid-sized power range, typically implemented for decentralized production (also in CHP configuration) and smart grids applications.

Preliminary modelling results [3] evidenced that the innovative proposed system layout exhibits, in the case of natural gas feeding, an electric efficiency over 65%, with a related CO_2 emission factor significantly lower than the one characteristic of the best conventional fuel cell-based CHP system (reduction of about 10% with respect to steam methane reforming based systems with anode recirculation), as also discussed in [4]. Also higher global efficiencies are expected in CHP applications.

Dry reforming is studied in literature mainly related to direct-biogas SOFCs [5–10], therefore considering internal reforming processes. In such studies the direct use of CH_4-CO_2 mixtures is presented enhancing internal dry reforming, taking advantage of the catalyst material in the cell anode. In the case of internal reforming, both chemical and electrochemical equilibriums are involved at the same time and they influence each other, with critical issues for what concerns thermal stresses when dry reforming represents the main CH_4 reaction path [11,12]. In the study here proposed, instead, dry reforming and electrochemical reactions are separated, the first occurs in the reforming reactor and the second in the SOFC stack. This layout permits the optimization of both components and requires a deep study of operative conditions of the units and their thermal integration.

Therefore, to support the SOFC-CDR integrated system architecture, a deep investigation is needed at both stack and reformer level, to determine components behavior and performance under these specific operative conditions. The present work, in particular, addresses the investigation of SOFC behavior when fed by concentrated fuel mixtures as the ones obtainable through dry reforming process.

Compared with the case here investigated, SOFCs are usually operated, as discussed in literature for what mainly concerns performance characterization, with highly diluted mixtures. Systems fuelled with natural gas, in fact, operate with syngas from steam methane reforming (SMR) or partial oxidation (Pox) [13]. Both these technologies produce a gas mix with high content of inert, steam in the case of SMR and nitrogen in Pox. If biogas is used instead of methane, the syngas is even more diluted due to the presence of CO_2 in the initial fuel.

Highly concentrated syngas are studied when coupling SOFC with gasification systems. Indeed, some types of gasifier, such as steam or oxygen gasifiers, produce a mixture where the sum of active species (CO, H_2 and CH_4) can achieve high concentrations (>80 vol.%) and a LHV of 20 MJ/Nm^3 [14,15]. Literature reports studies of using these mixtures, as SOFC fuel, mainly focused on experimental test on single cells with the aim of evaluating cell performance and carbon deposition issues [16–24]. Ref. [25], as example, concerns a SOFC based system fed by a biogenous gas mixture as fuel, equipped with an external reformer. Experimental data of the reformer operation according also to the dry reforming path reaction are provided, but tests on the short-stacks are provided only in the cases of feeding with a steam-reformed mixture and hydrogen. The effect of high concentrated syngas in a SOFC stack or short-stack is poorly treated in literature. Moreover the available studies [20,26] concern the SOFC performance characterization, in terms of polarization curve and produced power, while the thermal issue related to the poor dilution of the anodic feeding mixture is not addressed.

The present work, concerns the investigation of SOFC short-stack operation, in case of feeding with concentrated fuel mixtures obtained through external dry reforming process, considering both electrochemical performance and thermal issue. Literature does not report any experimental results on the operation of a SOFC stack with dry reformed methane. With the aim of supporting the SOFC-CDR concept already proposed, this study allows, for the first time, the performance assessment of single components (i.e. SOFC stack, CDR unit) operated as resulting from their coupling. Specifically, an experimental investigation is performed through a parameter variation study of the two main subsystems: the CDR reactor and the SOFC stack. Fuel feeding compositions were determined by simulation of the SOFC-CDR integrated system, at specific working points, and through experimentation to enlarge the CDR unit operative conditions (in terms of reactor temperature and CH_4/CO_2 inlet ratio) and, therefore, the variation range of chemical species in the reformate gas. Therefore, also a preliminary experimental activity on dry reforming process was performed.

First results on a SOFC short-stack highlight a limited increase in stack temperature (assuring safety operative conditions for what concerns the risk of thermal stresses) and produced power increasing with the fuel mixture concentration, supporting the particular SOFC-CDR integration described above.

2. Theoretical background: SOFC – CDR integrated system

The SOFC-CDR system architecture is constituted by two main sections. The upper one is composed by a main SOFC stack and a dry reformer unit that feeds the fuel cell.

Since the syngas flow rate produced by the CDR block is greater than the one required by the main-SOFC, a supplementary SOFC stack was added as bottomer system. The power of this stack is fixed in order to exploit the syngas not consumed by the main-SOFC. System feeding streams are two, respectively: the inlet air flow rate and the fuel (natural gas) feeding flow rate. A simplified scheme of the concept is reported in Fig. 1, while for the detailed system layout modelled in the Aspen Plus environment we refer to [3].

As it can be seen, the system layout shows a direct integration of main-SOFC and CDR unit. Specifically, after water condensation, ANODE exhaust gases, delivered by the main-SOFC, move to the CDR input together with a methane stream. This fresh methane is mixed with anode off-gas by an ejector in order to guarantee the pressure recovery. With respect to the intended application (intermediate power range), the source of methane supply will likely be pressure grid of natural gas at higher level with respect to domestic grid with only several mbar of pressure. The syngas produced by the CDR unit is sent again, in the required amount, to the main-SOFC anode, while the remain part is used to fed the bottomer-SOFC anode. From simulations performed in [3] a total power of 170 kW arises subdivided as 95 kW and 75 kW produced respectively by the main-SOFC and the bottomer-SOFC. The anodic exhaust of the bottomer-SOFC, still containing unreacted species (e.g. H_2 and CO), is sent to a burner reactor. The produced heat is used to preheat the inlet air.

From a thermal point of view, the main-SOFC exhaust gases provide the heat required by CDR reactor (thus operated also at reduced temperature with respect to conventional CDR applications). Moreover, maintaining a low CDR temperature in order to reduce the thermal need, the produced syngas contains CO that, well tolerated (within certain limits) by SOFC, is used as a fuel without efficiency penalties at the overall system level. To achieve a suitable cathode inlet air temperature, the feeding air passes through a series of compact heat exchangers in which the exhaust gases are exploited to preheat the inlet air stream. The overall architecture is reported in Fig. 1.

Thermodynamic calculations show that the technology under development can reach over 65% of electrical efficiency offering a significant reduction in CO_2 emissions. Such performance was
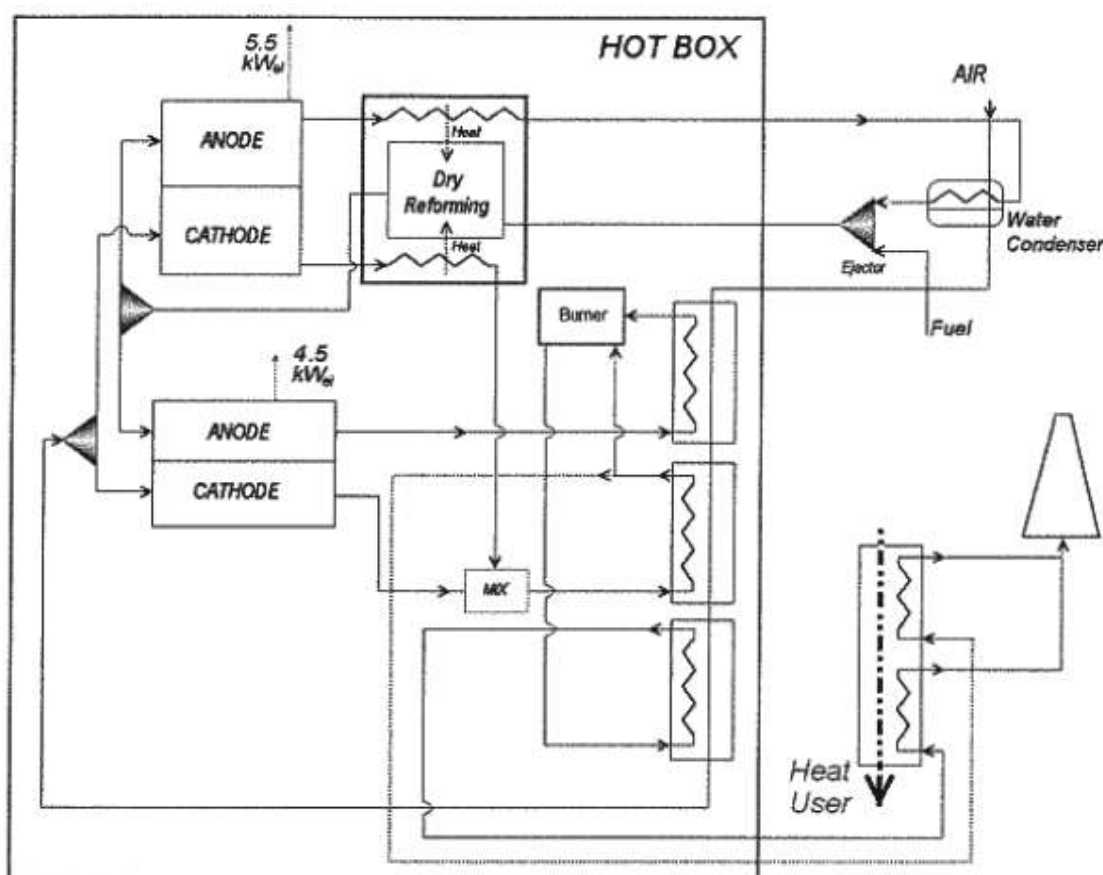
Fig. 1. Overall architecture of proposed system.

calculated when modelling the system with a stack temperature of 850 °C, CDR operating at 655 °C and an equivalent molar flow of CH_4 and CO_2 at reactor inlet. In addition, no external water is needed, further contributing to the reduction in primary sources exploitation. An increased system lifetime is foreseen by drying of recycled anode off-gas, minimizing the risk of condensation effects also during system start-up and shutdown procedures.

3. Preliminary testing activity on dry reforming process

The experimental investigation on the dry reforming process was performed within a wider research activity concerning the production of concentrated reformed mixtures as in the case of sorption-enhanced steam reforming [27–30]. Aiming to validate the feasibility of the coupling of CDR and SOFC technologies, preliminary dry reforming tests were performed on a test rig equipped with a fixed-bed tubular reactor (see Fig. 2). Such a reactor in Hastelloy X allows possible simultaneous high operating pressure and temperature (up to 10 bar and 900 °C). The catalyst bed is placed in the isothermal zone between two pieces of glass wool. Three thermocouples are placed inside the reactor, through the outlet, in contact with the catalyst bed. The reactor is housed inside a 3-zones furnace that ensures an isothermal profile in throughout the reactor length. Gas lines are fed from cylinders provided with pressure reducing valves that guarantee a 3–10 bar line pressure. After passing through a line shut-off valve, the reactant gases are fed into the reactor by means of dedicated mass flow controllers; check-valves are installed to prevent products flowing back. A temperature controlled gas preheater and a liquid evaporator prevent

condensation inside the reactor. At both reactor inlet and outlet, the flow passes through 15 μm sintered filters made of 316 stainless steel for particle capture. At the reactor outlet, reaction products pass through a liquid/gas separator fitted with a high-resolution capacitive level sensor. This system allows the condensation of liquids at low temperature; liquid draining is performed automatically. Gases leave the separator through the upper part towards the pressure control system. It consists of a servo positioned micrometric regulating valve providing a continuous and constant flow of gases at the outlet. After the pressure control system, exhaust gas passes through a flow meter for flow rate determination and then it is analyzed by two micro-Gas Chromatography columns for detection of H_2, N_2, CH_4, CO_2 and H_2, O_2, N_2, CO. CH_4 respectively. A sample every 2 min is analyzed and recorded. The whole bench is controlled remotely by a dedicated software that allows the programming of each test phase by varying one or more operating parameters.

The catalyst tested in this preliminary phase is Ni 15%-Co 5%-$MgO-Al_2O_3$. This material was synthesized within a further research activity, performed by University of Perugia, concerning the development of innovative catalysts for the Dry Reforming process. The particular catalyst composition was identified and tested to prevent carbon deposition, considering lower operating temperatures (700–750 °C) with respect to the typical ones of hydrogen production through Dry Reforming (also up to 900–1000 °C [31,32]). Lower temperatures are here investigated in relation to the CDR unit thermal integration with the SOFC stack [3].

The weight and volume of catalyst bed is 40 g and 150 ml and it was activated under hydrogen atmosphere at 500 °C. After activation, the feeding composition was switched to simulate an
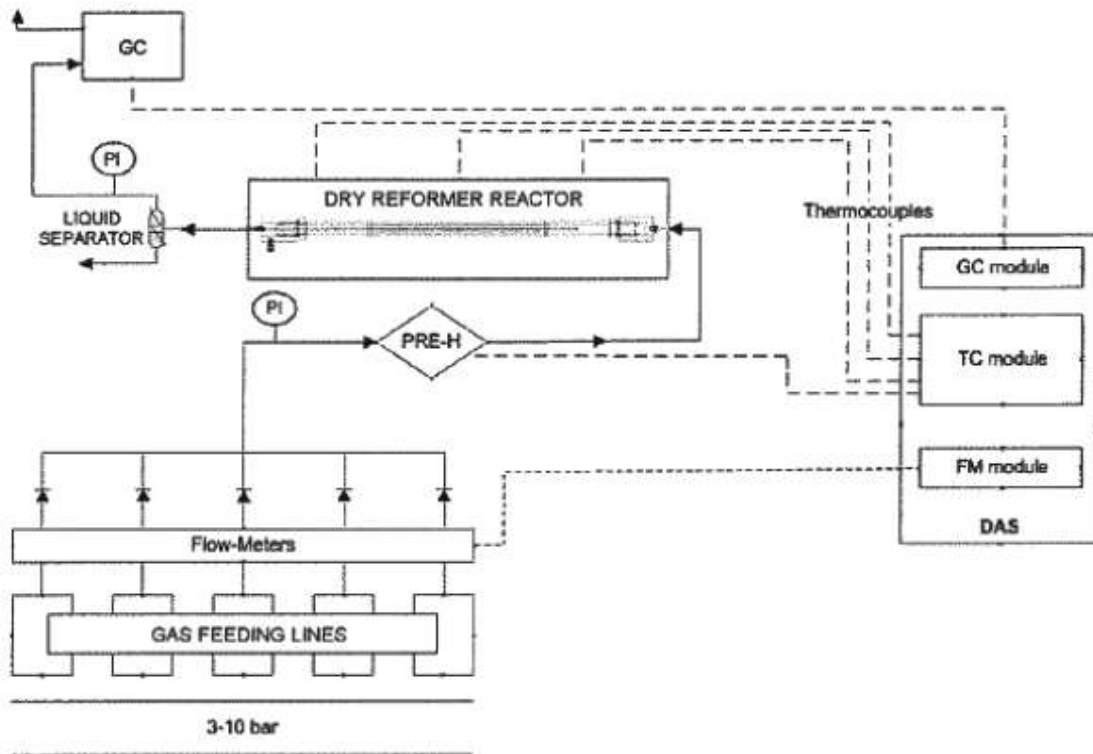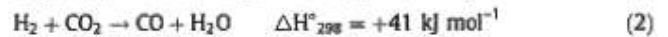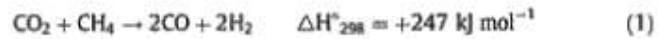
Fig. 2. CDR test rig schematic.

equimolar CH_4-CO_2 mixture. Different operating conditions, as described in the following, were tested for about 20 min (once stable composition of outflow gases was reached) in order to collect 10 measurements by the GC section. Average values of gas contents were used to evaluate performance of the process.

Initially, tests were executed at different temperatures (620 °C, 700 °C, 750 °C and 810 °C to have sufficient operative points to characterize the reactor behavior at temperature variation) with total flow rate equal to 800 ml/min. Fig. 3 shows trends of CO, H_2, CO_2 and CH_4 content (vol.% on dry basis) at reactor outlet varying the temperature.

Increasing the temperature, CH_4 and CO_2 contents decrease, while H_2 and CO ones grow accordingly to the endothermic

reaction expressed by Eq. (1). Reverse water gas shift reaction (Eq. (2)), that consumes the produced hydrogen, is also favored by high temperature and thus CO content increases more rapidly with respect to the H_2 one.

$$CO_2 + CH_4 \rightarrow 2CO + 2H_2 \qquad \Delta H°_{298} = +247 \text{ kJ mol}^{-1} \qquad (1)$$

$$H_2 + CO_2 \rightarrow CO + H_2O \qquad \Delta H°_{298} = +41 \text{ kJ mol}^{-1} \qquad (2)$$

For experimental activity on SOFC short stack, 700 °C and 750 °C were considered in the following among the investigated temperatures. These values, in fact, are compatible with the thermal integration of the SOFC stack and the CDR unit, considering the SOFC operating temperatures chosen for the experimentation
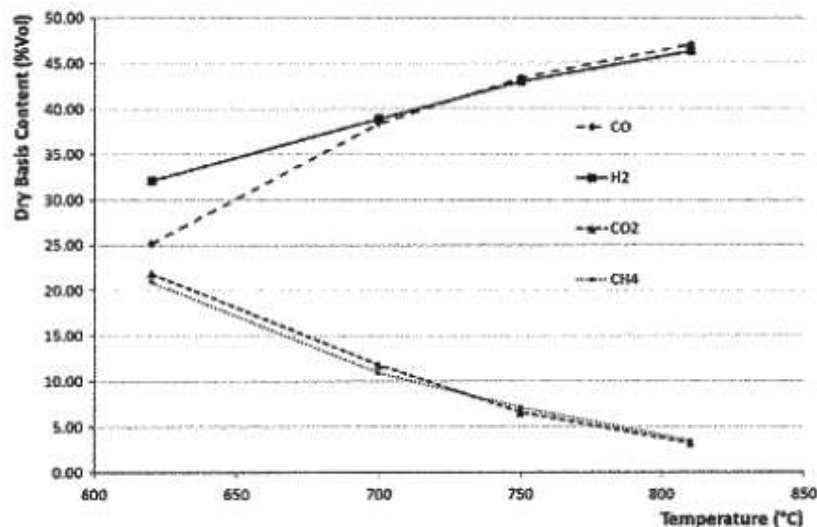
Fig. 3. CO, H_2, CO_2 and CH_4 contents vs operating temperatures.

(see Section 4.3). Moreover, at 620 °C the occurrence of carbon deposition phenomenon was experimentally revealed. Indeed, catalyst surface coking occurs above to 557 °C via methane dehydrogenation (Eq. (3)), meanwhile below to 700 °C the Boudouard reaction (Eq. (4)) takes place. Thus, carbon deposition is produced to a greater extent at temperatures lower than 700 °C.

$$CH_4 \rightarrow C(s) + 2H_2 \qquad \Delta H°_{298} = +75 \text{ kJ mol}^{-1} \qquad (3)$$

$$2CO \rightarrow C(s) + CO_2 \qquad \Delta H°_{298} = -171 \text{ kJ mol}^{-1} \qquad (4)$$
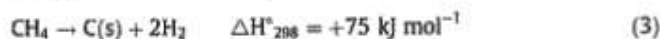
For this reason, considering also the lower methane conversion obtained at 620 °C (see Fig. 3), the reformate composition obtained with this reactor temperature was not included in the test campaign on the SOFC short stack (see Section 4.2).

Furthermore, for the dry reforming experiments performed at 700 °C and 750 °C, the total flow rate of the feeding mixture was varied (200, 400, 600 and 800 ml/min) in order to maximize the methane conversion. As expected, higher H_2 and CO contents (see Fig. 4) were obtained for the lowest flow rate (200 ml/min) due to the higher residence time of the feeding mixture. In fact, the gas hourly space velocity (GHSV) changes from 320 l/h at 800 ml/min to 80 l/h at 200 ml/min. Fig. 4 reports experimental results together with simulation outcomes obtained in the Aspen Plus environment (the CDR unit was modelled with a Rgibbs reactor) at chemical equilibrium and under similar operating conditions. As evident in Fig. 4, at the lowest flow rate (200 ml/min), H_2 and CO contents have a good match with simulation results.

Therefore, syngas composition experimentally obtained on Ni 15%-Co 5%-MgO-Al$_2$O$_3$ catalyst, under 200 ml/min of feeding equimolar CH_4-CO_2 mixture at 700 and 750 °C, were considered in the next tests on SOFC short stack (B1 and B2 compositions of Table 2, Section 4.2).

4. SOFC experimental characterization

4.1. Materials

The experimental activity was performed on a 4 cells short stack based on anode-supported planar cells, each with an active area of 80 cm^2. Stack details and materials are reported in Table 1. The stack is hosted in a test rig that permits its operation and the
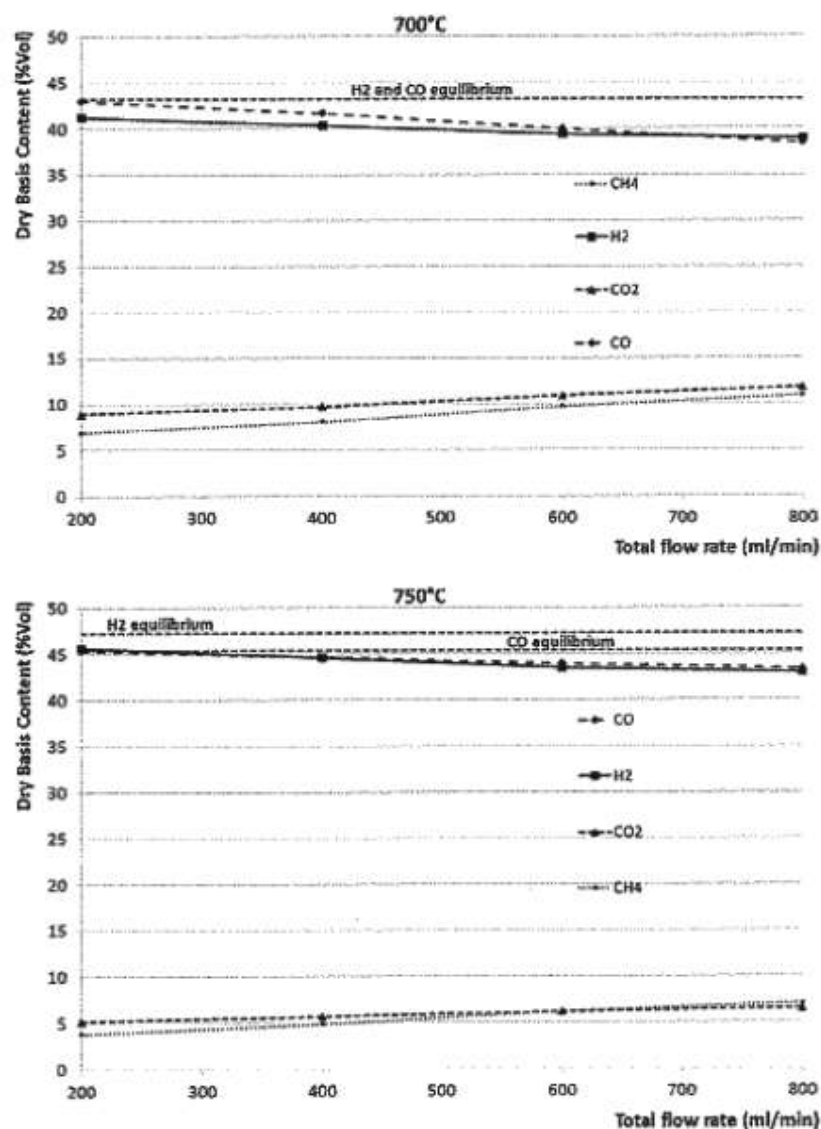
Fig. 4. CO, H_2, CO_2 and CH_4 contents vs flow rate (ml/min).

Table 1
Short stack details.

Anode substrate	Ni/8YSZ cermet 1500 µm
Anode substrate	Ni/8YSZ cermet 1500 µm
Anode functional layer	Ni/8YSZ cermet 7–10 µm
Electrolyte	8YSZ 8–10 µm
Cathode functional layer	LSM/8YSZ 10–15 µm
Cathode current collector	LSM 60–70 µm
Stack design	F-design [33]
Interconnect/cell frame	Crofer22APU
Anode contact layer	Ni-mesh
Cathode contact layer	Perovskite type oxide (LCC10)
Sealing	Glass-ceramic (87YSZ20)
Number of cells	4
Size of cells	100×100 mm^2
Active area per cell	80 cm^2
Total active area	320 cm^2

control of main parameters such as voltage, current, temperature and gas flows. In details, gas flow system is composed by air gas flow meters at the cathode and pure gases (H_2, CO, CO_2, CH_4, N_2) at the anode, while a controlled evaporator mixer allows to flow steam into the anode. Temperature is controlled by two thermoregulators that permit the setting of furnace temperature, where the stack is physically located, and of inlet gas flows (both anodic and cathodic). Electrical circuit is realized with a power supply, in series with an electrical load and the stack, so that both constant current (CC) and constant voltage (CV) stack configurations are possible. During the test, CC operation is kept while measuring voltage with a data acquisition system. Also stack temperature is monitored through two thermocouples located in the stack body, close to anode (T1) and cathode (T2) inlet respectively. Note that internal stack gas flow is a counter current design so that one electrode gas side is close to the outlet of the other electrode. All physical parameters are sampled by a control system with frequency on 1 Hz. A picture of the test rig is reported in Fig. 5.

4.2. Test campaign

The testing activity was planned to evaluate stack performance when dry reforming compositions are used. Specifically the aim was the determination, for each investigated operating condition, of the obtainable power density and the thermal behavior of the short stack.

Considering the outcomes of both our previous modelling at stack and system level and experimental activity on dry reforming, 5 fuel mixtures were selected for the anode feeding. In this way, a sufficiently wide range of reformate gases was obtained, as reported in Table 2. Test compositions are divided into two groups: A and B.

Compositions A come from specific simulations performed by means of the SOFC-CDR integrated model, according to the specific layout architecture defined in [3], mainly varying the optimization of the thermal regeneration section, SOFC operating temperature and therefore the temperature of the CDR unit. Compositions B, instead, were determined from experimental activities on dry reforming, as detailed in Section 3.

In details, relative to the dry reformer operating temperature, A1 refers to 809 °C, A2 to 840 °C and A3 to 960 °C, while a constant CH_4/CO_2 ratio (equal to 0.6 to maximize, according to simulation results, the overall efficiency of the SOFC-CDR integrated system) was maintained at the reactor inlet. Regarding compositions B, B1 and B2 were obtained from experimental tests on dry reforming reactor with reactor temperature of 700 °C and 750 °C respectively. Moreover, both compositions B refer to a reduced feeding flow rate (set to assure a sufficient contact time to maximize methane conversion) and an equimolar CH_4-CO_2 mixture (CH_4/CO_2 = 1) at the

Fig. 5. SOFC test rig.

dry reforming reactor inlet, so for reactor temperature and feeding conditions not included in the simulation campaign.

Table 2 reports also the inert ($H_2O + CO_2$) concentration and the O/C ratio. Compositions A are more diluted than the B ones, while O/C values are in the same range with smaller values for the B compositions.

Fig. 6 reports the ternary diagram (CHO) of the compositions. By means of such a diagram it is possible to predict the main risk related to the fuel composition in terms of carbon deposition or nickel re-oxidation. As expected, the compositions are on the border of the carbon deposition area. Such a risk is overestimated because is based on inlet gas composition while, during operation, steam is produced pushing the gas mix compositions in a more safety area. Moreover, as experimentally demonstrated and deeply discussed in [34], Gibbs equilibrium diagrams can be used to identify the coking risk, providing reliable information only in reference to open circuit voltage condition. Under current swap, instead, the oxygen migration through the electrolyte causes different equilibrium conditions moving towards the no-coking region. Anyway the carbon deposition risk should be investigated in the future through a dedicated activity.

Based on these compositions gas flows were calculated introducing the equivalent hydrogen flow rate, $\dot{H}_{2eq}$, as defined by Eq. (5).

$$\dot{H}_{2eq} = \dot{H}_2 + \dot{CO} + 4\dot{CH}_4 \tag{5}$$

where $\dot{H}_2$, $\dot{CO}$ and $\dot{CH}_4$ are hydrogen, carbon monoxide and methane molar flow rates respectively. The introduction of $\dot{H}_{2eq}$ parameter aims to quantify the active species in the flow-mix weighted for the electron flow that can be produced in the electrochemical reaction. $\dot{H}_{2eq}$ was fixed for all tests at 80 Nl/h equal to 4.16 ml/min cm^2. The test campaign was designed based on constant fuel utilization, expressed by means of fuel utilization factor (U_f). For each gas composition, in fact, three U_f values were defined (0.7, 0.6, 0.5) identifying three single operating conditions for the stack. U_{ox} was kept

Table 2
Gas composition (mol.) used during test activity.

	A1	A2	A3	B1	B2
H_2	25%	26%	31%	40.0%	43.8%
CH_4	11%	11%	6%	5.3%	2.3%
H_2O	6%	6%	6%	4.2%	3.5%
CO	37%	38%	43%	43.1%	45.6%
CO_2	21%	19%	14%	7.4%	4.8%
O/C	1.23	1.21	1.22	1.11	1.11
Inert	27%	25%	20%	11.6%	8.3%
Reactor temperature	809 °C	840 °C	960 °C	700 °C	750 °C
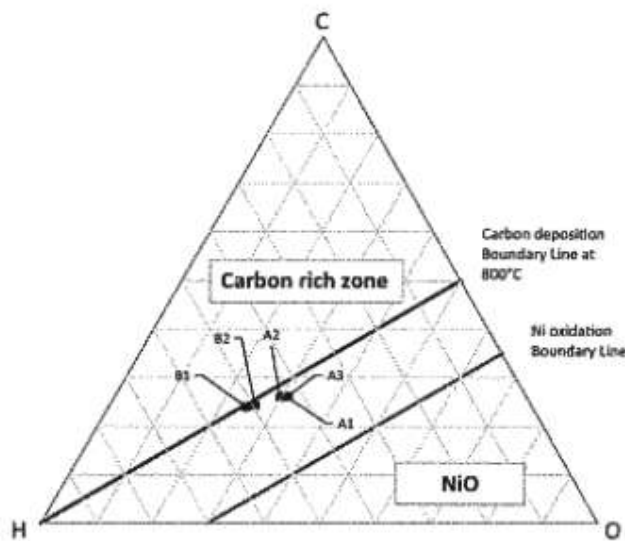
Fig. 6. Ternary diagram of dry reforming compositions.

constant at 0.2 for all the tests. A total of 15 conditions were therefore calculated as reported in Table 3.

Each condition is kept for one hour to permit thermal stabilization of the stack. Characteristic parameters (e.g. voltage, operative temperatures) for each operation point were calculated as mean values during a period of 5 min at the end of the hour. Aiming to analyze the thermal issue (in terms of reached temperatures in the anodic and cathodic sides respectively) under the several operating conditions here investigated, furnace temperature was kept below the stack one, taking advantage of heat development during stack operation. To achieve a proper setting of the furnace temperature, preliminary tests were executed with feeding conditions typical of steam reforming fuel pre-processing. Specifically, furnace temperature was reduced until difference between stack and furnace grew over the limit of 10 K. This condition was obtained for furnace temperature close to 740 °C that is also the typical operating temperature of SOFC technology.

4.3. Results

All compositions were tested as defined in the test campaign. Stabilization was achieved after one hour both for voltage and temperature. As example Fig. 7 reports the variation of total stack voltage and temperatures during the three tested U_f conditions with A2 composition. Voltage trend shows, in all cases, a stable value with no constant decrease during the stabilization period. Such behavior indicates that there is no degradation due to coking, coherently with prediction and observations made on the basis of the ternary diagram COH (see Section 4.2). As known, indeed, carbon deposition strongly affects the cell stability with fast degradation in performance, making cell stability even more important than the power output in carbon deposition detection [35]. Anyway, to exclude a degradation due to carbon deposition under the feeding conditions here investigated, long-term tests will be performed in the future to asses any material modification (a proper post-analysis will be included) related to operation.

Fig. 8 reports stack power as function of U_f for all tested compositions. Higher powers where obtained for B compositions for all U_f values. Such difference comes mainly from the fuel concentration that permits an increase in OCV values and, consequently, in all the voltages.

Table 3
Details of the test campaign.

|	T SOFC °C	Nl/h H_{2eq}	U_f	U_{ox}	% H_2	% CO	% CO_2	% CH_4	% H_2O	Nl/h H_2	Nl/h CO	Nl/h CO_2	Nl/h CH_4	g/h H_2O	Nl/h Air	A I	mA/cm² J
A1	740	80	0.7	0.2	25	37	21	11	6	18.87	27.92	15.85	8.30	3.64	666.67	33.48	418.51
	740	80	0.6	0.2	25	37	21	11	6	18.87	27.92	15.85	8.30	3.64	571.43	28.70	358.72
	740	80	0.5	0.2	25	37	21	11	6	18.87	27.92	15.85	8.30	3.64	476.19	23.91	298.94
A2	740	80	0.7	0.2	26	38	19	11	6	19.26	28.15	14.07	8.15	3.57	666.67	33.48	418.51
	740	80	0.6	0.2	26	38	19	11	6	19.26	28.15	14.07	8.15	3.57	571.43	28.70	358.72
	740	80	0.5	0.2	26	38	19	11	6	19.26	28.15	14.07	8.15	3.57	476.19	23.91	298.94
A3	740	80	0.7	0.2	31	43	14	6	6	25.31	35.10	11.43	4.90	3.93	666.67	33.48	418.51
	740	80	0.6	0.2	31	43	14	6	6	25.31	35.10	11.43	4.90	3.93	571.43	28.70	358.72
	740	80	0.5	0.2	31	43	14	6	6	25.31	35.10	11.43	4.90	3.93	476.19	23.91	298.94
B1	740	80	0.7	0.2	40	43	4	5	4	30.71	33.06	3.26	4.06	2.62	666.67	33.48	418.51
	740	80	0.6	0.2	40	43	4	5	4	30.71	33.06	3.26	4.06	2.62	571.43	28.70	358.72
	740	80	0.5	0.2	40	43	4	5	4	30.71	33.06	3.26	4.06	2.62	476.19	23.91	298.94
B2	740	80	0.7	0.2	44	46	4	2	4	35.53	37.05	2.84	1.85	2.28	666.67	33.48	418.51
	740	80	0.6	0.2	44	46	4	2	4	35.53	37.05	2.84	1.85	2.28	571.43	28.70	358.72
	740	80	0.5	0.2	44	46	4	2	4	35.53	37.05	2.84	1.85	2.28	476.19	23.91	298.94
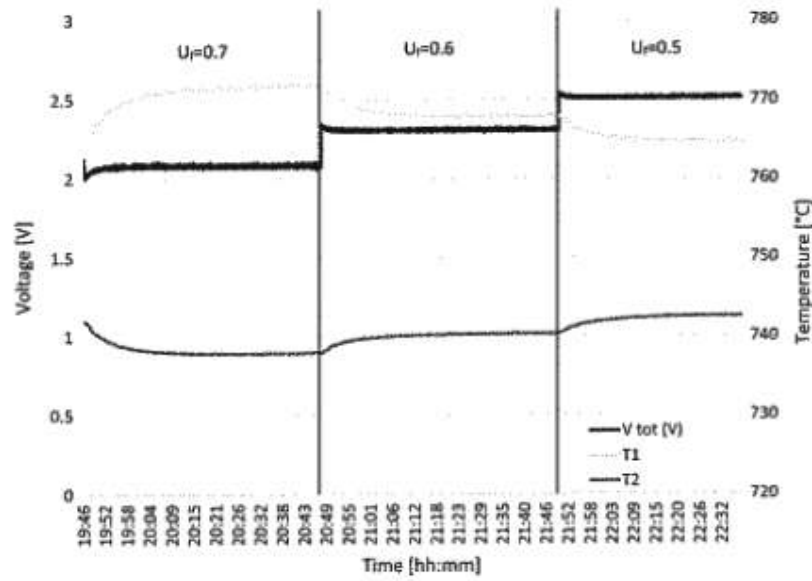
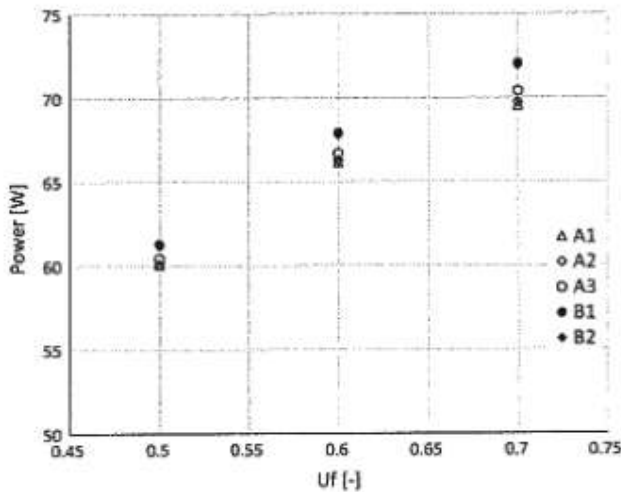Fig. 7. Temperature and voltage variation during test A2.

Fig. 8. Power as function of Uf for all tested compositions.

Main focus of the study is the evaluation of the effect of fuel composition on thermal equilibrium. As preliminary result, as expected and already assessed in previous studies [36], observing Fig. 7 it can be noted as stack temperatures differ due to high heat flow developed at gas inlet (T1). It is due to the high reaction rate occurring in the stack anodic compartment. Differently, the cathodic side (T2) suffers of the large coolant effect due to the high air flow rate entering at lower temperature.

Further considerations are made in reference to two main parameters: average temperature (Tav) between T1 (anode inlet) and T2 (cathode inlet) and temperature difference (DT) between the two values. The first parameter gives an indication of the heat amount that is released by the stack while the second one indicates the distribution of the heat inside the cells.

The graphs in Fig. 9 show that all the temperatures, obtained for different fuel compositions, have similar trends indicating that U_f effect does not differ with composition variation. Regarding Tav and DT absolute values, both graphs show an analogous thermal behavior of the short-stack between A1 and A2, that are very similar compositions. For the same reason, similar values were
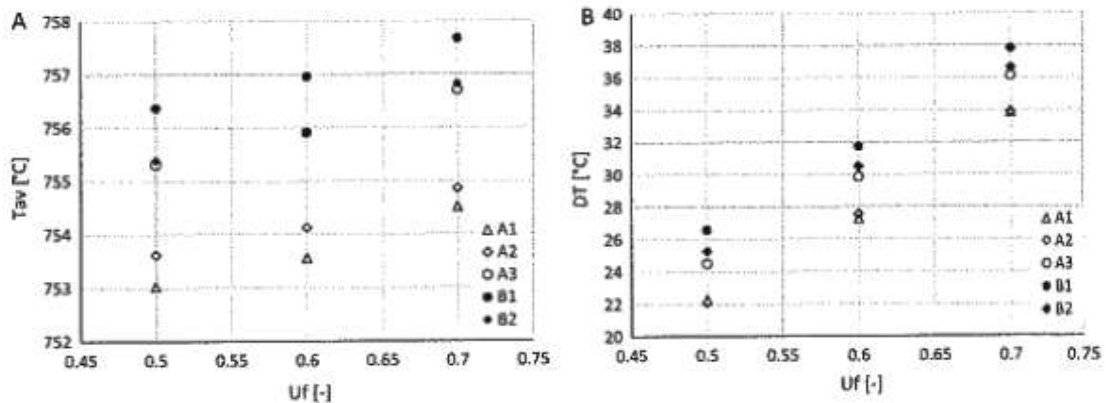

Fig. 9. Temperature analysis of tested conditions: average temperature (a) and temperature difference (b).
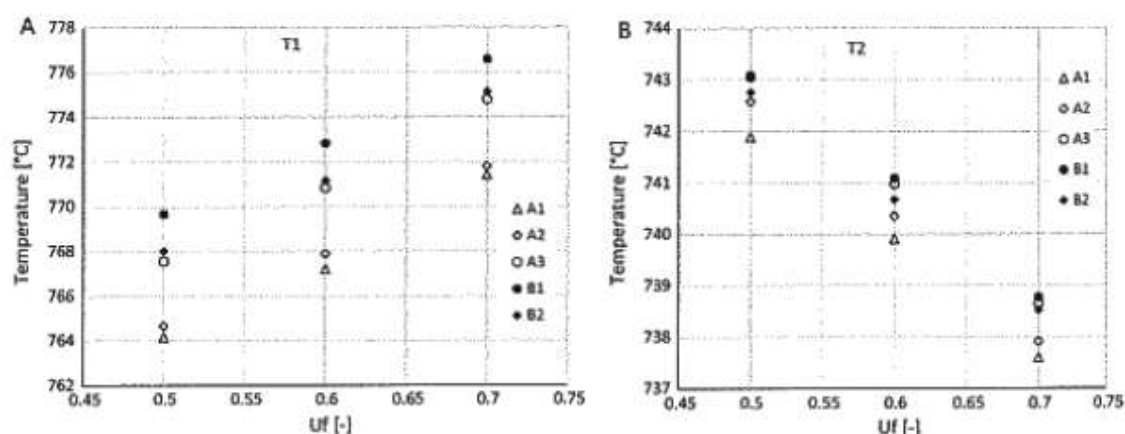
Fig. 10. Temperature analysis of tested conditions: T1 (a) and T2 (b).

obtained for A3 and B2, while the highest Tav and DT values arose in the case of B1 composition. Globally, temperature trends are correlated with fuel dilution. Specifically, both Tav and DT parameters increase at dilution decreasing. Anyway, Tav increases of 3 °C maximum varying the fuel composition, while a maximum increase of about 5 °C in the spatial temperature difference is measured. Consequently, the use of fuel mixtures produced through dry reforming doesn't significantly affect thermal stresses phenomena.

Graphs a and b of Fig. 10 report, in details, the trend of temperatures T1 and T2 respectively. The figure shows how, increasing U_f, T1, close to the anode inlet, increases while T2, close to the anode outlet (because of the counter-current design of the short-stack gas flow), decreases. These trends, increasing the reacted fuel flow rate with the current density (see Table 3), indicate the higher heat production by the electrochemical reaction inside the stack and the greater coolant effect at the cathode inlet. Moreover, T1 increase indicates that the reaction distribution is closer to the anode inlet, where the fuel enters into the stack. On the cathode side, the increase in U_f is related to an increase in the air flow rate (see Table 3), entering into the stack at lower temperature, with a consequent reduction in T2 close to the cathode inlet.

5. Conclusions

The present study moves from a novel concept of CHP, previously proposed by the authors, based on the coupling of SOFC with dry reforming unit. In a previous study it was proved as this architecture can allow electric and global efficiency values significantly higher with respect to an analogous steam methane reforming based system with anode recirculation (reduction of 10% in the CO_2 emission factor). To support and validate this novel system architecture, this paper addresses an experimental investigation of the performance of the single components when operated under the particular conditions resulting from their coupling. In particular, main focus of the paper is the investigation of short stack performance and thermal behavior in case of feeding with highly concentrated syngas compositions, as the ones produced by methane dry reforming. At this regards, it is remarked as these issues are not addressed in literature at the short stack level, specifically for what concerns the thermal behavior.

Inlet anode compositions chosen for the experimental campaign are based both on theoretical model prediction (compositions A) and experimental outcomes specifically performed on a dry reforming reactor (compositions B). The operation of SOFC short stack on dry reforming compositions is therefore assessed.

As expected, a greater produced power was obtained when higher concentrated fuel mixtures were used. For what above, among all the tested compositions the one obtained from dry reforming experiments (B1 and B2) are the most performing providing a power increase up to 3.6% with respect to mixture A1.

In addition, the obtained results show that highly concentrated compositions, like the ones tested, do not cause a significant increase in the stack temperature. In particular, considering a wide range of fuel compositions in terms of the inert fraction (from 27% of mixture A1 to 8.3% of mixture B2), Tav increases of 3 °C maximum, while a maximum increase of about 5 °C in the spatial temperature difference is measured. The results allow to exclude critical issues due to thermal stresses related to the use of highly concentrated fuels, supporting the feasibility of the coupling of dry reforming with SOFC with significant impact on CHP applications at the intermediate power range. Further studies will focus on long term operation to investigate the occurrence of carbon deposition.

References

[1] Marketsandmarkets.com. Europe Fuel Cell Technology Market: By Applications (Portable, Stationary, Transport), Types (PEMFC, DMFC, PAFC, SOFC, MCFC), Fuel (Hydrogen, Natural Gas, Methanol, Anaerobic Digester Gas) & Geography-European Trends And Forecast To 2018; 2013.
[2] FUEL CELLS AND HYDROGEN JOINT UNDERTAKING (FCH2 JU). Multi - Annual Work Plan 2014–2020; 2014.
[3] Barelli L, Ottaviano PA. Solid oxide fuel cell technology coupled with methane dry reforming: a viable option for high efficiency plant with reduced CO_2 emissions. Energy 2014;71:118–29.
[4] Desideri U, Barelli L. Solid oxide fuel cell (SOFC). Handbook of clean energy systems. Chichester, UK: John Wiley & Sons, Ltd; 2015.
[5] Guerra C, Lanzini A, Leone P, Santarelli M, Brandon NP. Optimization of dry reforming of methane over Ni/YSZ anodes for solid oxide fuel cells. J Power Sources 2014;245:154–63.
[6] Bonura G, Cannilla C, Frusteri F. Ceria-gadolinia supported NiCu catalyst: a suitable system for dry reforming of biogas to feed a solid oxide fuel cell (SOFC). Appl Catal B Environ 2012;121–122:135–47.
[7] Lanzini A, Leone P, Guerra C, Smeacetto F, Brandon NP, Santarelli M. Durability of anode supported Solid Oxides Fuel Cells (SOFC) under direct dry-reforming of methane. Chem Eng J 2013;220:254–63.

[8] Lanzini A, Guerra C, Leone P, Santarelli M, Smeacetto F, Fiorilli S, et al. Influence of the microstructure on the catalytic properties of SOFC anodes under dry reforming of methane. Mater Lett 2016;164:312–5.

[9] Cordiner S, Feola M, Mulone V, Romanelli F. Analysis of a SOFC energy generation system fuelled with biomass reformate. Appl Therm Eng 2007;27:738–47.

[10] Menon V, Banerjee A, Dailly J, Deutschmann O. Numerical analysis of mass and heat transport in proton-conducting SOFCs with direct internal reforming. Appl Energy 2015;149:161–75.

[11] Pillai M, Lin Y, Zhu H, Kee RJ, Barnett SA. Stability and coking of direct-methane solid oxide fuel cells: effect of CO₂ and air additions. J Power Sources 2010;195:271–9.

[12] Jang W-J, Jeong D-W, Shim J-O, Kim H-M, Roh H-S, Son IH, et al. Combined steam and carbon dioxide reforming of methane and side reactions: thermodynamic equilibrium analysis and experimental application. Appl Energy 2016;173:80–91.

[13] Liso V, Olesen AC, Nielsen MP, Kær SK. Performance comparison between partial oxidation and methane steam reforming processes for solid oxide fuel cell (SOFC) micro combined heat and power (CHP) system. Energy 2011;36:4216–26.

[14] Bocci E, Sisinni M, Moneti M, Vecchione L, Di Carlo A, Villarini M. State of art of small scale biomass gasification power systems: a review of the different typologies. Energy Procedia 2014;45:247–56.

[15] Lid Din Z, Zainal ZA. Biomass integrated gasification-SOFC systems: technology overview. Renew Sustain Energy Rev 2016;53:1356–76.

[16] Alzate-Restrepo V, Hill JM. Carbon deposition on Ni/YSZ anodes exposed to CO/H₂ feeds. J Power Sources 2010;195:1344–51.

[17] Baron S, Brandon NP, Atkinson A, Steele B, Rudkin R. The impact of wood-derived gasification gases on Ni-CGO anodes in intermediate temperature solid oxide fuel cells. J Power Sources 2004;126:58–66.

[18] Burnette DD, Kremer GG, Bayless DJ. The use of hydrogen-depleted coal syngas in solid oxide fuel cells. J Power Sources 2008;182:329–33.

[19] Shi Y, Li C, Cai N. Experimental characterization and mechanistic modeling of carbon monoxide fueled solid oxide fuel cell. J Power Sources 2011;196:5526–37.

[20] Homel M, Gür TM, Koh J-H, Virkar AV. Carbon monoxide-fueled solid oxide fuel cell. J Power Sources 2010;195:6367–72.

[21] Offer GJ, Brandon NP. The effect of current density and temperature on the degradation of nickel cermet electrodes by carbon monoxide in solid oxide fuel cells. Chem Eng Sci 2009;64:2291–300.

[22] Ye X-F, Wang SR, Zhou J, Zeng FR, Nie HW, Wen TL. Assessment of the performance of Ni-yttria-stabilized zirconia anodes in anode-supported Solid Oxide Fuel Cells operating on H₂–CO syngas fuels. J Power Sources 2010;195:7264–7.

[23] Li C-X, Yun L-L, Zhang Y, Li C-J, Guo L-J. Microstructure, performance and stability of Ni/Al₂O₃ cermet-supported SOFC operating with coal-based syngas produced using supercritical water. Int J Hydrogen Energy 2012;37:13001–6.

[24] Ma T, Yan M, Zeng M, Yuan J, Chen Q, Sundén B, et al. Parameter study of transient carbon deposition effect on the performance of a planar solid oxide fuel cell. Appl Energy 2015;152:217–28.

[25] Papurello D, Borchiellini R, Bareschino P, Chiodo V, Freni S, Lanzini A, et al. Performance of a Solid Oxide Fuel Cell short-stack with biogas feeding. Appl Energy 2014;125:254–63.

[26] Penchini D, Cinti G, Discepoli G, Sisani E, Desideri U. Characterization of a 100 W SOFC stack fed by carbon monoxide rich fuels. Int J Hydrogen Energy 2013;38:525–31.

[27] Barelli L, Bidini G, Corradetti A, Desideri U. Production of hydrogen through the carbonation–calcination reaction applied to CH₄/CO₂ mixtures. Energy 2007;32:834–43.

[28] Barelli L, Bidini G, Di Michele A, Gallorini F, Petrillo C, Sacchetti F. Synthesis and test of sorbents based on calcium aluminates for SE-SR. Appl Energy 2014;127:81–92.

[29] Barelli L, Bidini G, Gallorini F. SE-SR with sorbents based on calcium aluminates: process optimization. Appl Energy 2015;143:110–8.

[30] Barelli L, Bidini G, Corradetti A, Desideri U. Study of the carbonation-calcination reaction applied to the hydrogen production from syngas. Energy 2007;32:697–710.

[31] Alves HJ, Bley Junior C, Niklevicz RR, Frigo EP, Frigo MS, Coimbra-Araújo CH. Overview of hydrogen production technologies from biogas and the applications in fuel cells. Int J Hydrogen Energy 2013;38:5215–25.

[32] Lavoie J-M. Review on dry reforming of methane, a potentially more environmentally-friendly approach to the increasing natural gas exploitation. Front Chem 2014;2:81.

[33] Fang Q, Blum L, Peters R, Peksen M, Batfalsky P, Stolten D. SOFC stack performance under high fuel utilization. Int J Hydrogen Energy 2015;40:1128–36.

[34] Aslannejad H, Barelli L, Babaie A, Bozorgmehri S. Effect of air addition to methane on performance stability and coking over NiO-YSZ anodes of SOFC. Appl Energy 2016;177:179–86.

[35] Chen T, Wang WG, Miao H, Li T, Xu C. Evaluation of carbon deposition behavior on the nickel/yttrium-stabilized zirconia anode-supported fuel cell fueled with simulated syngas. J Power Sources 2011;196:2461–8.

[36] Barelli L, Cinti G, Desideri U, Ottaviano PA. SOFC thermal transients: modeling by application of experimental system identification techniques. Fuel Cells 2014;14:107–22.
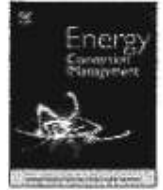
SOFC regulation at constant temperature: Experimental test and data regression study

L. Barelli [a,*], G. Bidini [a], G. Cinti [a], A. Ottaviano [b]

[a] Department of Engineering, University of Perugia, Via G. Duranti 1/A4, Perugia 06125, Italy
[b] Department of Engineering, University of Napoli "Parthenope", Centro Direzionale Isola C4, Napoli 80143, Italy

ARTICLE INFO

ABSTRACT

The operating temperature of solid oxide fuel cell stack (SOFC) is an important parameter to be controlled, which impacts the SOFC performance and its lifetime. Rapid temperature change implies a significant temperature differences between the surface and the mean body leading to a state of thermal shock. Thermal shock and thermal cycling introduce stress in a material due to temperature differences between the surface and the interior, or between different regions of the cell. In this context, in order to determine a control law that permit to maintain constant the fuel cell temperature varying the electrical load and the infeed fuel mixture, an experimental activity were carried out on a planar SOFC short stack to analyse stack temperature. Specifically, three different anodic inlet gas compositions were tested: pure hydrogen, reformed natural gas with steam to carbon ratio equal to 2 and 2.5. By processing the obtained results, a regression law was defined to regulate the air flow rate to be provided to the fuel cell to maintain constant its operating temperature varying its operating conditions.

© 2016 Elsevier Ltd. All rights reserved.

1. Introduction

In solid oxide fuel cell (SOFC) systems, thermal management is a critical issue to prevent damage and improve fuel cell life. In particular, SOFC stack lifetime can be directly linked to the stack performance degradation which depends partly on to the stack structure and materials, but also on the conditions that stack is operated in. Inappropriate control during start-up and shutdown and/or following of the electrical power demand, severe characterisation procedures and thermal cycling can induce cell failures [1–4].

In fact, stresses induced by the difference in thermal expansion coefficients of the ceramic and metal components, can lead to thermal stress phenomena causing serious problems in SOFC operation as thoroughly reviewed in [5]. In fact, as emphasized in [6,7], the bigger temperature variations are, the larger are the mechanical stresses in the fuel cell structure due to the mismatch in stack constituent materials.

Consequently, the minimization of thermal gradients, cause of cell degradation and failure [7–11], allowing SOFC operation near to constant temperature, is a very crucial issue [12].

As anticipated, both temperature time variation and spatial gradients can be considered cause of thermal problems. To reduce thermal stresses and ensure system reliability, it is critical to enforce constraints in terms of maximum temperature and spatial temperature variations during SOFCs transient operation. As indicated in [13,14], a high risk of cell failure occurs in case of excessive temperature gradients, starting from a very high temperature. In [15], in order to couple safe operation and high system efficiency during load tracking, a model for a 5 kW stand-alone SOFC system was developed. Specifically the effect of the bypass valve on SOFC system performance and temperature was analyzed.

Due to the difficult of experimental investigations of SOFC operation under unsteady conditions, a numerical approach can be most usable. Indeed, a considerable number of studies focused on numerical models to predict thermal distribution [16–18] is available.

So in order to understand the evolution of the thermal gradient/stress and its effects on SOFC lifetime, [19,20] show a three-dimensional numerical model suitable to determine, during SOFC transients, the temperature profiles together with the trends of current density, activation overpotential and gas concentration.

[21], instead, explains a 1D multiphysics SOFC dynamic model usable to predict the non-uniform distributions of current density, gas pressure and, above all, SOFC temperature during its operation. Moreover, a wide discussion about dynamic SOFC modelling can be also found in [22,23].

* Corresponding author.
  E-mail address: linda.barelli@unipg.it (L. Barelli).

The interest in controlling the cell temperature within safety limits, is also addressed in studies of hybrid systems based on SOFC [24–26]. In [27], a new tool, which combines feed-forward and standard proportional–integral techniques, was developed in order to avoid failures and stress conditions during load changes. Specifically, authors asserted that this new control method permits to better control fuel cell temperature with a maximum gradient significantly lower than 3 K/min.

In [28,29], the temperature control is based on decentralized PI and PID controllers (proportional-integral-derivative), which are tuned by utilizing the model so to manipulate air flow to achieve the desired SOFC temperature. In particular [28] refers to the particular configuration of internal reforming solid oxide fuel cell, while the analysis proposed in [29] are based only on theoretical assumptions. In [30] a generalized predictive control (MIMO-GPC) is applied to regulate the maximum temperature and its results are compared with standard PID controller.

[31,32] show a novel concept for thermal management of SOFC. Specifically, in [31] the design involves a secondary air channel to control cell temperature. In [32] a model including an air bypass valve was analyzed to achieve maximum system performance and operation ability during load following operation.

The research work here presented, focused on planar SOFC technology with external reforming, differs from what discussed in literature. Specifically, it does not propose a new design or a variation of the fuel cell structure, but it aims, through a rigorous approach, at the adjustment of the air flow, i.e. oxygen utilization factor, to maintain constant cell temperature during load transients. Moreover, the study was performed considering different feeding gas compositions.
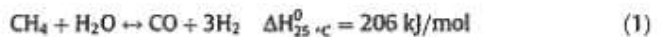
For this purpose, tests were carried out on a SOFC short stack. All the physical parameters of interest (cell temperature, inlet air flow rate, fuel flow, etc.) were monitored varying the electrical load and the infeed fuel mixture. By processing the obtained results, it was implemented a regression law that determines, under a specific anodic feeding composition, the needed air flow rate to maintain constant its operating temperature varying cell load.

In the future, achieved results will be implemented in dynamic models of SOFC-based systems, including hybrid SOFC-GT cycles, to deep investigate how this control strategy of the fuel cell (i.e. invariable operating temperature in load-following operation) impacts on regulation of BoP components and, in case of hybrid systems, other sub-sections.

2. Method

The experimental activity aim is to evaluate relation between air flow and average stack temperature. The air flow rate values which guarantee a constant stack temperature were determined varying the load conditions in terms of equivalent hydrogen in input. For the experimental campaign air flow variations are imposed in terms of oxidant utilization (U_{ox}).

The testing activity was performed considering three different cases corresponding to three inlet gas mix compositions (Table 1): pure hydrogen (REF), reformed natural gas with steam to carbon (S/C) 2 (REF2) and reformed natural gas with S/C = 2.5 (REF25). Gas compositions were simulated using pure gasses mix and the concentrations were calculated theoretically considering chemical equilibrium of both steam reforming and shift reactions. Complete transformation of methane, 100% steam reforming, was considered while shift reaction was supposed to have an equilibrium of 34% CO reaction as resulting from simulation carried out at about 650 °C (imposing chemical equilibrium status).

$$CH_4 + H_2O \leftrightarrow CO + 3H_2 \quad \Delta H_{25 \, °C}^0 = 206 \text{ kJ/mol} \quad (1)$$

$$CO + H_2O \leftrightarrow CO_2 + H_2 \quad \Delta H_{25 \, °C}^0 = -41 \text{ kJ/mol} \quad (2)$$

Test campaign is based on three main parameters: equivalent hydrogen ($\dot{n}_{H2eq}$), U_{ox} and fuel utilization (U_f). $\dot{n}_{H2eq}$, expressed by Eq. (3), is directly related to the power of the cell, while U_f and U_{ox} refer to the amount of reacting inlet streams compared to overall feeding flow-rates (Eqs. (4) and (5)). In the following, all parameters are defined:

$$\dot{n}_{H2eq} = \dot{n}_{H2} + \dot{n}_{CO} + 4 \cdot \dot{n}_{CH4} \quad (3)$$

$$U_f = \frac{I \cdot c}{2F\dot{n}_{H2eq}} \quad (4)$$

$$U_{ox} = \frac{I \cdot c}{4F\dot{n}_{Air}} \quad (5)$$

where $\dot{n}_{H2}$, $\dot{n}_{CO}$ and $\dot{n}_{CH4}$ are molar flows of hydrogen (mol s^{-1}), carbon monoxide and methane respectively related to the anodic feeding composition, $\dot{n}_{Air}$ is the molar flow of air (mol s^{-1}), I is total current (A), c is the number of cells and F is the Faraday constant (C mol^{-1}).

For each defined gas mix only U_{ox} and $\dot{n}_{H2eq}$ parameters were varied while U_f was kept constant at 0.7. This choice is justified by the study target, or rather to relate the effect of power and air variation so to keep constant stack temperature. Consequently, power variation was realized keeping U_f constant and varying the inlet flow, defined via $\dot{n}_{H2eq}$, so to keep stack efficiency – related to U_f – as high as possible and operate the system in conditions similar to real ones. The variation of $\dot{n}_{H2eq}$ was realized to cover a high window of operation from 100 Nl h^{-1} down to 40 Nl h^{-1}.

Regarding the test campaign planning, for each anode feeding composition, different load conditions were investigated via

Table 1
Gas composition used during the test.

Gas MIX	H$_2$ (%)	CO (%)	CO$_2$ (%)	H$_2$O (%)	CH$_4$ (%)
REF	100	–	–	–	–
REF2	66.80	13.20	6.80	13.20	–
REF25	60.73	12	6.18	21.09	–

Table 2
Test campaign.

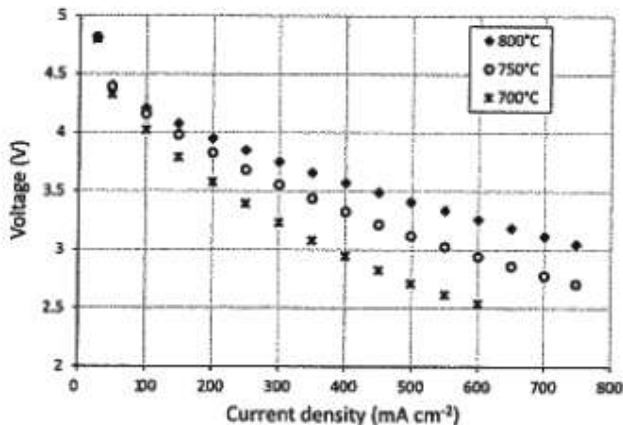| Gas MIX	$\dot{q}_{H2eq}$ (Nl h^{-1})	U_f (–)	U_{ox} (–)
REF	40–60–80–100	0.7	0.3–0.35–0.4–0.45
REF2	40–60–80–100	0.7	0.3–0.35–0.4–0.45
REF25	40–60–80	0.7	0.25–0.3–0.35–0.4–0.45

Fig. 1. Short stack polarization curves at 800 °C, 750 °C and 700 °C.

setting $\dot{n}_{H2eq}$ values indicated in Table 2. Moreover, for each load condition, a U_{ox} study was performed varying air feeding flow rate. In particular, values indicated in Table 2. were imposed keeping constant total current and anode feeding condition, i.e. composition and $\dot{n}_{H2eq}$ characteristic of the particular U_{ox} study. A duration of one hour was set for each test, to reach thermal equilibrium under the specific investigated conditions (anode mixture, $\dot{n}_{H2eq}$, U_{ox}).

Table 2 reports parameters values used in the global test campaign. Note that due to high dilution, composition REF25 could not achieve the highest power obtained with an equivalent hydrogen flow rate of 100 Nl h^{-1} ($\dot{q}_{H2eq}$).

Usually in the test rig stack temperature is set with furnace temperature that, due to heat losses and temperature gradient, is higher or close to stack one. Keeping such approach no temperature variation can be measured because furnace reaction are faster than stack inertia with the result that stack remains at constant temperature. To solve the problem once reached operation condition, furnace temperature was decreased until stack minimum measured temperature was suitably higher than furnace. Following this procedure furnace temperature was set at 750 °C, obtaining average stack temperature in the range of 760–780 °C. This condition amplifies temperature variation and can be considered similar to real condition where the stack is covered with insulation (not present in short-stacks as the one used in this study for experimentation) and temperature losses are reduced to minimum.

3. Experimental set-up

The experimental test was performed on a 4 cell planar ASC SOFC short stack. The stack was supplied by Forschungszentrum Jülich. Cells are realized with commercial materials: Ni-8YSZ anode, 8YSZ electrolyte and LSM cathode. Cells are square size of 10 cm side while the stack is realized following the F-design. Polarization curves obtained under pure hydrogen feeding, respectively at 700, 750 and 800 °C operating temperature, are depicted in Fig. 1. The test rig was internally developed so to permits start-up and operation of the short stack. Temperature is controlled using a furnace hosting the stack and two cable heaters set anode and cathode inlet pipes temperature. Gas flows is measured with flow meter controllers while anode water is vaporized and mixed with other gases after measurement and its control is realized with a liquid meter. Both air and fuel gas are at ambient pressure during tests. Current is controlled with an electronic load, while SOFC cells temperatures are measured with two thermocouples, T1 and T2. Fig. 2 contains a picture of the stack mounted on the test rig and a sketch of T1 and T2 positions. Specifically, thermocouples are positioned in holes realized in the middle interconnection between cell 2 and cell 3. Note that T1 is close to fuel-in and air-out while, vice versa, T2 is close to fuel-out and air-in. Stack and test rig are deeper described elsewhere [33].

4. Results

Fig. 3. is an example of U_{ox} variation test. The graph reports temperature values, in details the two stack temperatures (T1, T2) and furnace temperature, U_{ox} and U_f. In this case the composition was REF and $\dot{q}_{H2eq}$ 80 Nl h^{-1}. U_f has constant value of 0.7 similarly to all the other tests. Main evidence of temperature variation is on stack temperature 2, close to air inlet. As expected, the increase of U_{ox} causes temperature increase due to lower air mass flow and decrease in relative coolant effect.

In order to have a more systematic view of the thermal behaviour, the mean values of T1 and T2 were calculated varying cathodic feeding composition and load conditions. Specifically, this value was estimated relating to the final 300 s of each test, when thermal equilibrium conditions are achieved.

Fig. 4 reports experimental results of REF composition. Stack temperature, calculated as average between T1 and T2 mean values indicated above, is reported as function of U_{ox} (a) and as function of power (b). As expected, higher temperatures are achieved with
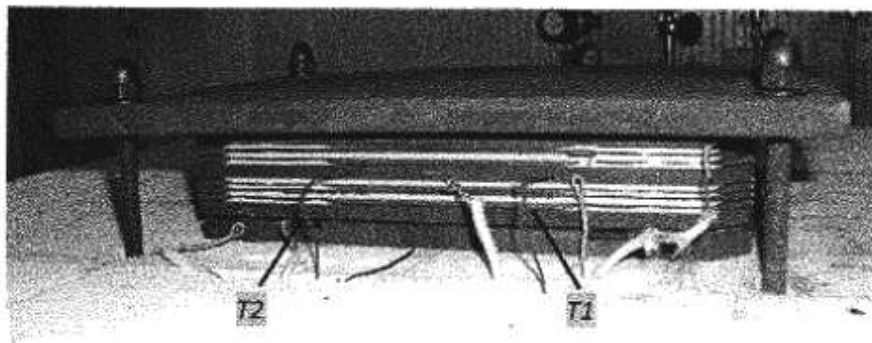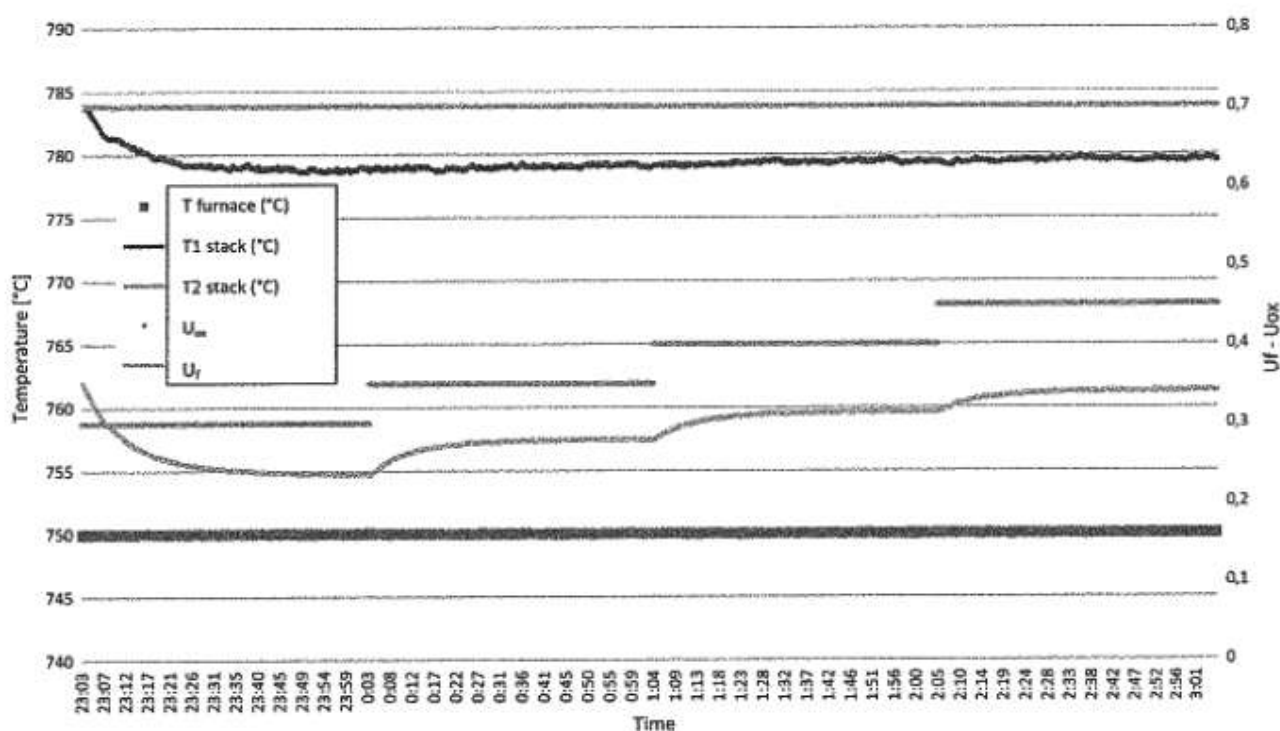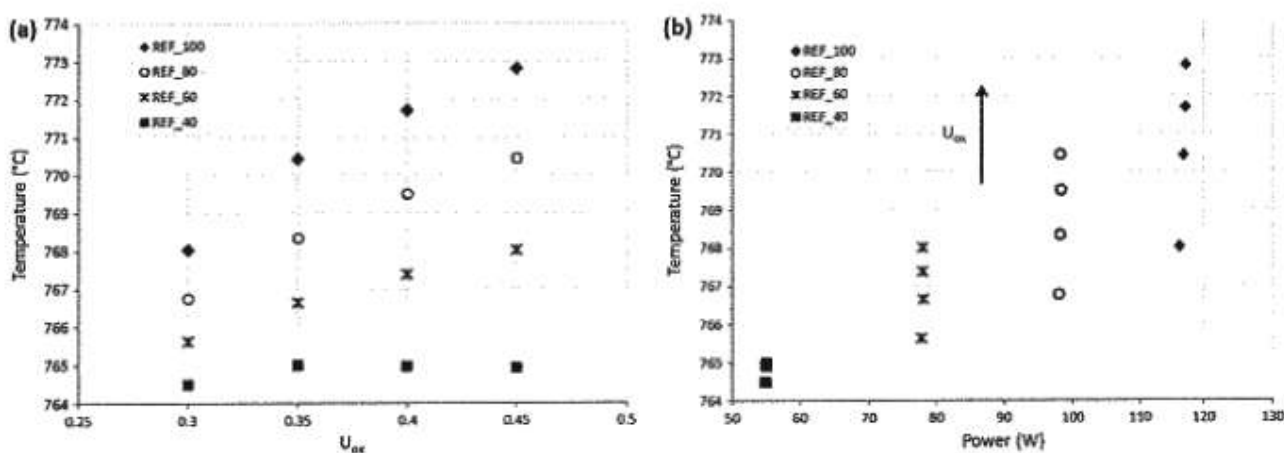

Fig. 2. T1 and T2 positions in the test rig.

Fig. 3. Time variation of U_{ox}.

Fig. 4. Stack temperature as function of U_{ox} (a) and of power (b) for REF tests. In Fig. 4b U_{ox} increases from down to top as indicated by the arrow.

higher $\dot{q}_{H2eq}$, corresponding to higher power. Such behaviour is related to the increase in heat production when the stack is operated at full rate power with respect to rate operation. The effect of air flow is well described by the depicted results, showing a temperature decrease with U_{ox} reduction: the effect of this parameter seems more relevant at higher power rate. At $\dot{q}_{H2eq}$ of 40 Nl h^{-1} the temperature control cannot be realized because an appreciable temperature variation does not occur. Both graphs (a) and (b) permit to evaluate that, varying stack power, operative temperature can be kept constant through a suitable U_{ox} variation. Specifically, in reference to the tested U_{ox} range, for REF composition the stack temperature control is possible only for higher power rates corresponding to $\dot{q}_{H2eq}$ in the range 60–100 Nl h^{-1}.

Similar considerations can be done analyzing Fig. 5 where results of REF2 test are reported. Stack temperature values are

similar to the ones obtained for REF composition and also in this case temperature control can be performed, in reference to the tested U_{ox} range, only for higher values of power ($\dot{q}_{H2eq}$ = 60–100 Nl h^{-1}).

Fig. 6 reports results of tests performed with REF25 composition. In this case an additional U_{ox} condition was introduced to obtain indication on the effect of U_{ox} and $\dot{q}_{H2eq}$ on temperature. With this composition, constant temperature could be obtained for lower $\dot{q}_{H2eq}$ compared to other compositions, mainly due to diluent effect of steam on performances. The higher steam content, in fact, causes decrease in OCV and, consequently, in operating voltage.

For completeness, Fig. 7 reports stack efficiency (determined on the basis of the produced power and the overall fuel flow rate entering into the short stack) in all operation conditions, in particular for compositions REF (a), REF2 (b) and REF25 (c). Results show
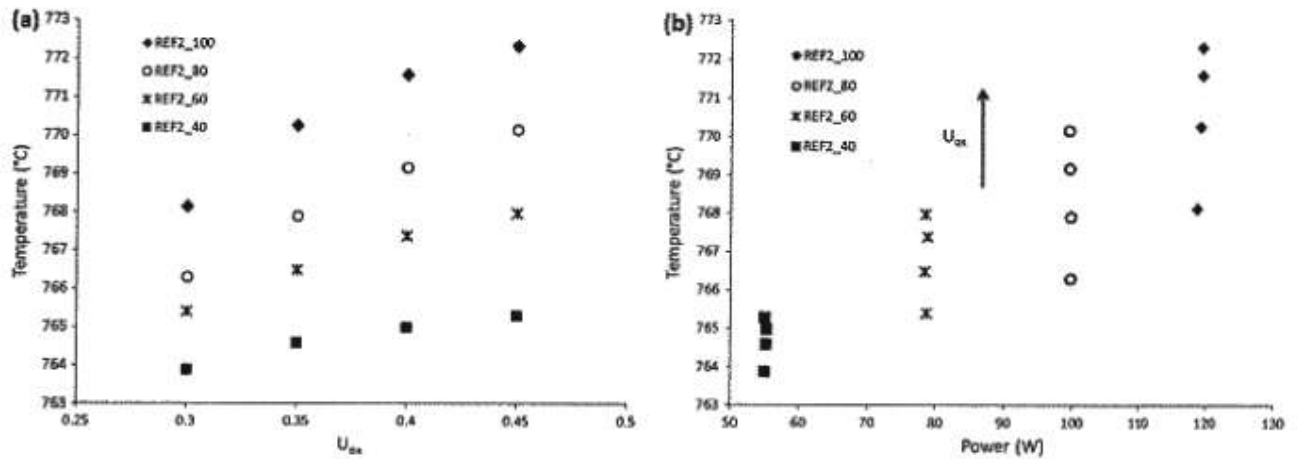
Fig. 5. Stack temperature as function of U_{ox} (a) and of power (b) for REF2 tests. In Fig. 5b U_{ox} increases from down to top as indicated by the arrow.
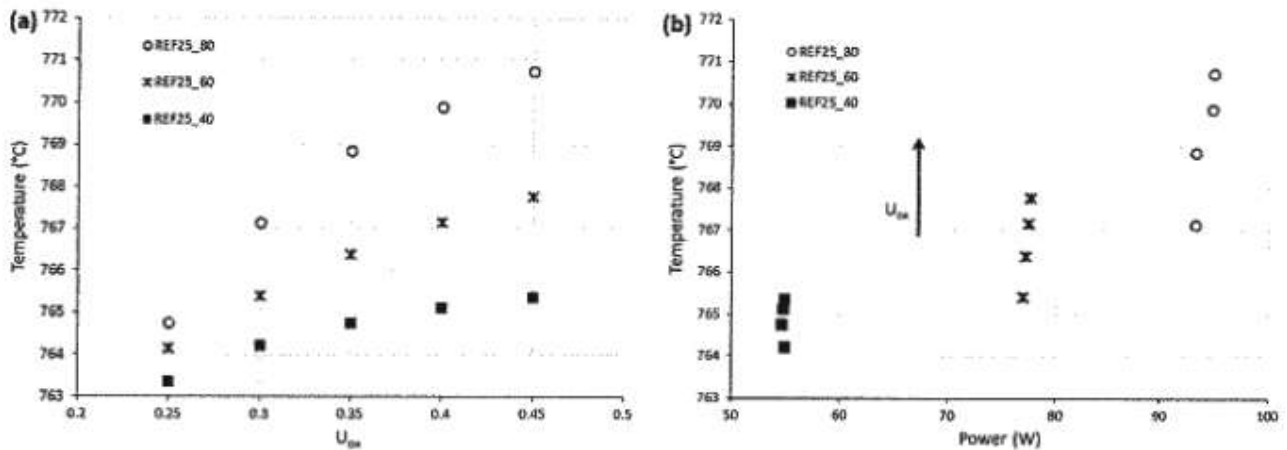

Fig. 6. Stack temperature as function of U_{ox} (a) and of power (b) for REF25 tests. In Fig. 6b U_{ox} increases from down to top as indicated by the arrow.

the efficiency increase with power reduction. This behaviour is typical of fuel cells. Compositions have a limited effect on efficiency, since it is mainly affected by U_f which is the same in all tests, with values slightly reduced for more diluted fuel mixtures.

4.1. Data analysis

In this section, obtained experimental data, presented in Section 4, were analyzed in order to find a regression law that allows the adjustment of cathodic air with a consequent U_{ox} regulation, to maintain stack temperature almost constant varying FC operating point. Firstly, it was identified the temperature to be held constant in presence of stack load variations, regulating U_{ox} parameter.

Regarding the first part of test campaign (gas mix REF), results are shown in Fig. 4b and in Table 3. An almost constant temperature trend, about 768 °C, was identified in the three operating conditions characterized by U_{ox} and $\dot{q}_{H2eq}$ (Nl h^{-1}) equal respectively to: 0.45–60, 0.35–80 and 0.3–100 (indicated in bold in Table 3).

As already discussed in Section 4, for REF composition, temperature control is possible only for higher power rates corresponding to $\dot{q}_{H2eq}$ in the range 60–100 Nl h^{-1}. Therefore, results at 4 Nl h^{-1} are no longer considered.

The operative temperature of 768 °C resulted also for REF2 test (Table 4). Specifically, this temperature level was obtained with U_{ox} and $\dot{q}_{H2eq}$ conditions of: 0.45–60, 0.35–80 and 0.3–100 (highlighted in bold in Table 4).

Table 5 shows temperatures values obtained with REF25 feeding composition. In this case, considering the too low temperatures obtained at 40 Nl h^{-1} H$_{2eq}$ (similarly to previous cases) and the lack of values for 100 Nl h^{-1} H$_{2eq}$, as already discussed in Section 4, operating stack temperature of about 767 °C arose under 60 and 80 Nl h^{-1} H$_{2eq}$ with 0.3 and 0.4 U_{ox} respectively (highlighted in bold in Table 5).

For each identified $\dot{q}_{H2eq}$ and U_{ox} values that ensure a constant operating temperature varying the gas composition, the corresponding experimental values of stack inlet air ($\dot{q}_{Air\_in}$), averaged as four temperatures, are summarized in Table 6.

Table 6 shows $\dot{q}_{Air\_in}$ values subsequently used for the determination of the correlation equations among operative conditions (anodic mixture, $\dot{q}_{H2eq}$) and air flowrate to guarantee stack operation at constant temperature. To get results as general as possible, power variations (proportional to the inlet H$_{2eq}$ flow rate and to the stack efficiency) were considered in percentage terms. In other words, the flow rate of 100 Nl h^{-1} H$_{2eq}$, which allows to reach the maximum stack power, was taken as the nominal capacity because it represents the 100% power value. Moreover, the other $\dot{q}_{H2eq}$ values, considering the electric efficiency determined in the experimental campaign, stand for 84%, 66% and 46% of nominal power. The values in bold of Table 6, corresponding to the working point characterized by 84% of nominal load and REF2 composition, are not used here for the evaluation of the correlation equations, because they will be subsequently used to test the regression law.
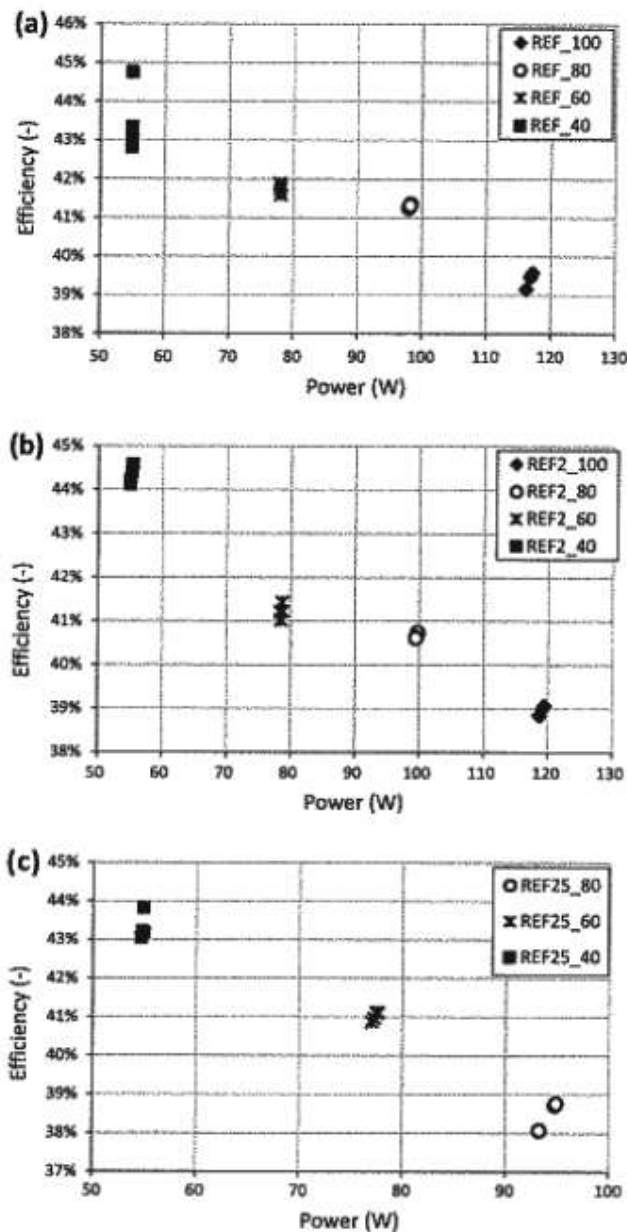
Fig. 7. Stack efficiency as function of power and $\dot{q}_{H2eq}$ with composition REF(a) REF2 (b) and REF25 (c).

Table 3
Test REF: temperature values (°C) Vs $\dot{q}_{H2eq}$ and U_{ox}.

REF	$\dot{q}_{H2eq}$ (Nl h^{-1})		
U_{ox}	60	80	100
0.3	765.62	766.77	768.03
0.35	766.65	768.34	770.42
0.4	767.39	769.51	771.70
0.45	768.01	770.44	772.81

Regression was firstly performed for each anodic mixture and then generalized to get results for any gas composition within the variation range represented by REF, REF2 and REF25. Below, Table 7 reports the equations that correlate, for each fuel mixture, $\dot{q}_{Air\_in}$ values (y) to percentage power (x), to maintain the temperature set-point.

Table 4
Test REF2: temperature values (°C) Vs $\dot{q}_{H2eq}$ and U_{ox}.

REF2	$\dot{q}_{H2eq}$ (Nl h^{-1})		
U_{ox}	60	80	100
0.3	765.41	766.30	**768.13**
0.35	766.49	**767.90**	770.25
0.4	767.38	769.18	771.58
0.45	**767.97**	770.15	772.32

Table 5
Test REF25: temperature values (°C) Vs $\dot{q}_{H2eq}$ and U_{ox}.

REF25	$\dot{q}_{H2eq}$ (Nl h^{-1})	
U_{ox}	60	80
0.3	765.40	**767.14**
0.35	766.39	768.85
0.4	**767.15**	769.90
0.45	767.77	770.73

Table 8 shows the comparison between $\dot{q}_{Air\_in}$ values calculated by Eqs. (6)–(8) (Table 7) and the ones obtained experimentally. It can be easily noted that determined equations provide the same or very close values for each feeding gas mix. Moreover, a prediction of $\dot{q}_{Air\_in}$ values, out of the U_{ox} range tested in previous experiments, can be estimated to provide air flow conditions which guarantee stack temperature control at extreme power conditions: i.e. 46% power for all anodic feeding mixtures and 100% power for REF25 case.

Aiming to estimate the required air to ensure constant stack temperature varying both load and gas feeding mix, a regression on the angular coefficients (a) and the constants terms (b) of Eqs. (6)–(8) was performed. Specifically, a high accuracy was obtained correlating a and b terms to dilution factor (DF) and hydrogen content (X_{H2}) characteristic of the anodic mixture as expressed by Eqs. (9) and (10) respectively.

$$DF = \frac{\dot{n}_{CO2} + \dot{n}_{H2O}}{\dot{n}_{CO2} + \dot{n}_{H2O} + \dot{n}_{H2} + \dot{n}_{CO}} \tag{9}$$

$$X_{H2} = \frac{\dot{n}_{H2}}{\dot{n}_{CO2} + \dot{n}_{H2O} + \dot{n}_{H2} + \dot{n}_{CO}} \tag{10}$$

Table 9 summarizes the available values relative to the REF, REF2 and REF25 cases.

In order to combine DF and X_{H2} and to obtain, at the same time, the best fit with coefficients a and b (Eqs. (12) and (13), a model parameter z was defined in Eq. (11).

$$z = \frac{e^{DF}}{1 - DF} + X_{H2}^2 \cdot (1 - DF) \tag{11}$$

$$a = 5{,}044.83 \cdot z^2 - 19{,}318.32 \cdot z + 19{,}490.97 \tag{12}$$

$$b = -287.59 \cdot z + 294.26 \tag{13}$$

Fig. 8(a) and (b) show the trend of Eqs. (12) and (13) respectively. Continuous lines are trends of parameters a and b versus z, while marked points represent values used for fitting.

For a general SOFC operative condition, the model can be applied initially evaluating z parameter (Eq. (11)) in function of the real anodic mixture (DF, X_{H2}). Then, after the determination of a and b coefficients (Eqs. (12) and (13), the air flowrate value can be determined according to a linear function (a is the angular coefficient and b the constant term) known the specific load characteristic of the investigated operating condition.

This procedure was applied to the test conditions of Table 10 and the obtained data, summarized in Table 10, provided a model accuracy, esteemed on the working points used for the regression

Table 6
Reference conditions for each gas mix. Bold values correspond to the working point used for the regression law validation.

	REF			REF2			REF25	
$\dot{q}_{H2eq}$ (Nl h^{-1})	60	80	100	60	80	100	60	80
U_{ox}	0.45	0.35	0.3	0.45	**0.35**	0.3	0.4	0.3
$\dot{q}_{Air\_in}$ (Nl h^{-1})	222.0	380.9	555.5	231.2	**380.4**	554.1	256.3	443.9

Table 7
Equations: Air$_{in}$ (Nl h^{-1}) Vs Power (%).

Gas Mix	Correlation equations	
REF	$y = 833.65x - 280.78$	(6)
REF2	$y = 807.78x - 253.09$	(7)
REF25	$y = 938x - 306.5$	(8)

Table 8
$\dot{q}_{Air\_in}$ values (Nl h^{-1}): experimentals (Exp) Vs calculated (Eq.). The bold value corresponds to the working point used for the regression law validation.

Power	$\dot{q}_{H2eq}$	$\dot{q}_{Air\_in}$ (Nl h^{-1})					
		REF		REF2		REF25	
(%)	(Nl h^{-1})	Exp	Eq. (6)	Exp	Eq. (7)	Exp	Eq. (8)
46%	40	–	52.42	–	70.02	–	68.7
66%	60	222.0	219.02	231.2	231.58	256.3	256.3
84%	80	380.9	385.62	**380.4**	–	443.9	443.9
100%	100	555.5	552.22	554.1	554.69	–	631.5

Table 9
Regression parameters.

DF	X_{H2}	a	b
0	1	833.65	−280.78
0.2	0.686	807.78	−253.09
0.27	0.633	938	−306

law development, of about 1.5% in terms of normalized root mean square error.

To validate this performance, the regression model was tested on the working point characterized by 84% power and REF2 composition (DF = 0.2, X_{H2} = 0.686), previously not used in the development phase. The simulated $\dot{q}_{Air\_in}$ value for such a working point is reported in Table 10 (in bold), together with the corresponding experimental value. As it can be noted, the model predicts an air flow rate of 392.7 Nl h^{-1} instead of 380.4 Nl h^{-1} with an error of about 3%.

Globally, the developed regression law can be applied to SOFC stack regulation in the range of:

– 66–100% SOFC power,
– anodic feeding gases with hydrogen molar content (X_{H2}) over 63% and dilution factor up to 27%.

In this way, knowing the infeed mixture composition (DF, X_{H2}) together with the operating point (% of power), it will be possible to calculate the air flow rate, and so U_{ox} value, required to maintain the constant operating temperature.

5. Conclusions

SOFC thermal management is a fundamental issue to prevent damage and improve fuel cell lifetime. Inappropriate temperature control during load following can induce cell performance issues and failures. An experimental activity was carried out to link the air infeed flowrate value with the SOFC average stack temperature, and in particular, to determine air amount which guarantees a constant stack temperature varying required load (i.e. power percentage) and fuel composition. The experimental test was performed on a 4 cells planar SOFC short stack.

Three different inlet gas compositions were tested (anodic side): pure hydrogen (REF), reformed natural gas with S/C 2 (REF2) and 2.5 (REF25). For each tested mixture, it was identified the temperature value to be held constant in presence of stack load variations, regulating $\dot{q}_{Air\_in}$ and, consequently, U_{ox} parameter.

Basing on experimental results, a general regression law was estimated to get the air flow rate $\dot{q}_{Air\_in}$ (with high accuracy), known the required load and the anodic feeding composition, in terms of characteristic dilution factor (DF) and hydrogen content
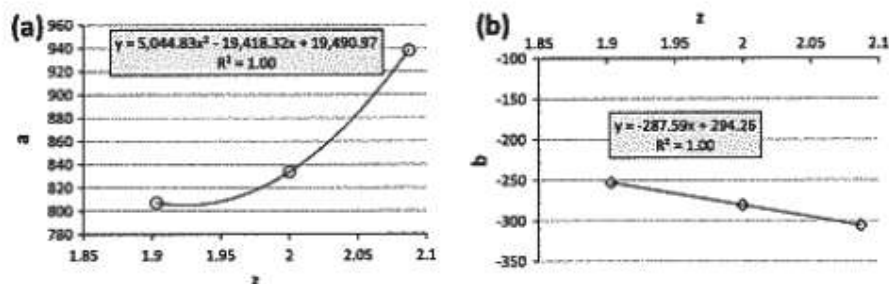
Fig. 8. Fitting of a and b coefficient.

Table 10
Application and performance of regression procedure. The bold value corresponds to the working point used for the regression law validation.

DF	X_{H2}	z	a	b	% Power			Simulated $\dot{q}_{Air\_in}$ (Nl h^{-1})			Experimental $\dot{q}_{Air\_in}$ (Nl h^{-1})		
0	1	2	821.20	−282.20	0.66	0.84	1	219.3	386.0	552.7	222	380.9	555.5
0.2	0.686	1.90	795.13	−256.56	0.66	**0.84**	1	231.3	**392.7**	554.2	231.2	**380.4**	554.1
0.27	0.633	2.09	925.03	−305.25	0.66	0.84	–	256.9	444.5	–	256.3	443.9	–

(X_{H2}). This law was validated on an experimental working point, providing an error of 3%. Globally, it can be applied to SOFC stack regulation at constant operating temperature in the range of:

- 66–100% SOFC power,
- anodic feeding gases with hydrogen molar content (X_{H2}) over 63% and dilution factor up to 27%.

Impacts of this stack control strategy on operative conditions of other system components will be investigated in future works. Specifically, it will be implemented in dynamic models of SOFC-based systems (included SOFC-GT cycles) in order to determine the effect of the required air regulation on the control strategy of the whole system.

References

[1] Nakajo A, Mueller F, Brouwer J, Van herle J, Favrat D. Mechanical reliability and durability of SOFC stacks. Part II: Modelling of mechanical failures during ageing and cycling. Int J Hydrogen Energy 2012;37:9269–86.
[2] Hagen A, Hendriksen PV, Frandsen HL, Thydén K, Barfod R. Durability study of SOFCs under cycling current load conditions. Fuel Cells 2009;9(6):814–22.
[3] Dikwal C, Bujalski W, Kendall K. The effect of temperature gradients on thermal cycling and isothermal ageing of microtubular solid oxide fuel cells. J Power Sources 2009;193(1):241–8.
[4] Knibbe R, Hauch A, Hjelm J, Ebbesen S, Mogensen M. Durability of solid oxide cells. Green 2011;1:141–69.
[5] Barelli L, Barluzzi E, Bidini G. Diagnosis methodology and technique for solid oxide fuel cells: a review. Int J Hydrogen Energy 2013;38(12):5060–74.
[6] Wuillemin Z, Nakajo A, Müller A, Schuler AJ, Diethelm S. Locally-resolved study of degradation in a SOFC repeat-element. ECS Trans 2009;25(2):457–66.
[7] Nakajo A, Wuillemin Z, Van Herle J, Favrat D. Simulation of thermal stresses in anode-supported solid oxide fuel cell stacks. Part I: Probability of failure of the cells. J Power Sources 2009;193:203–15.
[8] Nakajo A, Stiller C, Härkegård G, Bolland O. Modeling of thermal stresses and probability of survival of tubular SOFC. J Power Sources 2006;158:287–94.
[9] Barelli L, Cinti G, Desideri U, Ottaviano A. SOFC thermal transients: modeling by application of experimental system identification techniques. Fuel Cells 2014;14(1):107–22.
[10] Braun RJ, Tyrone LV, Huayang Z, Robert JK. Analysis, optimization, and control of solid-oxide fuel cell systems. Adv Chem Eng 2012;41:383–446.
[11] Huang B, Qi Y, Murshed M. Solid oxide fuel cell Perspective of dynamic modeling and control. J Process Control 2011;21(10):1426–37.
[12] Mangold M, Krasnyk M, Sundmacher K. Nonlinear analysis of current instabilities in high temperature fuel cells. Chem Eng Sci 2004;59:4869–77.
[13] Fardadi M, Mueller F, Jabbari F. Feedback control of solid oxide fuel cell spatial temperature variation. J Power Sources 2010;195(13):4222–33.
[14] Serincan MF, Pasaogullari U, Sammes NM. A transient analysis of a micro tubular solid oxide fuel cell (SOFC). J Power Sources 2009;194:864–72.
[15] Zhang L, Li X, Jiang J, Li S, Yang J, Li J. Review: dynamic modeling and analysis of a 5-kW solid oxide fuel cell system from the perspectives of cooperative control of thermal safety and high efficiency. Int J Hydrogen Energy 2015;40:456–76.
[16] Li J, Cao GY, Zhu XJ, Tu YH. Two-dimensional dynamic simulation of a direct internal reforming solid oxide fuel cell. J Power Sources 2007;171:585–600.
[17] Maharudrayya S, Jayanti S, Deshpande AP. Pressure losses in laminar flow through serpentine channels in fuel cell stacks. J Power Sources 2004;138:1–13.
[18] Mahcene H, Moussa HB, Bouguettaia H, Bechki D, Babay S, Meftah MS. Study of species, temperature distributions and the solid oxide fuel cells performance in a 2-D model. Int J Hydrogen Energy 2011;36:4244–52.
[19] Al-Masri A, Peksen M, Blum L, Stolten D. A 3D CFD model for predicting the temperature distribution in a full scale APU SOFC short stack under transient operating conditions. Appl Energy 2014;135:539–47.
[20] Ho Thinh X. Dynamic characteristics of a solid oxide fuel cell with direct internal reforming of methane. Energy Convers Manage 2016;113:44–51.
[21] Huangfu Y, Gao F, Abbas-Turki A, Bouquain D, Miraoui A. Transient dynamic and modeling parameter sensitivity analysis of 1D solid oxide fuel cell model. Energy Convers Manage 2013;71:172–85.
[22] Gemmen RS. Dynamic modeling of fuel cells. In: Bove R, Ubertini S, editors. Model Solid Oxide Fuel Cells. Springer; 2008 [Chapter 9].
[23] Bhattacharyya D, Rengaswamy R. A review of solid oxide fuel cell (SOFC) dynamic models. Ind Eng Chem Res 2009;48:6068–86.
[24] Ferrari ML. Solid oxide fuel cell hybrid system: control strategy for stand-alone configurations. J Power Sources 2011;196:2682–90.
[25] Stiller C, Thoruda B, Bolland O, Kandepu R, Lars Imsland L. Control strategy for a solid oxide fuel cell and gas turbine hybrid system. J Power Sources 2006;158:303–15.
[26] Jia Z, Sun J, Oh S-R, Dobbs H, King J. Control of the dual mode operation of generator/motor in SOFC/GT-based APU for extended dynamic capabilities. J Power Sources 2013;235:172–80.
[27] Ferrari ML. Advanced control approach for hybrid systems based on solid oxide fuel cells. Appl Energy 2015;145:364–73.
[28] Aguiar P, Adjiman CS, Brandon NP. Anode-supported intermediate temperature direct internal reforming solid oxide fuel cell II. Model-based dynamic performance and control. J Power Sources 2005;147:136–47.
[29] Sorrentino M, Pianese C. Model-based development of low-level control strategies for transient operation of solid oxide fuel cell systems. J Power Sources 2011;196:9036–45.
[30] Pohjoranta A, Halinen M, Pennanen J, Kiviaho J. Model predictive control of the solid oxide fuel cell stack temperature with models based on experimental data. J Power Sources 2015;277:239–50.
[31] Vijay P, Hosseini S, Tadé MO. A novel concept for improved thermal management of the planar SOFC. Chem Eng Res Des 2013;91:560–72.
[32] Jiang J, Li X, Li J. Modeling and model-based analysis of a solid oxide fuel cell thermal-electrical management system with an air bypass valve. Electrochim Acta 2015;177:250–63.
[33] Penchini D, Cinti G, Discepoli G, Sisani E, Desideri U. Characterization of a 100 W SOFC stack fed by carbon monoxide rich fuels. Int J Hydrogen Energy 2013;38:525–31.

Coupling Solid Oxide Electrolyser (SOE) and ammonia production plant

CrossMark
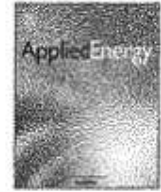
Giovanni Cinti [a,*], Domenico Frattini [b], Elio Jannelli [b], Umberto Desideri [c], Gianni Bidini [a]

[a] Università degli Studi di Perugia, via Duranti 93, 06125 Perugia, Italy
[b] Università degli Studi di Napoli Parthenope, Centro Direzionale Napoli Isola C4, 80143 Naples, Italy
[c] Università degli Studi di Pisa, Largo Lucio Lazzarino, 56122 Pisa, Italy

HIGHLIGHTS

- An innovative NH_3 production plant was designed.
- CO_2 emissions and energy consumption are studied in three different designs.
- High temperature electrolysis allows to achieve high efficiency and heat recovery.
- The coupling permits storage of electricity into a liquid carbon free chemical.

ARTICLE INFO

ABSTRACT

Ammonia is one of the most produced chemicals worldwide and is currently synthesized using nitrogen separated from air and hydrogen from natural gas reforming with consequent high consumption of fossil fuel and high emission of CO_2. A renewable path for ammonia production is desirable considering the potential development of ammonia as energy carrier. This study reports design and analysis of an innovative system for the production of green ammonia using electricity from renewable energy sources. This concept couples Solid Oxide Electrolysis (SOE), for the production of hydrogen, with an improved Haber Bosch Reactor (HBR), for ammonia synthesis. An air separator is also introduced to supply pure nitrogen. SOE operates with extremely high efficiency recovering high temperature heat from the Haber-Bosch reactor. Aspen was used to develop a model to study the performance of the plant. Both the SOE and the HBR operate at 650 °C. Ammonia production with zero emission of CO_2 can be obtained with a reduction of 40% of power input compared to equivalent plants.

© 2016 Elsevier Ltd. All rights reserved.

1. Introduction

Ammonia was presented recently as a potential fuel and as an eligible energy vector [1]. Such opportunity comes from ammonia high energy density. Volumetric and gravimetric energy density of ammonia at room temperature and 10 bar are 22.5 MJ/kg and 13.6 GJ/m^3 respectively, higher than other candidates such as hydrogen and methanol and not far from fossil sources such as gasoline, diesel and compressed natural gas. The utilization of ammonia as a fuel was reported with interesting results in traditional power units [2,3]. Ammonia combustion releases heat that can be used in both internal and external combustion engines [4]. In addition, the use of ammonia as a fuel is also demonstrated in fuel cells with consequent advantages in terms of low emissions and high efficiency. Ammonia is a carbon free fuel, no CO_2 is

emitted when burnt, and in fuel cell applications the risk of NO_x emissions is reduced because no direct mix between oxygen and ammonia occurs. A sustainable use of ammonia both as a chemical and as a fuel requires a renewable production of nitrogen and hydrogen [5,6]. Ammonia is usually produced in the Haber-Bosch (HB) loop reactor from pure hydrogen and nitrogen that are fed and recirculated in the reactor, operating at high pressure and high temperature. Hydrogen is commercially produced from fossil sources, such as natural gas, normally in an autothermal steam methane reformer or in a steam methane reformer, while nitrogen is separated from air. In order to call ammonia a green chemical, both hydrogen and nitrogen should be produced and supplied using renewable energy as a primary source: biomass [7], wind [8] or solar energy [9] can guarantee a renewable and sustainable production of ammonia based on thermochemical or electrochemical processes [10]. In particular, from water electrolysis and air separation powered by renewable electricity it is possible to produce green ammonia without any CO_2 emission to the atmosphere [11].

* Corresponding author.
E-mail address: giovanni.cinti@unipg.it (G. Cinti).

This kind of plant can also be used in electric grids with a large penetration of intermittent renewable energy sources to store energy into a liquid fuel that allows the spatial and temporal separation, of energy supply and demand. The green ammonia plant allows to store directly the renewable electricity into a chemical with high energy density, quite easy to stock and to transport. This concept was recently presented and studied in the literature [12,13]. An additional advantage of the proposed concept is that compared to the storage of renewable electricity into fuels such as methane, methanol or synthetic diesel; ammonia production does not require carbon dioxide but nitrogen as additional gas input. Both nitrogen and carbon dioxide can be separated from the air but the higher concentration of nitrogen increases efficiency and lowers production cost in comparison with CO_2.

Recent developments of Solid Oxide Fuel Cells (SOFCs) renewed interest in high temperature Solid Oxide Electrolysers (SOEs), based on the same materials and design [14]. SOEs operate with higher power density and higher efficiency compared to traditional electrolysers, especially if fed with high temperature waste heat, because the electrochemical conversion of water at high temperatures opens the opportunity to store both heat and electricity in the produced hydrogen [15]. Such opportunity is currently under study in industrial processes where waste heat recovery at high temperature is available. For example, coupling is possible with nuclear power plants where heat is usually a by-product [16], or with solar collectors in solar thermal power plants, where renewable heat comes from the sun [17] in order to achieve energy storage or production of secondary fuels or energy vectors [18]. In this scenario, the coupling of SOE and HB process is extremely interesting. NH_3 synthesis is an exothermal chemical reaction at high temperature and pressure, producing a large amount of heat. The integration between the HB process and the SOE potentially allows to transfer the heat produced by the HB reactor to the SOE to increase its performance. Moreover, the feasibility of ammonia production from renewable energy via electrolysis of water is very important to produce sustainable fuels and chemicals.

This study proposes an improvement to green ammonia production plants introducing, for the first time, an SOE for H_2 production in a HB process. In addition to the studies already cited above literature reports, for example, system designs based on wind power with a small efficiency and a limited degree of integration [19]. The new concept proposed in this work permits system implementation and allows to improve the power to ammonia storage efficiency. An electrochemical model and a thermodynamic simulation of a system layout, in which an SOE and an NH_3 plant are integrated and operated at high pressure and temperature, has been developed to evaluate the potential of the proposed concept with respect to other green solutions and to a reference benchmark case, based on the use of natural gas. The effect on the global efficiency and on avoided CO_2 emissions is evaluated. This work can enhance the development of green ammonia and can offer, at the same time, an interesting application of SOE, pushing the development and application of the technology not only in the energy sector but also in the chemicals production field. In the following paragraphs the theory and modelling of SOE and HB process are presented, the design of the model is described and, finally, the main results are analysed and commented.

2. Theoretical background and model development

2.1. Considerations for coupling and SOE electrochemical model

Ammonia synthesis is realized mainly with the plant design developed by Haber and Bosch (HB). The HB process considered in this work is based on a modern layout, as shown in Fig. 1.

Ammonia synthesis is an exothermal process based on the following chemical reaction:

$$\frac{3}{2}H_2 + \frac{1}{2}N_2 \leftrightarrow NH_3 \quad \Delta H^\circ = -45.7 \text{ kJ/mol } H_2 \quad (1)$$
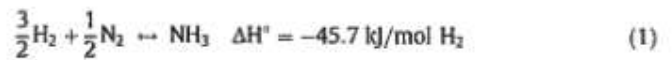
The distinctive physical aspects of this equilibrium reaction is the contrasting effect of pressure and temperature on thermodynamics and kinetics, according to the following equation [20]:

$$K_{NH_3} = K_\varphi \cdot K_p = \left(\frac{\varphi_{NH_3}}{\varphi_{N_2}^{1/2} \cdot \varphi_{H_2}^{3/2}} \right) \cdot \left(\frac{n_{NH_3}}{n_{N_2}^{1/2} \cdot n_{H_2}^{3/2}} \cdot \frac{n_{tot}}{P_{tot}} \right) \quad (2)$$

The left hand side is the chemical equilibrium constant in which non ideal fugacity coefficients are accounted in the term K_φ. The term K_p account for the reactor operating conditions, especially the presence of inert species, which can decrease the molar fraction of reactants and so the production of ammonia. On the other hand, as the total pressure increases, also the conversion of reagents into ammonia increases. The reaction kinetic is governed by the Temkin-Pyzhev equations [21] in which the reaction rate of the reverse process is negligible as the reactor temperature increases, but, due to the exothermal characteristic of the thermodynamic equilibrium, the chemical equilibrium constant is lower. Ammonia synthesis is realized mainly with the plant design developed by Haber and Bosch (HB). The HB process considered in this work is based on a modern layout, as shown in Fig. 1. The main features, according to the above thermodynamic and kinetic considerations, are the recycle streams, two stages of ammonia separation (before and after each reactor passage) and heat recovery from products to increase productivity and reduce energy requirements. As a consequence, an efficient and high conversion of reactants in the HB reactor is favored by:

- High pressure and temperature of the reactor.
- Stoichiometric H_2/N_2 ratio in the reactor feeding stream.
- Absence of inerts or diluting species.
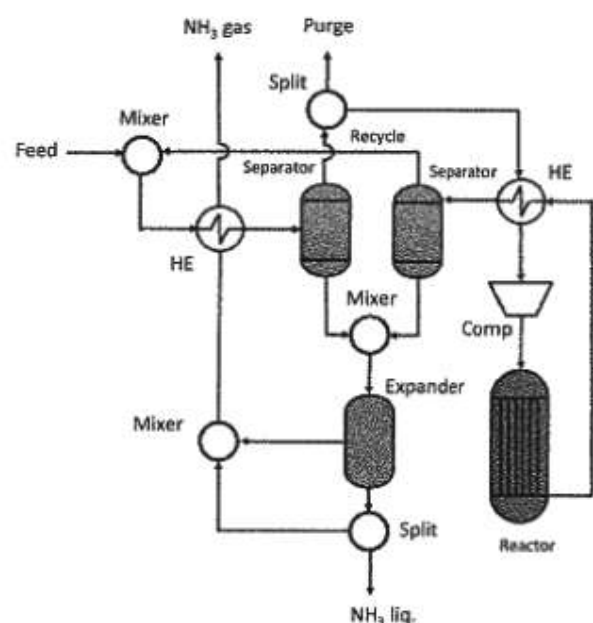- Auxiliary streams for purging inerts and for recirculation of unconverted gasses.

Fig. 1. HB process layout for production of NH_3.

From the physical point of view, the first two points determine the conversion per single pass in the HB reactor and, according to thermodynamics, an isothermal reactor should be preferred, with an efficient reaction heat recovery system, which is the major source of waste heat. The last two points mainly contribute to the global conversion and productivity of the plant. In fact, a feeding stream with a low content of inerts limits the need to partially purge unreacted gases, reduces the hydrogen losses in the tail gas, increases the recycle ratio in the HB loop as more ammonia can be produced and separated at each pass and the global conversion efficiency increases. Other relevant processes that affect the HB plant are syngas production and purification. Steam Methane Reforming (SMR) and Water Gas Shift (WGS) are the main processes involved in syngas production while physical and chemical separation processes, based on condensation, membranes and absorption at low temperatures, are used to purify syngas from species such as H_2O, CO, CO_2 and CH_4 [22]. On the other hand, electricity-based processes for H_2/N_2 production, such as electrolysis, cryogenic air separation and Pressure Swing Adsorption (PSA) [23] can be considered for syngas production as they involve low temperatures and mild thermodynamic conditions. So, from the thermodynamic point of view, exothermal and endothermal processes are simultaneously involved and, considering the presence of high and low temperature units, heat recovery issues arise in order to optimize the system design and process integration as these aspects influence the energy efficiency and the production of the overall plant. In this background, it is clear that a proper integration between different technologies to improve the HB process requires an overall system evaluation in order to verify benefits and drawbacks of each solution.

SOE conceptual scheme is depicted in Fig. 2.

Anodic and cathodic reactions are:

Anode $\quad O^{2-} \rightarrow 2e^- + \frac{1}{2}O_2$ (3)

Cathode $\quad H_2O + 2e^- \rightarrow H_2 + O^{2-}$ (4)
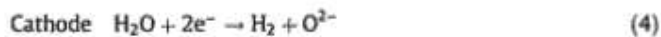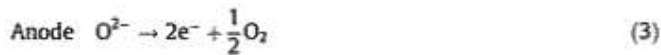
The overall electrolysis reaction is the following:

$H_2O \leftrightarrow H_2 + \frac{1}{2}O_2$ (5)

The reaction is endothermal and the enthalpy change has to be supplied externally. In electrochemical devices, such as fuel cells, energy is supplied as electrical (ΔG) and thermal energy ($T\Delta S$). Thermal energy is usually generated inside the cell, recovering heat from internal polarization losses. With the increase of temperature, total energy requirement (ΔH) increases but the amount of electrical energy is smaller. The result is a higher efficiency of the high temperature electrolyser than the low temperature ones. If part of the necessary heat is supplied by an external source, it is possible to achieve higher than one efficiency, obtaining the conversion of thermal energy into chemicals.

Thermodynamic values at 650 °C are reported in Table 1. Note that values are normalized for one mole of H_2 produced (electrolysis) or reacting (ammonia synthesis).
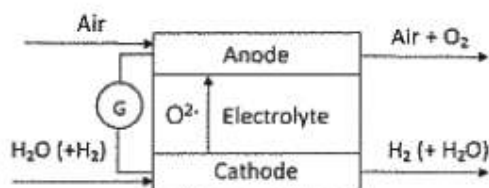

Fig. 2. SOE conceptual scheme.

Ammonia synthesis can supply up to 98% (39.14 kJ/mol H_2) of the heat required, in terms of entropy, of the electrolysis reaction (39.66 kJ/mol H_2). In order to couple thermodynamic and electrochemical calculations for integration with the HB process, a zero dimension model for the SOE was developed as follows.

In an SOE, the electrical inputs creates the electron flows involved in the reactions. In electrolysers, voltage is a function of current density and can be described with a very simple linear law as follows:

$V = OCV + ASR(T) * J$ (6)

Were OCV is the Open Circuit Voltage, ASR is Area Specific Resistance and J is current density. Both OCV and ASR are function of temperature. This simplified approach is supported by experimental results that show how the polarization curve is highly linear at high temperature [24]. In additions authors already demonstrated how ASR does not change between SOFC and SOE operation [25]. This assumption will be used in defining values of ASR. In the following equation (iv) SOE electrical power density is described as follows:

$P_e = V * J = OCVJ + ASR * J^2$ (7)

Energy output of the SOE is the energy of produced hydrogen. Such energy is the chemical energy of the fuel usually quantified in the LHV. For this study such energy was considered the enthalpy of the reaction (1) equivalent to the LHV of the fuel. Differently from LHV, the calculation was performed at the operational temperature. Specific chemical energy (in terms of energy flow per unit area) converted in the SOE is defined as follows:

$\Delta H = dh(T) * H_{2mol}$ (8)

where H_{2mol} is the specific molar flow (mol/m^2) of hydrogen and dh (T) is the enthalpy of the reaction (1). Hydrogen specific flow and current density are connected to the electrochemical parameters by the equation:

$H_{2mol} = \frac{J}{2 * F}$ (9)

where F is the Faraday constant. Differently from fuel cells, the chemical reaction in electrolysers is endothermal and the heat losses of the process, such as overpotential losses, are in equilibrium with reaction requirements. The energy balance is completed by the contribution of heat transfer with the external source. The latter takes into account the SOE heat losses into the environment and the heat inlet from the environment that may come from a high temperature heat source, as in this application. External heat (Q) is calculated, for the present study, as a function of hydrogen energy production by the following equation

$Q = k * \Delta H$ (10)

The energy balance of the SOE is defined by the following equation:

$P_e = \Delta H + Q = \Delta H(1 + k)$ (11)

Differently from fuel cells, were produced heat has to be subtracted by the air flow, in SOEs the external heat contribution plays an important role not only on the operational temperature but also on the performance. Assuming the stack at constant temperature, Eq. (12) directly relates current density and temperature to the external heat. Thus, temperature definition and k allow to calculate the current density. Considering the previous equations J can be calculated as:

$J = \frac{1}{ASR}\left(\frac{dh(T) * (1 + k)}{2 * F} - OCV\right)$ (12)

Efficiency is calculated as the ration between energy output (ΔH) and energy input (P_e) by the following equation:

	Temperature [°C]	Pressure [bar]	ΔH [kJ/mol H₂]	TΔS [kJ/mol H₂]	ΔG [kJ/mol H₂]
Water electrolysis	650	1	247.32	39.66	207.65
Ammonia synthesis	650	550	−39.14	−83.68	44.54

$$\eta = \frac{\Delta H}{P_e} = \frac{1}{1+k} \tag{13}$$

Note that the efficiency is only a function of external heat contribution (k). In the specific case of k = 0 the SOE operates in adiabatic conditions (no heat exchange with the environment) with a 100% theoretical efficiency. This operational condition is called thermoneutral. All equations were implemented in a zero-dimensional model developed using Excel and FluidProp© as cathode for thermodynamic parameters. The OCV value was calculated using the well-known Nernst equation considering at cathode inlet a steam flow with 10% hydrogen (necessary for the integrity of the electrode) and at anode inlet air. ASR values are derived from a SOFC commercial product [17] due to the aforementioned equivalence with SOE ones.

2.2. Description of developed case studies

In order to assess the profitability of coupling SOE and HB process for the production of green ammonia, Process Flow Diagrams (PFDs) were realized in the AspenPlus environment to compare different scenarios. In particular, three case studies were developed. A brief description of the relevant process physics of each developed layout is given below. More details about the flowsheets and the specific parameters used to model the single blocks in AspenPlus are given in Appendix A. Considering the high temperature and high pressure conditions for the HB loop, no kinetic approaches are applied for simulations and only the thermodynamic equilibrium is considered.

The plant layout for the reference case, named NG-REF-HB, with conventional NH₃ production from natural gas is shown in Fig. 3.

In this plant the upstream process is the CH₄ steam reforming, where many units are required for the clean-up of the reformed gas in order to obtain a feed stream for the ammonia production with the appropriate composition. In fact, the reforming process is endothermal and requires a large amount of heat. The first burner is adiabatic and the amount of oxygen introduced is not sufficient to oxidize all the fuel and a partial gasification occurs with H₂ and CO formed together with CO₂ with the aim to partially provide the necessary heat for reforming and H₂ for the synthesis. In the subsequent WGS section, CO reacts with steam to produce H₂, thus increasing hydrogen content in the syngas for ammonia production. The Acid Gas Removal unit (AGR), the Methanator unit (METH) and the Condenser (COND) are devoted to the physical and chemical separation and removal of CO₂, CO and H₂O after the WGS section. These processes require a much lower temperature (50–100 °C) than that of WGS (250–550 °C). The waste heat available is recovered to produce the high temperature steam for the reforming unit. From the thermodynamic point of view, the operating conditions of these units must be accurately chosen in order to correctly simulate the physics of the process.

In Fig. 4 the low temperature electrolysis case, named EL-PSA-HB, with H₂ produced from commercial electrolysers and N₂ produced by PSA, is shown.

This layout is completely different from the previous one. The feeding streams to the plant are air and water, at ambient condition, as primary sources for H₂ and N₂. From the physical point of view, the principal characteristic of this solution is that no chemical energy, as fuel, is introduced and the only energy input

is electricity, thus the thermodynamic of the process does not involve high temperatures, pressures or large heat exchangers. In agreement with the actual water electrolysers performance, a hydrogen purity of 99.9% and an electrical efficiency of 64.4% have been specified for this block [26]. The air separation unit is based on a PSA standard process at room temperature and 30 bar, with commercial carbon molecular sieves as adsorbent [27].

Finally, the case of SOE and HB with heat recovery from the synthesis reactor, SOE-PSA-HB, is shown in Fig. 5.

From the thermodynamic point of view, the main difference with the previous case is that the low temperature electrolysis is replaced by the high temperature one. The physics of the upstream section, representing the SOE unit, has been already discussed in previous works [28] and slightly modified as specified in Appendix A. Briefly, the main modifications for thermodynamic reasons concern the operating temperature and the thermal input of SOE that matches the conditions imposed by the HB reactor. This ties the coupling task to the energy balance and thermodynamic equilibrium of the overall system.

3. Results and discussion

Fig. 6 reports the variation of hydrogen production rate and efficiency (a) and of electrical power input and voltage (b) as a function of temperature for three values of k: k = 0 (thermoneutral), k = 0.2 (heat into the SOE) and k = −0.2 (heat losses). Fig. 6a shows a trade-off between efficiency and hydrogen production: with higher values of k smaller efficiency can be obtained. As expected from Eq. (13), efficiency is not affected by temperature variation while hydrogen production increases with temperature due to the decrease of internal resistances (ASR). Regarding Fig. 6b, the electrical power density increases with temperature and is higher when k is smaller (heat losses). Cell voltage remains constant at current density variation while it increases when k decreases. Thermoneutral voltage obtained is approximately 1.29 V in agreement with the literature [14].

Considering the coupling of ammonia synthesis with SOE, it is possible to calculate the k factor, considering the heat flow from the ammonia reactor calculated from the Aspen model. At the operating temperature of 650 °C all other SOE parameters are calculated and reported in Table 2.

In order to compare the performance of the different cases considered, the following Table 3 shows the major comparative parameters for the three scenarios. They refer only to the HB loop subsection of the flowsheets.

The global efficiency η_glob is based on the overall H₂ molar balance around the flowsheet as it takes into consideration the chemical conversion of hydrogen and also the separation of the unreacted moles for the internal recycle. On the other hand, the reactor efficiency η_react represents the conversion of H₂ per pass on molar basis inside the block REACTOR as it depends on the inlet molar composition and the operating condition of the HB loop. Comparing the values, remarkable differences are visible between the reference case, i.e. NG-REF-HB, and the remaining two, while the results obtained for the two cases with the use of electrolysers seem to be very similar. The first two plants, the first fed with natural gas and the second based on a low temperature standard electrolyser, can be operated at middle HB reactor conditions (250 bar
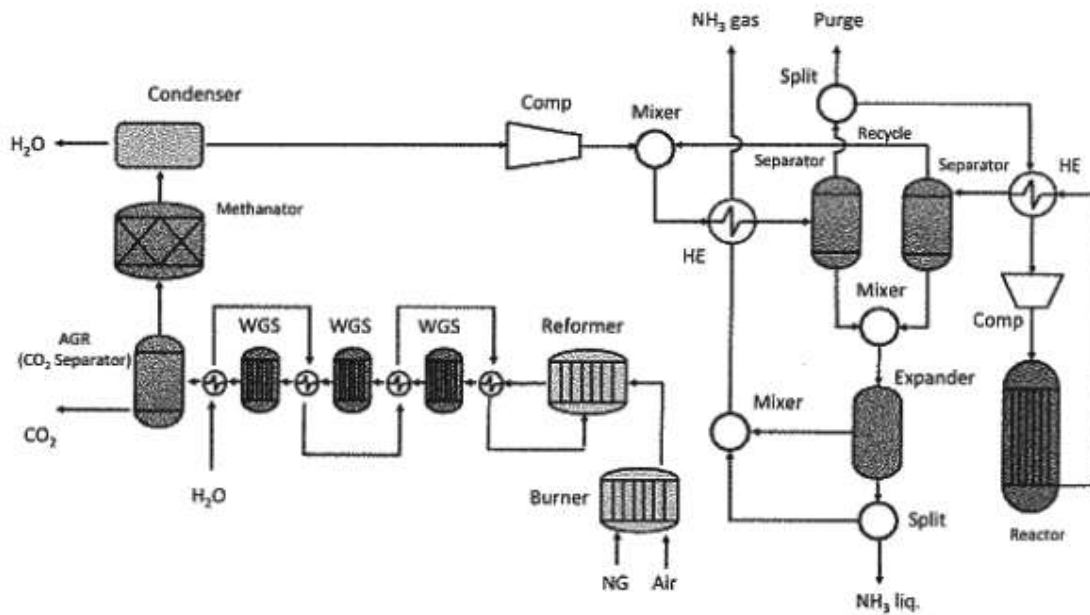
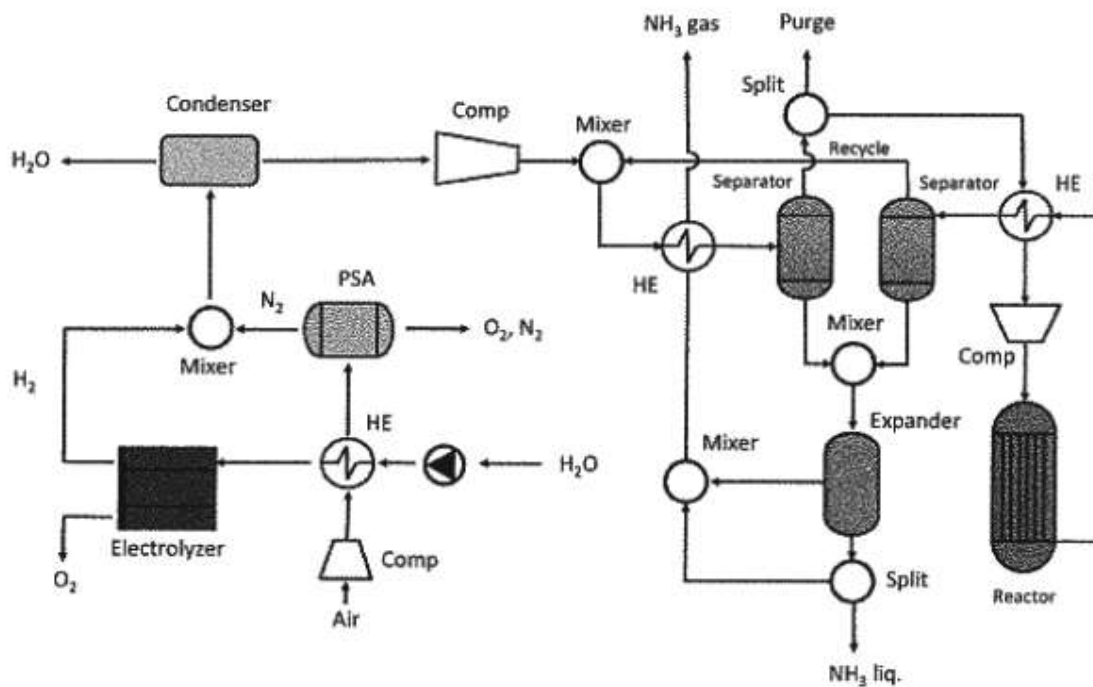Fig. 3. Layout of the reference case NG-REF-HB.

Fig. 4. Layout of the low temperature electrolysis case EL-PSA-HB.

and 550 °C). SOE necessarily requires heavy HB reactor conditions (550 bar and 650 °C) for coupling, as discussed in Section 2.1. Contrarily to what could be expected, the conversion per pass and the global efficiency is very different for NG-REF-HB and EL-PSA-HB, even if temperature and pressure of the HB reactor are the same. This is due to the high content of inerts in the reference case, i.e. CH_4, that dilutes the reactant steam and affects negatively the K_p term as envisaged from Eq. (2). Moreover, the dilution of the products by CH_4 affects the physical separation of ammonia because it

reduces the partial pressure of NH_3 in SEP01 and SEP02 blocks. This is the cause of the low η_{glob} and the deviation of the H_2/N_2 ratio inside the HB loop. As a consequence, the resulting purge ratio, i.e. the purge gas stream, should be higher in order to avoid the accumulation of inerts in the loop. On the contrary, the two cases with electrolysers have very similar HB loop performances due to the complete absence of inerts. This is a distinguishing feature of ammonia production when electrolysis and air separation are used to provide the H_2/N_2 mixture. In particular, the purge ratio is very
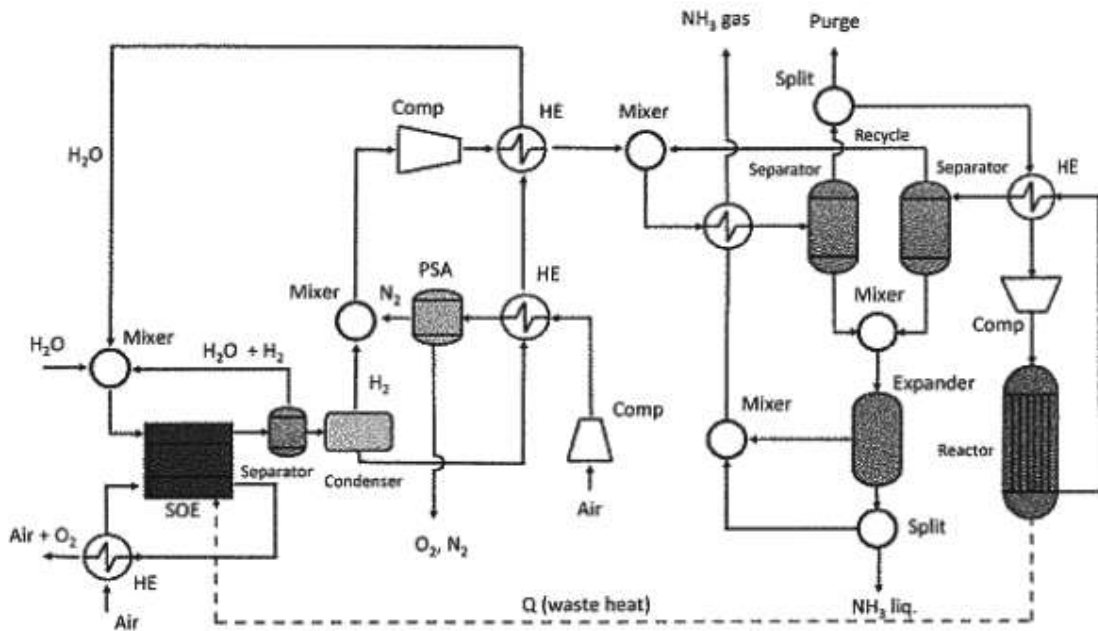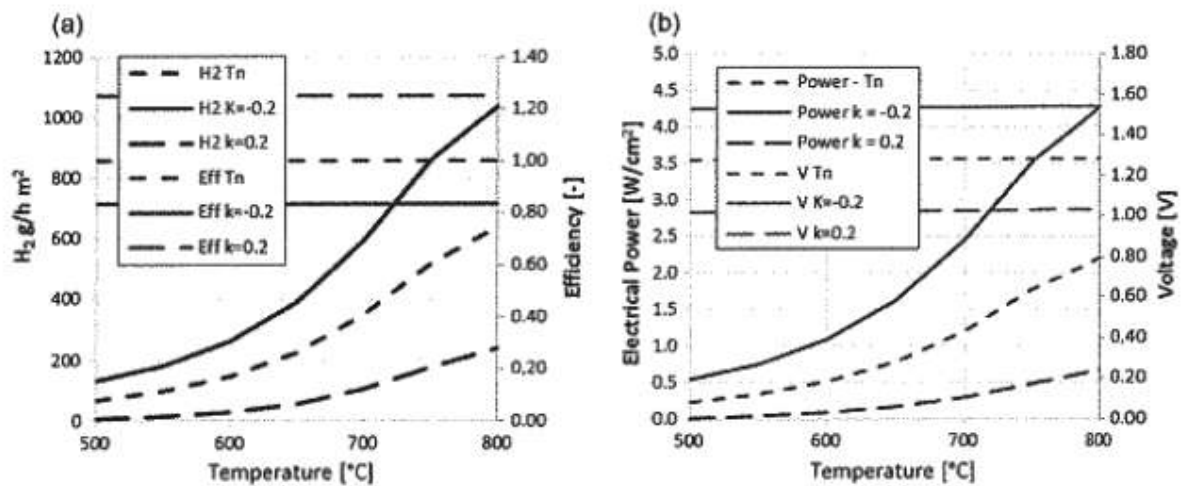
Fig. 5. Layout of the high temperature electrolysis case SOE-PSA-HB.

Fig. 6. Effect of temperature and k (a) hydrogen production rate and efficiency; (b) electrical power and voltage.

Table 2
SOE parameter when integrated with NH₃ synthesis.

Parameter	Units	Value
k	–	0.15
Temperature	°C	650
ASR	$\Omega\cdot cm^2$	0.57
OCV	V	0.94
H₂	g/h·m²	102.56
J	A/cm²	0.27
Voltage	V	1.09
Power density	W/cm²	0.35
η	–	1.17

In Table 4 the overall energy consumptions and the equivalent Greenhouse Gas (GHG) emissions of the three cases are reported. The equations used for calculations are the following:

$$Spec.\,Chem.\,Cons. = \frac{\sum \dot{n}_i \cdot LHV_i}{\dot{m}_{NH3}^{TOT}} \tag{14}$$

$$Spec.\,Elec.\,Cons. = \frac{\sum P_j^{el}}{\dot{m}_{NH3}^{TOT}} \tag{15}$$

$$Spec.\,Heat\,Cons. = \frac{\sum P_j^{th}}{\dot{m}_{NH3}^{TOT}} \tag{16}$$

$$GHG\,Emissions = \frac{(\dot{n}_{CO} + \dot{n}_{CO2} + \dot{n}_{CH4}) \cdot M_{CO2}}{\dot{m}_{NH3}^{TOT}} \tag{17}$$

small, so that more reactants can be recycled to the reactor instead of being purged with inerts. As a consequence, the recycle ratio, the NH₃ produced and the global efficiency increase.

Table 3
HB loop performances for the three different case studies.

	$(H_2/N_2)_{FEED}$ (mol/mol)	$(H_2/N_2)_{IN}$ (mol/mol)	Rec. ratio (mol/mol)	Purge ratio (mol/mol)	LHV_{PURGE} (MJ/kg)	η_{glob} (%)	η_{react} (%)
NG-REF-HB	3.07	3.17	3.33	0.44	26.76	61.12	18.25
EL-PSA-HB	3.01	3.02	4.29	0.08	21.35	92.33	21.06
SOE-PSA-HB	3.00	3.03	4.30	0.06	21.43	93.40	19.53

Table 4
Energy performances for the three different case studies.

	Spec. chem. cons. (kW h/kg_{NH3})	Spec. elec. cons. (kW h$_{el}$/kg_{NH3})	Spec. tot. cons. (kW h/kg_{NH3})	Spec. heat cons. (kW h$_{th}$/kg_{NH3})	GHG emissions (kg_{CO2eq}/kg_{NH3})	Storage eff. (%)
NG-REF-HB	12.81	1.77	14.59	−1.20	2.05	35.50
EL-PSA-HB	0	14.25	14.25	−1.63	0	36.35
SOE-PSA-HB	0	8.30	8.30	−1.14	0	62.41

$$Storage\,Eff. = \frac{\dot{m}_{NH3}^{TOT} \cdot LHV_{NH3}}{\sum \dot{n}_i \cdot LHV_i + \sum P_j^{el}} \cdot 100 \qquad (18)$$

where $\sum \dot{n}_i \cdot LHV_i$ is the total chemical energy entering the flowsheet, $\sum P_j^{el}$ is the sum of all the electric power and $\sum P_j^{th}$ is the sum of all the heat flux of the generic block j in the flowsheet. The specific total consumption is the sum of the values calculated from Eqs. (14) and (15). They are all normalized on $\dot{m}_{NH3}^{TOT}$, i.e. the total quantity of ammonia produced, considering both liquid and gaseous ammonia in output streams. As reference, positive values are intended as energy provided to the system, while negative values represent energy that should be subtracted from the system.

The first evident results is that for the case EL-PSA-HB and SOE-PSA-HB the specific chemical consumption is zero: these systems are fed only by air and water so that there is no energy cost. On the contrary, the NG-REF-HB uses a fuel, i.e. CH$_4$, as feedstock. As expected, only the first case has a net environmental impact in terms of GHG emissions due to the CO$_2$ release during the reforming and clean-up operations of the fuel. This is mainly concentrated

in the AGR block of the flowsheet in Fig. 3, because it is one of the units devoted to the removal of oxygenated species from the syngas for NH$_3$ synthesis. The remaining two cases have no net emissions because their feedstock is "carbon-free". The purge gas of the NG-REF-HB contains CH$_4$, which is a greenhouse gas, but the emission related to this gas is not accounted to the plant due to the fact that this stream can be stored as a secondary fuel or as a chemical feedstock for other purposes. Moreover, keeping in mind the previous purge ratios and global efficiencies, it can be concluded that the quantity of purge gas produced is considerable in the first system but negligible in the other two. Finally, a significant difference on the total and heat consumptions occurs in all cases. In particular, even though the HB loop performances are quite the same, the cases with electrolyser have very different consumptions. Comparing the reference case and the standard electrolyser case, it is worth to observe that the total consumption is not so different, so that there is a little benefit in preferring the electrolysis pathway, power-intensive but low impacting, rather than the traditional one, based on fossil fuel and less electricity-consuming with the perspective to produce a valuable tail gas. However, the
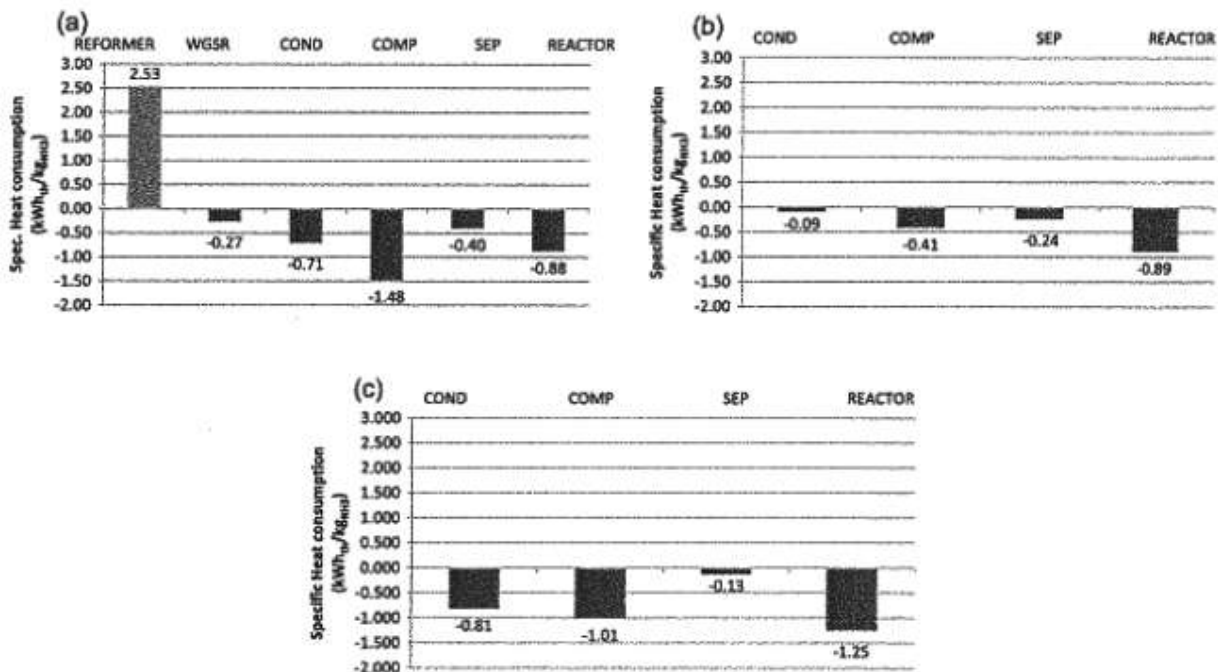
Fig. 7. Specific heat consumption of ancillaries: (a) NG-REF-HB; (b) EL-PSA-HB; (c) SOE-PSA-HB.

results show that in the case of coupling SOE, PSA and HB, the total energy consumption can be potentially lower than all other proposed solutions. In addition, considering the perspective of the storage of electricity into a chemical vector, i.e. NH₃, the calculation shows that the SOE-HB coupling has a potential storage efficiency of 62.4% and that it is almost two times higher than EL-PSA-HB and NG-REF-HB cases. The advantage of using high efficiency and high temperature electrolysis in a SOE is thus evident and integrated in a conventional chemical process like ammonia production.

To better understand this, in Fig. 7, the detailed consumption of heat is specified for the main ancillaries of the three developed scenarios. For the reference case, which has more ancillaries than the other cases, there is a considerable endothermal term, due to the heat required by the reformer block, and a higher exothermal contribution from the compression units, due to the intercooling.

The other two cases have smaller contributions, due to the simpler layout with no fuel thermal treatments or gas clean-up units. Comparing Figs. 7a and b, the heat available from HB reactor is the same because the operating conditions are the same but, due to the presence of a large amount of inerts, the amount of heat that should be removed from COMP is larger. The presence of species other than H_2, N_2 and NH_3 in the HB loop is a strong limit for productivity but also energy efficiency of traditional HB plant because, if compared to the contribution of an electrolysis-based plant, they cause lower conversion and larger amounts of waste heat. From this point of view, the SOE-PSA-HB offers more flexibility and opportunity for a convenient recovery of waste heat. In Fig. 7c not all the contributions reported are really lost because, as shown

by the flowsheet of Fig. A4 in appendix, the heat from COND and REACTOR are used to achieve the thermal equilibrium of the SOE block because this acts as a "heat sink" for the system. In detail, the heat from REACTOR is entirely used to feed SOE and is an input for the design of the electrolyser. Compared to low temperature electrolysis steam is supplied to SOE instead of water. The amount of energy to vaporize water, 1.79 kW h/kg$_{NH3}$ can be recovered partially from the compressor, where 1.01 kW h/kg$_{NH3}$ are released from intercoolers, and from condenser, where 0.81 kW h/kg$_{NH3}$ are released at high temperature. An additional advantage of this configuration is that no cooling of ammonia reactor is required reducing the environmental impact in terms of plant waste heat. One of the actual issue for SOE is that it requires a large amount of heat, or a high current density, from external sources to sustain the high temperature electrolysis process. If SOE and HB loop can be operated at similar temperatures, their coupling offer the opportunity to recover the large amount of heat available from HB reactor to achieve a stable thermal equilibrium in the SOE, without increasing the current density, i.e. the electricity consumption, as explained in the model above. The single contributions of COND and REACTOR in the SOE-PSA-HB case are reported for completeness and to show how they become of interest if compared to that of the mild HB reactor conditions.

The direct consequence of this fact can be immediately realized if the single electric consumptions are compared as shown in Fig. 8.

The first two columns clearly show the advantage of the high temperature electrolysis over the low temperature one, if additional heat is provided from another source. The consumptions related to the PSA subsection are the same for both cases, as expected, while the electric consumptions related to the compression units of the HB loop are very different, essentially due to the high pressure imposed at the REACTOR block of the SOE-PSA-HB. It is worth noting that for the reference case the electric consumption is represented only by the compression units in the HB loop, and that its value is 1.77 kW h/kg$_{NH3}$, the highest among the three scenarios, because a large part of this energy is used to compress inerts which dilutes the syngas stream.

The coupling of SOE and HB deeply affects the energy balance of the plant when the electrolysis is used in place of the reforming of a fossil fuel. Moreover, the type of electrolysis process modifies the distribution of energy consumption within the plant itself. The situation is briefly explained in Fig. 9.

When a low temperature electrolysis is used to produce the syngas for the HB loop, the electric consumption related to the electrolyser operation is >95% of the total, i.e. the overall energy balance is in practice restricted to the electrolyser, so that there is no flexibility and the whole plant is dependent from the electrol-
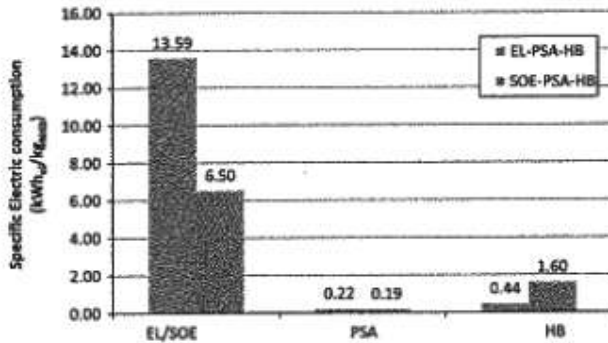

Fig. 8. Comparison of the electric consumption for EL-PSA-HB and SOE-PSA-HB cases.
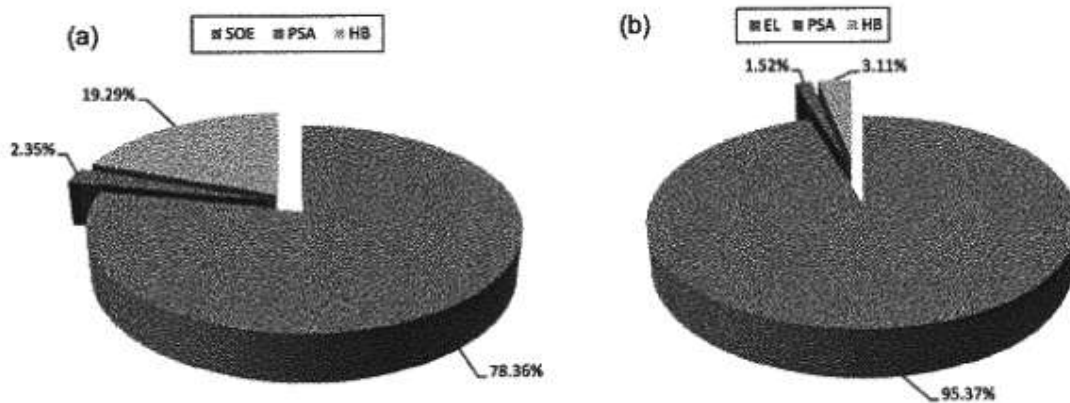

Fig. 9. Distribution of the specific electric consumption: (a) EL-PSA-HB; (b) SOE-PSA-HB.

ysis subsection. On the other hand, when a SOE is implemented, its impact on the overall energy balance is lower, as shown in Fig. 9b: the share for the electrolysis subsection decreases from 95.37% to 78.36%.

4. Conclusions

A novel system for the production of green ammonia was designed and analysed. The introduction of high temperature electrolyser, such as SOE, permits to increase efficiency and system integration. The high efficiency of SOE permits electrical input reduction of the electrolyser unit and to recover heat produced in the Haber-Bosch reactor. The electricity consumption is decreased down to 8.30 kWh/kg NH_3 and zero emission of CO_2 is obtained. In the field of chemical production, the new system permits the production of zero emission ammonia and increases the flexibility of the plant compared to traditional electrolysers. Regarding this point, the stationary results reported here are encouraging for the further improvement of plant integration with other renewable energy systems, such as wind and solar systems connected to the SOE, in order to take into consideration power production variation and a dynamic modelling of the layout. Considering also the use of ammonia as a fuel and the energy storage application, a high efficiency and highly flexible concept is developed. Renewable electrical energy can be stored with an efficiency up to 62% into a liquid vector that can be transported and directly used both for power and transport applications.

The results assess the potential of a novel energy concept based on SOE as conversion technology and ammonia as fuel. NH_3 can be produced by distributed renewable energy sources directly on site. The chemical obtained is easily stored locally or transported and introduced in a more complex distribution system. In both cases it is possible to consider the final utilization in the transport sector, as a fuel, or in the power production sector for electrification with no emission of CO_2.

Appendix A

An advanced HB flowsheet has been drawn using AspenPlus Suite, according to the flowsheet of Fig. A1 below, and is always the same for each case.

The description of the parameters used in AspenPlus is as follows. The "MCompr" block type was used with the rigorous ASME method for efficiency, heat and power consumption calculation of the multistage compressor unit COMP01. Intercooling temperature after each stage and the final discharge pressure were specified for this block. EVA01 is modelled with a "HeatX" block type and the cold stream outlet temperature is fixed in order to exchange as much heat as possible. The specifications for the remaining blocks are summarized in Table A1.

The rigorous "RGibbs" reactor block is used to model the HBR with the Aspen built-in PENG-ROB method for physical and chemical equilibrium calculations. The vapour-liquid equilibrium flash drum model "Flash2" is the block used for SEP01, SEP02 and EXPANDER. The splitting ratio, i.e. the amount of purge gas, of the block SPLIT01 is used as convergence variable for the PFD. In order to increase the ammonia recovery from HBR product stream, the tail gas from EXPANDER and a part of the liquid ammonia produced are used to push the cooling of the feeding stream in EVA01. The cold stream coming out from this block, i.e. P-GAS, is gaseous NH_3 with some traces of inerts which can be still considered as useful product of the plant. The HB loop thus described produces ammonia both in liquid and gaseous forms.

The complete flowsheet of the reference case, NG-REF-HB is shown in Fig. A2.

Natural gas and air, at ambient temperature, are fed to an adiabatic combustor (BURNER), and a partial gasification process occurs with H_2 and CO formed together with CO_2. The N_2 necessary for NH_3 synthesis is fed in with the AIR stream. In the block REFORMER, a pre-heated steam stream is added to the burnt gas. The Steam-to-Carbon ratio (S/C) is fixed at 2 so that the Steam Methane Reforming (SMR) reaction can take place. Afterwards, three reactors are used (WGSR1, WGSR2, WGSR3) to complete the Water Gas Shift reaction (WGS). The reactions involved in these blocks are the following:

Table A1
Block specifications for the HB loop.

Specification	HBR	SEP01	SEP02	EXPANDER
Temperature (°C)	550	0	20	–
Pressure (bar)	250	250	250	1
Heat duty (kW)	–	–	–	0
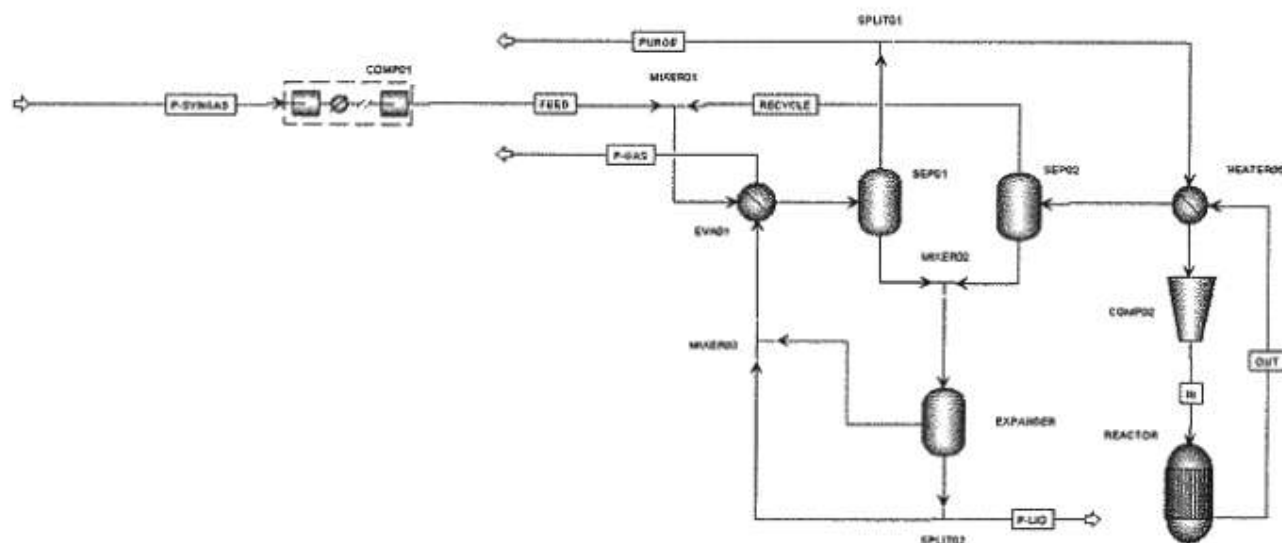
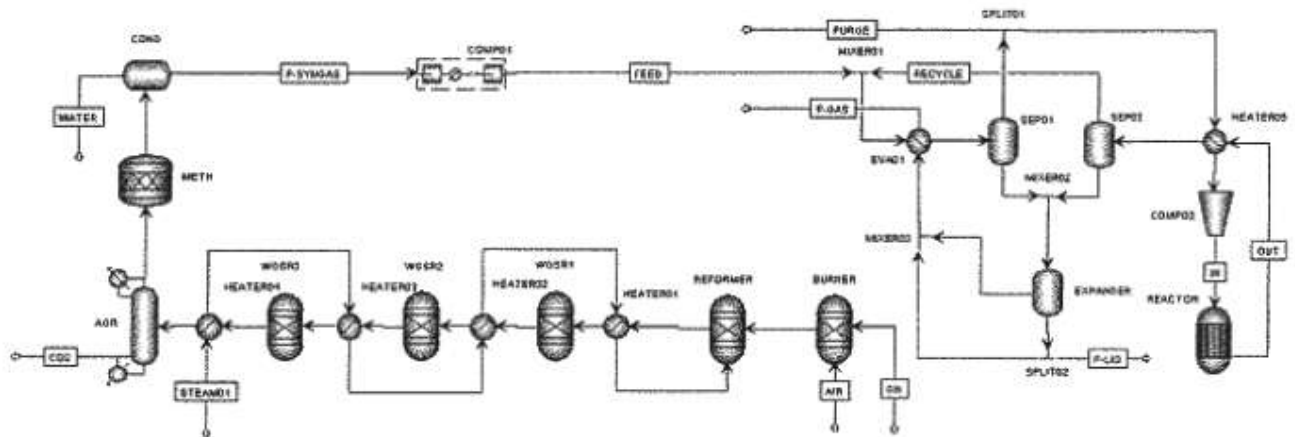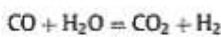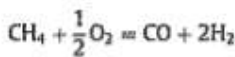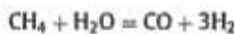

Fig. A1. Flowsheet of the HB loop developed in AspenPlus.

Fig. A2. Flowsheet diagram of the reference case NG-REF-HB.

$$CH_4 + H_2O = CO + 3H_2 \tag{A.1}$$

$$CH_4 + \frac{1}{2}O_2 = CO + 2H_2 \tag{A.2}$$

$$CO + H_2O = CO_2 + H_2 \tag{A.3}$$

$$CH_4 + 2O_2 = CO_2 + 2H_2O \tag{A.4}$$

The reactor block used to model all these units is "RGibbs" and the built-in NRTL Aspen property method was used for calculations. A "Sep" block with standard specifications concerning temperature (≈50–80 °C) and separation efficiency (>90%) is used for the AGR block [22]. An adiabatic "RStoic" reactor block is used by

Table A2
Block specifications for clean-up section.

Specification	AGR	METH	COND
Temperature (°C)	50	–	15
Pressure (bar)	1	1	1
Heat duty (kW)	–	0	–

METH to convert residual CO_2 and COND is a "Flash2" block type, operated at 15 °C to allow and complete gas/liquid separation. Table A2 summarizes the specifications of those last three blocks.

The second case is named EL-PSA-HB and its schematic flow diagram is shown in Fig. A3.

The HB loop is the same as above, while the upstream architecture for low temperature electrolysis and PSA is simpler: water is compressed in a hydraulic pump (PUMP01) and heated in a counter current heat exchanger (HEATER01) to the electrolyser (ELECTR) operating conditions, namely 80 °C and 30 bar. The built-in "Pump" block has been used to model PUMP01, HEATER01 is a "HeatX" block type and ELECTR is an "RGibbs" reactor block. The electrochemical calculations for ELECTR block are based on commercial alkaline electrolysers data from literature [26]. The PSA standard process was modelled in Aspen Plus by means of a compressor (COMP03) and a separator (PSA) in series at 30 bar, room temperature and overall N_2 purity of 99.9% [23]. The property method used in this section was the NRTL built-in Aspen model.

Finally, the last case is the SOE-PSA-HB process illustrated in the flowsheet of Fig. A4.

In this case only, the ammonia reactor was forced to operate at 650 °C and 550 bar. In order to have comparable results with the
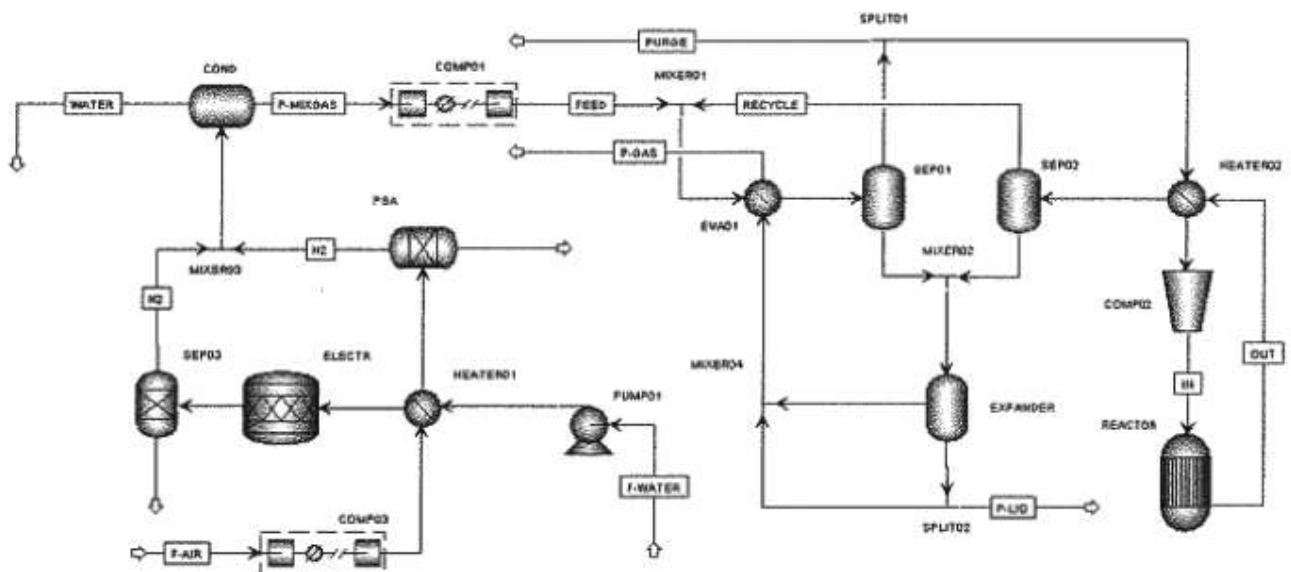

Fig. A3. Flowsheet diagram of the low temperature electrolysis case EL-PSA-HB.
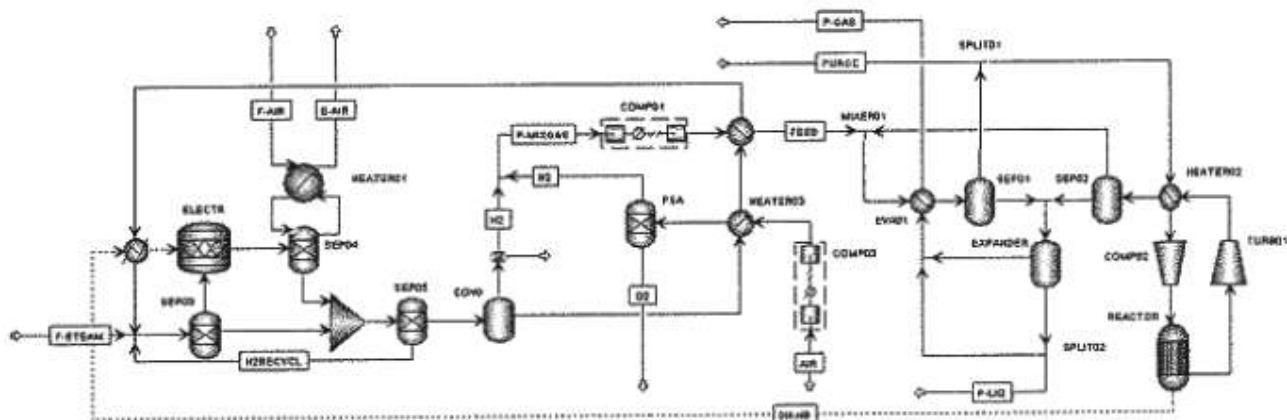
Fig. A4. Flowsheet diagram of the high temperature electrolysis case SOE-PSA-HB.

previous cases, the different pressure level is controlled only in the HB REACTOR block by using a pair of compressor/turbines before and after the block (COMP02, TURB01). Selected temperature and pressure are the highest that can be accepted for the HB process and, at the same time, this temperature is the lowest possible to consider in a SOE at the present stage of development. The original flowsheet representing the SOE unit [28] was here modified for the HB coupling purpose with the addition of a condenser (COND) to separate produced hydrogen (H2) from residual water, and a pre-heater at anode side (HEATER01), for preheating of the sweeping air (F-AIR) by heat recovery from oxygen enriched air (E-AIR) coming from anode outlet. The water separated from the COND block is used for cooling the feeding air of PSA block (AIR), and the feeding stream (FEED) before the HB loop. Afterwards, separated water is recycled to SOE as steam. Finally, the tear stream DH-HB represents the chemical heat available from the REACTOR block, due to ammonia reaction according to Eq. (1), that is used in SOE. The external subroutine for electrochemical calculations is based on the model described in Section 2.1, in order to consider the thermal contribution of HB coupling to the SOE energy balance. The only inputs to the subroutine are the operating temperature, already set at 650 °C, and the heat supplied to the SOE (DH-HB) per unit of hydrogen produced, to calculate k used in Eq. (10).

References

[1] Zamfirescu C, Dincer I. Ammonia as a green fuel and hydrogen source for vehicular applications. Fuel Process Technol 2009;90:729–37. http://dx.doi.org/10.1016/j.fuproc.2009.02.004.

[2] Frigo S, Gentili R. Analysis of the behaviour of a 4-stroke SI engine fuelled with ammonia and hydrogen. Int J Hydrogen Energy 2013;38:1607–15. http://dx.doi.org/10.1016/j.ijhydene.2012.10.114.

[3] Ryu K, Zacharakis-Jutz GE, Kong S-C. Effects of gaseous ammonia direct injection on performance characteristics of a spark-ignition engine. Appl Energy 2014;116:206–15. http://dx.doi.org/10.1016/j.apenergy.2013.11.067.

[4] Zamfirescu C, Dincer I. Using ammonia as a sustainable fuel. J Power Sources 2008;185:459–65. http://dx.doi.org/10.1016/j.jpowsour.2008.02.097.

[5] Comotti M, Frigo S. Hydrogen generation system for ammonia–hydrogen fuelled internal combustion engines. Int J Hydrogen Energy 2015;40:10673–86. http://dx.doi.org/10.1016/j.ijhydene.2015.06.080.

[6] Ferrero D, Lanzini A, Santarelli M, Leone P. A comparative assessment on hydrogen production from low- and high-temperature electrolysis. Int J Hydrogen Energy 2013;38:3523–36. http://dx.doi.org/10.1016/j.ijhydene.2013.01.065.

[7] Andersson J, Lundgren J. Techno-economic analysis of ammonia production via integrated biomass gasification. Appl Energy 2014;130:484–90. http://dx.doi.org/10.1016/j.apenergy.2014.02.029.

[8] Morgan E, Manwell J, McGowan J. Wind-powered ammonia fuel production for remote islands: a case study. Renew Energy 2014;72:51–61. http://dx.doi.org/10.1016/j.renene.2014.06.034.

[9] Patil A, Laumans L, Vrijenhoef H. Solar to ammonia – via proton's NFuel units. Proc Eng 2014;83:322–7. http://dx.doi.org/10.1016/j.proeng.2014.09.023.

[10] Giddey S, Badwal SPS, Kulkarni A. Review of electrochemical ammonia production technologies and materials. Int J Hydrogen Energy 2013;38:14576–94. http://dx.doi.org/10.1016/j.ijhydene.2013.09.054.

[11] Mingyi L, Bo Y, Jingming X, Jing C. Thermodynamic analysis of the efficiency of high-temperature steam electrolysis system for hydrogen production. J Power Sources 2008;177:493–9. http://dx.doi.org/10.1016/j.jpowsour.2007.11.019.

[12] Schulte Beerbühl S, Fröhling M, Schultmann F. Combined scheduling and capacity planning of electricity-based ammonia production to integrate renewable energies. Eur J Oper Res 2015;241:851–62. http://dx.doi.org/10.1016/j.ejor.2014.08.039.

[13] Frattini D, Cinti G, Bidini G, Desideri U, Cioffi R, Jannelli E. A system approach in energy evaluation of different renewable energies sources integration in ammonia production plants. Renew Energ 2016;99:472–82.

[14] Laguna-Bercero MA. Recent advances in high temperature electrolysis using solid oxide fuel cells: a review. J Power Sources 2012;203:4–16. http://dx.doi.org/10.1016/j.jpowsour.2011.12.019.

[15] O'Brien JE, McKellar MG, Harvego EA, Stoots CM. High-temperature electrolysis for large-scale hydrogen and syngas production from nuclear energy – summary of system simulation and economic analyses. Int J Hydrogen Energy 2010;35:4808–19. http://dx.doi.org/10.1016/j.ijhydene.2009.09.009.

[16] Sanz-Bermejo J, Muñoz-Antón J, Gonzalez-Aguilar J, Romero M. Optimal integration of a solid-oxide electrolyser cell into a direct steam generation solar tower plant for zero-emission hydrogen production. Appl Energy 2014;131:238–47. http://dx.doi.org/10.1016/j.apenergy.2014.06.028.

[17] Cinti G, Baldinelli A, Di Michele A, Desideri U. Integration of Solid Oxide Electrolyzer and Fischer-Tropsch: a sustainable pathway for synthetic fuel. Appl Energy 2016;162:308–20. http://dx.doi.org/10.1016/j.apenergy.2015.10.053.

[18] Wendel CH, Braun RJ. Design and techno-economic analysis of high efficiency reversible solid oxide cell systems for distributed energy storage. Appl Energy 2016;172:118–31. http://dx.doi.org/10.1016/j.apenergy.2016.03.054.

[19] Tallaksen J, Bauer F, Hulteberg C, Reese M, Ahlgren S. Nitrogen fertilizers manufactured using wind power: greenhouse gas and energy balance of community-scale ammonia production. J Clean Prod 2015;107:626–35. http://dx.doi.org/10.1016/j.jclepro.2015.05.130.

[20] Appl M. Ammonia, principles and industrial practice. 1st ed. Weinheim: Wiley-Vch; 1999. http://dx.doi.org/10.1002/9783527613885.

[21] Boudart M. Kinetics and mechanism of ammonia synthesis. Catal Rev 1981;23:1–15. http://dx.doi.org/10.1080/03602458108068066.

[22] Mondal P, Dang GS, Garg MO. Syngas production through gasification and cleanup for downstream applications – recent developments. Fuel Process Technol 2011;92:1395–410. http://dx.doi.org/10.1016/j.fuproc.2011.03.021.

[23] Ivanova S, Lewis R. Producing nitrogen via pressure swing adsorption. Chem Eng Prog 2012;108:38–42.

[24] Liso V, Nielsen MP, Kær SK. Influence of anodic gas recirculation on solid oxide fuel cells in a micro combined heat and power system. Sustain Energy Technol Assessments 2014;8:99–108. http://dx.doi.org/10.1016/j.seta.2014.08.002.

[25] Penchini D, Cinti G, Discepoli G, Desideri U. Theoretical study and performance evaluation of hydrogen production by 200 W solid oxide electrolyzer stack. Int J Hydrogen Energy 2014;39:9457–66. http://dx.doi.org/10.1016/j.ijhydene.2014.04.052.

[26] <www.fch.europa.eu/sites/default/files/study%20electrolyser_0-Logos_0_0.pdf> (last access 30/06/2016).

[27] <www.linde-engineering.com/internet.global.lindeengineering.global/en/images/HA_N_1_1_e_09_150dpi19_6131.pdf> (last access 30/06/2016).

[28] Cinti G, Discepoli G, Bidini G, Lanzini A, Santarelli M. Co-electrolysis of water and CO2 in a solid oxide electrolyzer (SOE) stack. Int J Energy Res 2016;40:207–15. http://dx.doi.org/10.1002/er.3450.